CALIFORNIA
ENERGY COMMISSION

Energy Research and Development Division

FINAL PROJECT REPORT

Low-Cost Thermal Energy Storage for Dispatchable Concentrated Solar Power

Gavin Newsom, Governor
March 2021 | CEC-500-2021-020

PREPARED BY:

Primary Authors:
Richard E. Wirz, Amey Barde, Karthik Nithyanandam, Kaiyuan Jin, Yide Wang

University of California Los Angeles
420 Westwood Plaza, Engineering IV
Los Angeles, CA 90095
(310) 825-5489
http://www.wirz.seas.ucla.edu/

Contract Number: EPC-14-003

PREPARED FOR:
California Energy Commission

Michael Kane
Project Manager

Jonah Steinbuck, Ph.D.
Office Manager
ENERGY GENERATION RESEARCH OFFICE

Laurie ten Hope
Deputy Director
ENERGY RESEARCH AND DEVELOPMENT DIVISION

Drew Bohan
Executive Director

ACKNOWLEDGEMENTS

This research effort was supported by California Energy Commission Contract Number EPC-14-003 and Southern California Company Grant No 5660042538. The researchers express their sincerest gratitude to these agencies and the associated personnel for their support of this project.

The authors acknowledge the contributions to the project from Professor Adrienne Lavine, Professor Miguel Garcia-Garibay, Parker Wells, Mitchell Shinn, Gabriella Bran, Sid Naik, Louis Tse, Ethan Ely, Christos Voutsaras, Dr. Adam Collins, Dr. Zhitong Chen, Dr. Taylor Matlock, Anirudh Thuppul, Nolan Uchizono, Cesar Huerta, Henry Huh, Angelica Ottaviano, Phil Chiu, Ben Dankongkakul, Will Sauer, Christos Voutsaras, and Peter Wright.

PREFACE

The California Energy Commission's (CEC) Energy Research and Development Division supports energy research and development programs to spur innovation in energy efficiency, renewable energy and advanced clean generation, energy-related environmental protection, energy transmission and distribution and transportation.

In 2012, the Electric Program Investment Charge (EPIC) was established by the California Public Utilities Commission to fund public investments in research to create and advance new energy solutions, foster regional innovation and bring ideas from the lab to the marketplace. The CEC and the state's three largest investor-owned utilities—Pacific Gas and Electric Company, San Diego Gas & Electric Company and Southern California Edison Company—were selected to administer the EPIC funds and advance novel technologies, tools, and strategies that provide benefits to their electric ratepayers.

The CEC is committed to ensuring public participation in its research and development programs that promote greater reliability, lower costs, and increase safety for the California electric ratepayer and include:

- Providing societal benefits.
- Reducing greenhouse gas emission in the electricity sector at the lowest possible cost.
- Supporting California's loading order to meet energy needs first with energy efficiency and demand response, next with renewable energy (distributed generation and utility scale), and finally with clean, conventional electricity supply.
- Supporting low-emission vehicles and transportation.
- Providing economic development.
- Using ratepayer funds efficiently.

Low-Cost Thermal Energy Storage for Dispatchable Concentrated Solar Power is the final report for Contract Number EPC-14-003 conducted by the University of California, Los Angeles. The information from this project contributes to the Energy Research and Development Division's EPIC Program.

For more information about the Energy Research and Development Division, please visit the CEC's research website (www.energy.ca.gov/research/) or contact the CEC at ERDD@energy.ca.gov.

ABSTRACT

Elemental sulfur is a low-cost energy storage media suitable for many medium to high temperature applications, including trough and tower concentrated solar power and combined heat and power systems. In this project, researchers demonstrated the viability of an elemental sulfur thermal energy storage (SulfurTES) system as a viable technology for utility-scale thermal storage applications. The research team identified scientific and engineering tasks, including material compatibility analysis, thermodynamic study, sulfur heat transfer behavior study, laboratory- and pilot-scale demonstration, and system-cost analysis. The scientific tasks revealed that sulfur could be safely controlled in low-cost containment systems at high temperatures over hundreds to thousands of thermal cycles. Sulfur exhibited excellent heat transfer behavior, resulting in superior thermal charge/discharge characteristics of the SulfurTES systems. These outcomes were further used for the design of laboratory and pilot-scale demonstration of the SulfurTES systems. These demonstrations showed that a SulfurTES battery can be successfully integrated with diverse energy sources, including solar energy to store high-grade thermal energy for multiple thermal cycles at temperatures up to 600^{o}C with volumetric energy density of about 400 kilowatt-hours per cubic meter. Further, the experiments were conducted to study the effect of operating conditions on the thermal charge/discharge characteristics of SulfurTES system based on thermal charge/discharge rate, exergetic efficiency, and energy efficiency. The results of the laboratory- and pilot-scale demonstration were used to develop a system-cost model. This model is used as design tools to define the parametric space for which the utility-scale SulfurTES systems can achieve performance and cost targets.

Keywords: sulfur, sulfurTES battery, thermal energy storage (TES), charge/discharge characteristics

Please use the following citation for this report:

Wirz, Richard E., Barde Amey, Nithyanandam Karthik, Jin Kaiyuan, and Yide Wang. 2021, *Low-Cost Thermal Energy Storage for Dispatchable Concentrated Solar Power*. California Energy Commission. Publication Number: CEC-500-2021-020

TABLE OF CONTENTS

LIST OF FIGURES

Page

LIST OF TABLES

Page

EXECUTIVE SUMMARY

Background

California has been leading the efforts to develop and deploy renewable energy technologies to generate carbon-neutral electricity. Recently, the state has set an ambitious goal of 100 percent renewable and carbon-free electricity generation by 2045. At present, 36 percent of California's electricity is from renewable energy sources such as solar and wind. Continued, aggressive integration of renewable energy sources into the energy system is necessary to achieve the state's 2045 goal. Although renewable energy sources are vital for reducing and eliminating the adverse impacts of today's energy technologies, these sources are intermittent and need complementary technologies to ensure grid reliability.

The thermal energy storage system is a promising complement to intermittent renewables and pairs with concentrated solar power. The thermal energy storage system stores excess solar energy harvested during a period of peak solar insolation as heat, which is later used to generate electricity during a period of low insolation or at night. An integrated concentrated solar power/thermal energy storage system ensures continuous supply of solar energy for generation of carbon-free electricity. The state-of-the art thermal energy storage systems use molten salt as a thermal storage medium. However, these systems suffer from inherent drawbacks, including a restricted operating temperature range of 536° Fahrenheit –1,049° Fahrenheit (280°Celsius – 565°Celsius) due to physical and chemical properties of solar salt and high thermal storage costs (for example, not meeting the United States Department of Energy target of $15 per kilowatt-hour [kWh]). Efforts to overcome these technological barriers are mainly focused on the development of advanced molten salts that can operate at high temperatures. However, these efforts have not yielded a reliable thermal storage solution for high-temperature applications, and, thus, a need exists for high-temperature, low-cost thermal energy storage technology.

Project Purpose

For this project, the Energy Innovation Laboratory at the University of California, Los Angeles, developed a novel thermal storage system using elemental sulfur as a storage medium (SulfurTES). Sulfur is abundantly available in nature at a very low cost (~$0.04–0.12/kilogram. It is chemically stable over a wide temperature range from 248°F – 1,832°F (120°– 1,000°C) and provides moderate heat capacity to store high-grade thermal energy. SulfurTES systems have potential to replace state-of-the art thermal energy storage technology to provide a low-cost, high-temperature alternative for utility-scale applications. The ultimate goal of the project was to identify and resolve key technological barriers and help advance it to the level that will generate confidence in the industry to further develop the SulfurTES technology for commercial applications. Integrating the utility-scale SulfurTES system will enable the concentrated solar power companies to generate low-cost, carbon-free electricity for 24 hours. This will accelerate the number of concentrated solar power systems into the existing energy infrastructure, while ensuring the reliable and low-cost operation of the electricity grid. Successful use of the SulfurTES systems will help California to achieve its 2045 clean electricity goal, providing economic benefits and improved quality of life to California residents.

The research team adopted a holistic approach for the development of SulfurTES technology to address scientific, engineering, and system-level challenges. The outcome of this research is useful for a range of stakeholders, including academia, industry, investors, and policymakers. This report will serve as a guide for further development of the SulfurTES technology for commercial and industrial applications.

To achieve the final project goal, project researchers identified and met several key objectives:

1. Material compatibility analysis to identify the materials that can be used in high-temperature sulfur environment.
2. Thermal analysis of elemental sulfur to characterize the thermodynamic behavior of sulfur and identify the thermochemical benefits for thermal energy storage application.
3. Heat transfer analysis of sulfur to characterize the thermal charge/discharge behavior of SulfurTES systems.
4. Laboratory-scale demonstration of the 10-kWh SulfurTES system over multiple thermal cycles.
5. On-sun demonstration of the pilot-scale SulfurTES system integrated with concentrated solar power dish to store 30 kWh of thermal energy.
6. System-cost analysis for the development of low-cost, high-performance utility-scale SulfurTES system.

Project Approach

The project team was comprised of researchers from academia, a concentrated solar power company, and a utility company (Southern California Gas) to achieve the scientific and engineering objectives of the project.

The research objectives of this project were classified into two categories: scientific and engineering. Successfully completing the scientific objectives provided insight into the physical mechanism that govern the functioning of the SulfurTES systems and included a material compatibility study, thermal analysis, and heat transfer analysis. The engineering objectives were designed toward developing and analyzing the SulfurTES systems and included laboratory-scale demonstration, pilot-scale demonstration, and system-level analysis. This holistic approach allowed the research team to mature the SulfurTES technology and make it ready for the product development stage.

The project team identified two important technical challenges for this technology. First is the identification of the low-cost containment materials that are compatible with high-temperature sulfur environment. Researchers conducted exhaustive literature review and screened three potential sulfur containment materials: stainless steel 304, stainless steel 316, and Inconel. These materials were subjected to qualitative and quantitative analyses to characterize their resistance to the sulfur corrosion. These analyses revealed that stainless steel 316 and Inconel are able to resist sulfur corrosion at high temperatures for long periods of operation. The team selected stainless steel 316 to contain the sulfur because of its significantly lower cost as compared to Inconel. The second challenge was designing low-cost containers that can safely contain sulfur over a long period of thermal (heat) charge/discharge cycles. The researchers found that moderate sulfur pressure existed at high operating temperatures which allowed

them to develop thin-walled, low-cost containers to safely store the sulfur over hundreds-thousands of thermal cycles.

The thermal performance of the SulfurTES systems is governed by the sulfur heat transfer characteristics. The team used experimental systems and computational and analytical tools to understand the component and system level heat transfer behavior of the sulfur for relevant design parameters and operating conditions. These studies showed that the sulfur exhibits excellent heat transfer performance resulting in the rapid charge/discharge rates of the SulfurTES system. The team conducted the system-level analysis to identify the parametric space for the design and operating conditions for which the SulfurTES system can meet the performance and the cost targets.

The project team received guidance from a technical advisory committee comprised of Guangdong Zhu (National Renewable Energy Laboratory), Adam Green (Solar Reserve), Milton Venetos, Jim McDermott, David Cygan, and Jeffrey Reed. The members of the committee have expertise in the fields that are important for the successful development of the thermal energy storage system. Their feedback was essential for the development of safe and effective SulfurTES systems. For example, a committee member suggested conducting a stress analysis of the stainless steel 316 tubes containing the sulfur to ensure that they can be safely operated for 30 years, which is the typical life of the thermal energy storage systems. This feedback motivated the team to conduct the life cycle analysis of the SulfurTES system and to ensure 30 years of operational lifetime.

Project Results

The research team successfully met all of the scientific and engineering objectives of the project. The SulfurTES technology was demonstrated in two stages. In the first stage, the laboratory-scale prototype of the SulfurTES system was developed to store more than 10 kWh of thermal energy over multiple thermal cycles. The research team analyzed the thermal performance of this system for many flow and temperature operating conditions to characterize the charge/discharge behavior. In the second stage, the SulfurTES system was scaled from 10 kWh to 30 kWh storage capacity and integrated with the concentrated solar power system for the on-sun demonstration of the technology. Moreover, the team developed a system-cost model to develop utility-scale SulfurTES systems that can achieve performance and cost targets. The research team successfully demonstrated the SulfurTES technology to store high-temperature solar energy, and also developed heat transfer and system-level analysis tools that will be used to design low-cost, high-performance utility-scale SulfurTES systems. These research efforts have matured the SulfurTES technology to become ready for the product development stage.

Technology/Knowledge Transfer/Market Adoption (Advancing the Research to Market)

The research team leveraged the experience and knowledge it gained through the project to create a cleantech startup, Element 16 Technologies, Inc., to commercialize the SulfurTES technology. The team identified combined heat and power and combined cooling heat and power systems for the commercial and industrial applications as beachhead markets, and

Element 16 has received grants from California Energy Commission to develop the SulfurTES systems for these applications.

The 2020 energy storage mandate may require investments of as much as $3 billion on power-storage systems in California to facilitate wider use of renewable energy. For the concentrated solar power thermal energy storage market, the 2013 global total available market can be estimated at $2.6 billion and the U.S. total available market is estimated at $1.6 billion. The majority of the United States market is located in Nevada, New Mexico and California. For the concentrated solar power industry, the market is expected to grow at a compounded annual growth rate of 44.9 percent.

The members of the technical advisory committee provided their expertise to identify strategic partners and potential investors that will enable the research team to propel the technology in the real-world applications.

Benefits to California

The overarching goal of this project was to develop a low-cost, high-temperature thermal energy storage technology that will enable and complement renewable energy sources, particularly solar energy, providing lower cost carbon-free electricity to California ratepayers. This proposed technology will lead to considerable reduction in greenhouse gas emissions of 776 tons per megawatt-hour electric (ton/MW_e) of CO_2, 0.023 ton/MW_e of sulfur dioxide (SO_2), and 1.2 ton/MW_e of nitrogen oxide (NO_x). Shifting power plant workload to night also reduces the plant cooling water requirements, saving the state 2.95 tons of water per time-shifted megawatt. These solutions will provide economic benefits to the California taxpayer, as well as ensure a better quality of life for residents.

CHAPTER 1: Introduction

For renewable energy to contribute significantly to the overall energy supply, low-cost storage options must be demonstrated and implemented. An effective implementation of a low-cost thermal energy storage (TES) system can achieve this goal by providing dispatchability to renewable energy resources, including concentrated solar power (CSP) and can even be considered for storing surplus electric energy from photovoltaics (PV) and wind turbines during times of over-generation. Moreover, studies have shown that integration of a thermal energy storage system with a combined heat and power (CHP) system yields improved thermal performance and reduces fossil fuel consumption, resulting in favorable economics [1, 2].

The performance and value of a TES system were analyzed based on three important parameters, namely, the cost of energy storage, operating temperature range, and thermal performance. Several thermal energy storage systems, operating on various physical principles have been developed; most common being latent, sensible, and thermochemical energy storage systems. A review of latent [3-9] and thermochemical [10-11] energy storage systems showed that these technologies are in the Research & Development phase and must overcome many practical challenges to be mature enough for industrial applications.

State of the art TES system is a two-tank molten salt system operating in the temperature range of 536˚F – 1049˚F (280˚C –565˚C) [12-14]. Many commercial CSP plants [15-19] have adopted this technology to provide energy dispatchability. Despite their successful implementation, state-of-the-art molten salt TES systems suffer from inherent drawbacks, including the higher cost of energy storage [3,20] and degradation at temperatures above about 565˚C. Thus, the need remains for low-cost, high-temperature thermal energy storage options that can overcome these challenges and achieve effective integration of renewable energy resources.

In this project, the team developed a low-cost, high-temperature thermal energy storage system using elemental sulfur as thermal storage medium (SulfurTES). Wirz et al., [21] proposed a novel concept to use elemental fluids, including sulfur, as the primary fluid for thermal energy storage. Sulfur is a molten medium over much of the temperature ranges important to CSP and, therefore, has many of the heat transfer and overall system performance advantages of molten salt, while avoiding the inherent limitations of the molten salts systems. Sulfur is abundantly available in nature at a very low cost ($0.04—0.12/kilogram [kg]). Sulfur does not degrade with temperature due to its elemental nature and can be used as a thermal storage fluid at temperatures up to 1200˚C. [22], making it an ideal thermal storage medium for medium-high temperature applications.

The research team identified key scientific and engineering objectives to identify and resolve technical barriers ahead of the technology and mature it to the product development stage. The study conducted a material compatibility analysis to identify low-cost materials that can withstand high-temperature sulfur environment for hundreds-thousands of thermal cycles. This analysis revealed the ability of SS316 and Inconel to resist sulfur corrosion at high temperature; the team selected SS316 as sulfur containment material due to its low cost.

Further, researchers conducted a thermodynamic analysis to study the pressure temperature characteristics of sulfur over the temperature range of interest for CSP applications (up to 600˚C). The thermodynamic analysis showed that sulfur exerts moderate pressures even at maximum operating temperatures, which allowed use of thin walled tubes to safely contain sulfur during thermal charge/discharge cycles, thus reducing the cost of sulfur containment. The heat transfer analysis is another important research effort conducted by the research team to study the charge/discharge behavior of SulfurTES systems. The team used experimental systems and computational/analytical tools to study sulfur heat transfer behavior under a controlled environment for relevant design parameters and operating conditions. The heat transfer analysis revealed excellent charge/discharge rates for sulfur resulting in superior thermal performance of SulfurTES systems. These scientific research tasks provided physical insight into the functioning of sulfur as a thermal storage medium and their outcomes were used as design inputs for the engineering tasks, including laboratory and pilot-scale demonstrations and system-level analysis of SulfurTES systems.

For the laboratory-scale demonstration, the research team developed a SulfurTES battery based on the shell-and-tube heat exchanger concept. The SulfurTES battery was operated over multiple thermal cycles for temperatures up to 600˚C to store greater than 10 kWh of thermal energy. The team also studied the effect of charge/discharge flow rates and temperatures on the SulfurTES performance, based on thermal charge/discharge rates, exergetic efficiency, and energy efficiency. The results of laboratory-scale demonstration were further used to refine the SulfurTES battery design for the development of the pilot-scale demonstration of the SulfurTES.

For the pilot-scale demonstration, the study developed a 30 kWh SulfurTES battery and integrated it with the CSP system developed by project partner, Thermal Storage Systems (TSS), a CSP company. TSS developed a CSP-dish system and a solar receiver to capture solar energy and convert it into high temperature thermal energy, which was used for the thermal charging of the SulfurTES battery. During the on-sun demonstration, the team stored greater than 30 kWh of thermal energy over multiple thermal cycles for temperatures up to 600˚C. Further, researchers conducted multiple thermal cycles to study the thermal performance of the SulfurTES battery for many flow and temperature conditions during the charging and discharging processes. The results of the laboratory- and pilot-scale demonstrations were used for development and validation of the system-cost model.

The system-level analysis is important to design utility-scale SulfurTES systems that can achieve performance and cost targets. The research team is developing an analytical model to predict the system-level performance of the SulfurTES systems for many geometric parameters and operating conditions. The performance of the SulfurTES systems will be analyzed based on the thermal charge/discharge rates, exergetic efficiency (ability of energy to produce work), and energy efficiency. Moreover, the analytical tool will be used to determine the thermal storage cost of the SulfurTES system to ensure that the United States Department of Energy cost target is achieved. This analytical tool will be an important design tool for system engineers for design and operation of the utility-scale SulfurTES systems that can achieve performance and cost targets.

These research efforts have established the viability of SulfurTES system as a prominent thermal energy storage technology for medium-high temperature applications. Successful

development and integration of utility-scale SulfurTES systems with CSP will increase the contribution of renewable sources to the total electricity generation. This will allow California to achieve its energy goals and bring economic benefits and better quality of living to California ratepayers.

CHAPTER 2:
Material Compatibility Analysis

Introduction

The goal of the material compatibility task is to test the compatibility of primary containment materials with elemental sulfur. Three different alloys with potential application for containment of sulfur as an energy storage fluid, namely SS304, SS316, and Inconel 600, were studied. All alloys were thermally cycled to maximum temperatures of 500°C and 600°C and kept at those temperatures for minimum and maximum time durations of 100 and 900 hours, respectively. Wall thickness measurements, scanning electron microscope (SEM), and energy dispersive X-ray spectrometer (EDS) results for all three different alloys are presented and discussed. The results of the analyses were successful since the vessels maintained their integrity after 900 hours at 500°C and 100 hours at 600°C. Tests were performed for sulfur at the impurity levels found in low-cost/commercially available sulfur. Corrosion rates for high-temperature thermal energy applications (500—600°C) satisfied lifetime requirements for both SS316 and Inconel 600 alloys.

Containment Material Selection

The material selection was based on extensive literature review of recorded interactions between sulfur and several metals and alloys at elevated temperatures and for extended periods of time [3,22-40]. Several different materials are used to resist corrosion in high sulfur environments. The best candidates for containment material are materials with an acceptable low rate of corrosion for the given application. Increasing the chromium content in steel increases its resistance to sulfidation [26,31,32]. Alloys containing chromium are able to protect the surface from corrosion caused by sulfur due to the formation of protective chromium sulfide film. High chromium stainless steels are also used to resist corrosion in sulfidizing environments [33,34].

Aluminum, platinum, and molybdenum are known to be completely resistant to sulfidation at temperatures up to and greater than 350°C [23,34-36]. According to several references, aluminum is considered to be resistant to corrosion by sulfur [25,36-38]. Aluminizing low-carbon steel and low-alloy steel has been successfully used in the petroleum refining industry to prevent sulfidation [30]. Aluminum has been used in the development of new alloys resistant to sulfidation at high temperatures [23]. Titanium alloys show great corrosion resistance against sulfur [29]. In environments containing elemental sulfur, Ti-alloys show no localized corrosion at temperatures up to 260°C [33].

Platinum and molybdenum are known to be resistant to sulfidation at temperatures up 1100°C [23.34-36]. In the presence of sulfur, molybdenum forms a layer of molybdenum disulfide ($MoS_{2)}$, which grows extremely slowly. At 350°C, a layer of MoS_2 about 0.2 microns thick forms on molybdenum in the presence of sulfur. Molybdenum is considered to be a highly sulfur corrosion resistant alloy [39]. Hastelloy-B, a nickel and molybdenum-based alloy, shows no measurable corrosion after 100 hours exposure to sulfur at 350°C (only slight tarnishing was present) [39].

Stainless steel is also used in sulfidizing environments. It is used extensively in the petroleum refinery industry, where sulfidation is an issue [34]. Type 347 stainless steel (SS347) is used in the reactor vessels for hydrocracking and hydrotreating systems to protect against high-temperature sulfidation [30]. Stainless steels such as 9Cr-1Mo are used to resist sulfidation in the catalyst regeneration unit, where temperatures can be up to 760°C [25]. Alloy type SS310 is known to be highly resistant to oxidation and sulfidation at temperatures higher than 590°C to avoid oxidation and sulfidation [39].

Based on the literature analysis, two corrosion resistant alloys, SS316 and Inconel 600, were identified as the most promising candidates for sulfur storage at high temperature and high pressure, because of their high content of chromium. Notably, stainless steel is a more attractive material compared to Inconel 625, because of its lower cost. SS304 will also be tested, and the results will be used as the controlled test. The chemical compositions of the three containment materials are presented in Table 1.

Table 1: Chemical Composition of Tested Alloys Before Sulfur Exposure (wt.%)

Alloy	Cr	Ni	C	Mn	Cu	Mo	Si	S	P	N	Fe
SS304	14.66	5.65	0.08	0.7	0.08	1.1	0.32	0.2	0.02	5.65	71.54
SS316	17.58	14.5	0.08	0.2	0.5	2.11	0.75	0.35	0.04	0.02	63.87
Inconel 625	17.38	71.88	—	—	—	—	—	—	—	—	10.74

Source: UCLA, Wirz Research Group

Test Tube Preparation

The test tubes were manufactured at the University of California, Los Angeles (UCLA) facilities. The tubes are 115 millimeters (mm) long with a 12.7 mm outside diameter. The wall thickness of all the tubes is 0.889 ± 0.127 mm, as specified by the manufacturer (Figure 1a). The tubing geometric dimensions are listed in Table 2. The tubing wall values will be compared with the values measured after the wall has been exposed to sulfur at high temperatures for different time periods. To ensure that no leaks occur during the thermal cycling, the end of the crimped section was welded as shown in Figure 1b. The tubes were washed with soap and water, and then rinsed with acetone. The tubes were left overnight inside an oven at a temperature of 250 ºC to remove moisture and other impurities from the surface.

Table 2: Material Specifications

Alloy	316 (mm)	304 (mm)	600 Inconel (mm)
Wall Thickness	0.889	0.889	0.889
Wall Thickness Tolerance	±0.127	±0.127	
OD	12.7	12.7	12.7
ID	10.99	10.99	10.99
OD Tolerance	±0.254	±0.254	±0.254

Source: UCLA, Wirz Research Group

Sulfur with an assay percent range of 99.5—100.5 percent was used. Sulfur was heated above melting temperature (114.6°C) to eliminate any air pockets and moisture in an alumina

crucible. One end of each tube was crimped and welded as shown in Figure 1a and b. The molten sulfur was poured into each of the tubes 76.2 mm above the welded edge. Once the sulfur was completely solidified, the tubes were vacuumed, crimped, and welded on the other end (Figure 1b). This procedure ensured that moisture and impurities were extracted from the inside of the tubes. The temperature of three of the test tubes was monitored with two thermocouples attached to the wall as shown in Figure 1c. The test tubes were placed in an oven (Figure 1d) that ramped up to a maximum temperature of 500°C or 600°C for each thermal cycle.

Figure 1: Experimental Setup

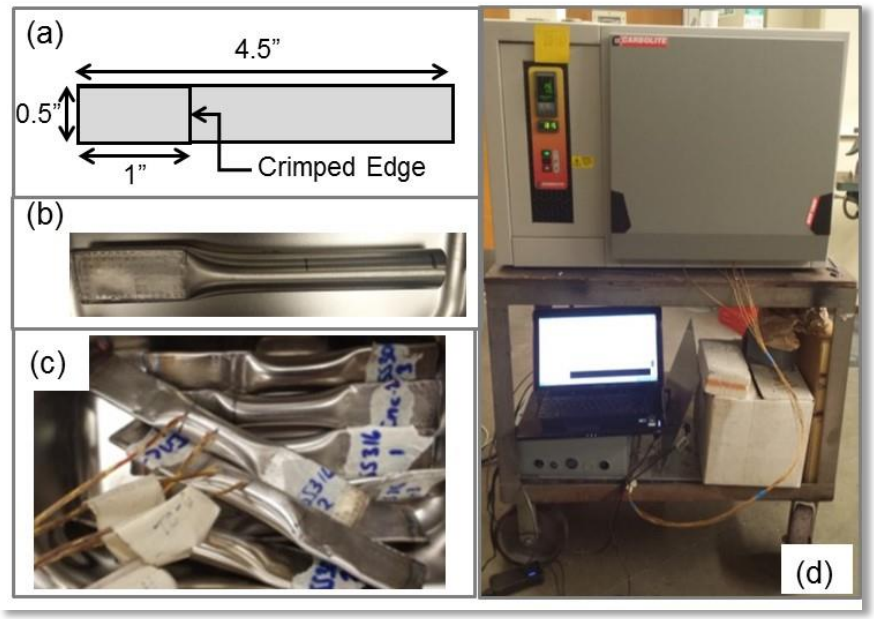

(a)Test tube dimensions, (b) test tubes without sulfur, (c) test tubes filled with sulfur, and (d) final experimental setup (oven, DAQ, power supply, and thermocouples).

Source: UCLA, Wirz Research Group

Experimental Procedure

Three tubes of each material were thermal cycled to the maximum temperature of 500°C for a total of 100 hours, 600 hours, and 900 hours. In addition, three tubes of each material were also thermal cycled to the maximum temperature of 600°C for a total of 100 hours. The cross-sectioned area of each tube as shown in Figure 2 was analyzed. Each sample was cleaned using CS_2 to dissolve the sulfur residuals on the wall surface. The wall thickness was measured before and after sulfur exposure to determine if sulfur reacted with the tube’s wall. A Scanning Electron Microscope (SEM) Nova230 with an attached Energy Dispersive X-ray spectrometer (EDS) was used to determine if sulfur at high temperatures of 500°C and 600°C deteriorated the tube inside wall. The wall thickness of the three tubes was measured using the SEM to obtain the change in the wall thickness.

Figure 2: Surface of Interest for Material Compatibility Analysis

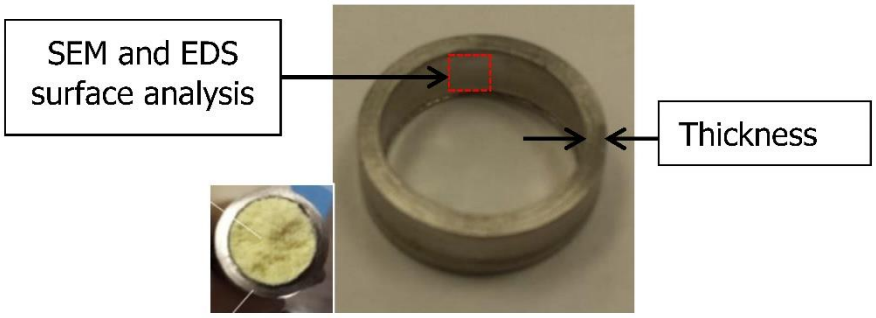

Source: UCLA, Wirz Research Group

Experimental Test at 500°C

Figure 3 shows the SS304, SS316, and Inconel tubes filled with pure sulfur before and after the thermal cycling. Expected rust can be observed on the three metal tubes. The tubes successfully maintained their integrity and no significant pitting corrosion occurred after 900 hours at 500°C**.** The wall thicknesses of the SS304, SS316, and Inconel 600 tubes before sulfur exposure (0 hours), and after 100 hours, 600 hours, and 900 hours of sulfur exposure are shown in Figure 4. The thickness of SS304 decreases from 1235 µm (0 hours) to 937 µm (600 hours) as the sulfur exposure time increases. Due to the rapid wall thickness decrease of the SS304 tube from 0 hours to 600 hours of sulfur exposure, SS304 tubes were not subjected to 900 hours of sulfur exposure as a safety precaution. The rapid decrease of thickness on the SS304 tubes was expected because SS304 is known to be corrosive in environments with sulfur.

On the other hand, SS316 and Inconel 600 showed an increase in tube wall thickness. Figure 4 demonstrates that the wall thickness of the SS316 tube increased from 738.5 µm (0 hours) to 946.3 µm (100 hours) and the Inconel 600 tube increased from 1015.5 µm (0 hours) to 1042.7 µm (100 hours). However, no significant increase in thickness was measured for either SS316 or Inconel 600 after 100 hours of exposure to elemental sulfur. The thickness of the SS316 and Inconel tubes exposed for 600 hours was thicker by 2.8 µm and 42.7 µm, respectively, than the tubes exposed for 100 hours. This is evidence of the formation of sulfide layers (sulfidation) as a result of the high activity of sulfur in the gaseous environment. Assuming linear corrosion behavior and TES operation period of eight hours per day, the wall thicknesses measurements before and after sulfur exposure for SS304 showed a corrosion rate of 846.8 µm/year. For SS316 and Inconel 600, the wall thickness due to sulfide layer formation increased at a rate of 26.28 µm/year and 496.4 µm/year, respectively. Inconel demonstrated a faster growth of protective sulfide layer than the SS316.

Figure 3: SS304, SS316, and Inconel Tubes Filled with Pure Sulfur

(a) Before Thermal Cycling, and (b) After Thermal Cycling (Total of 600 Hours at 500°C)

Source: UCLA, Wirz Research Group

Figure 4: Wall Thickness Measurements of SS304, SS316, and Inconel 600 Before and After Testing

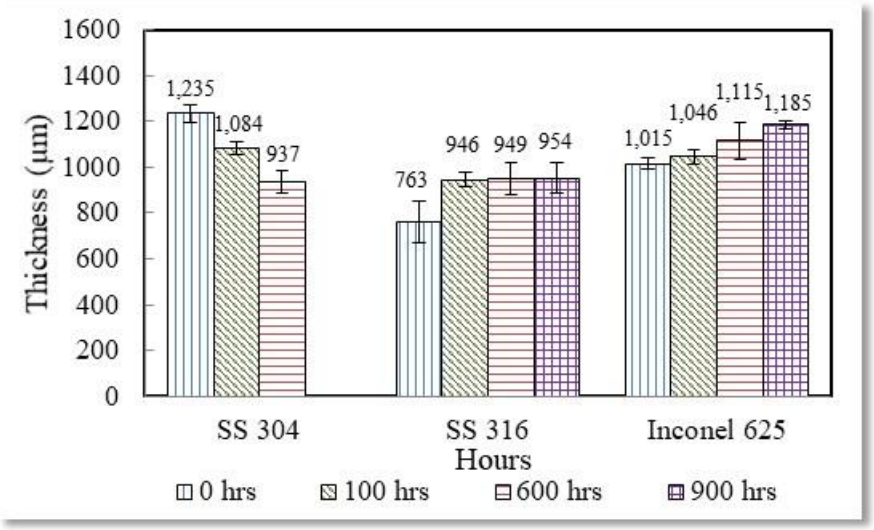

Source: UCLA, Wirz Research Group

Conclusion

Corrosion experiments were performed for three types of alloys (SS304, SS316, and Inconel 600) in contact with pure dry sulfur at 500°C and 600°C for the minimum and maximum time periods of 100 and 900 hours, respectively. The results of the analysis are successful since the vessels maintained their integrity after 900 hours at 500°C and 100 hours at 600°C. Wall thickness measurements, SEM, EDS, and X-ray powder diffraction analyses were performed on the three different alloys after sulfur exposure. SS304 had reduced thickness of the wall in contact with sulfur. SS316 and Inconel 600 had increased wall thickness due to the formation of a protective sulfide layer that slows down corrosion rate. No significant change was noticed on the sulfide layer growth after 100 hours at 500°C for either SS316 or Inconel 600. The results obtained are consistent with observations in literature that dealt with material compatibility of high temperature alloys with sulfur. EDS results from the containment of each tube also show that SS316 and Inconel 600 are more resistant to corrosion than SS304. The contamination of sulfur is due to a reaction that occurred with the tube surface, which concurs

with observations in the literature indicating that SS304 should react more with sulfur than SS316 and Inconel 600.

The results signify that the best candidate for containing sulfur for thermal energy storage application based on cost and material compatibility performance analysis is SS316. This alloy demonstrated high corrosion resistance under the desired conditions. This alloy is also low cost and easy to manufacture. On the other hand, although Inconel 600 also showed high corrosion resistance; it is expensive compared with SS316. This is consistent with previous studies that rate Inconel as an excellent corrosion resistant alloy, SS316 as a good corrosion resistance alloy, and SS304 as moderate corrosion resistant alloy. Overall, for the typical range of impurities in commercially available elemental sulfur, corrosion rates for high temperature solar thermal energy applications remained acceptable for SS316 and Inconel 600 alloys.

CHAPTER 3:
Thermal Analysis of Storage Fluid

Introduction

The overarching goal of the thermal analysis was to investigate the thermodynamic characteristics of sulfur in the temperature range of 25 ^{o}C – 600^{o}C. The main objectives of this analysis were to: (1) investigate the pressure-temperature characteristics of sulfur, and (2) quantify the thermochemical benefits. The experiments were conducted at various operating conditions of sulfur mass content and containment material. At the maximum operating temperature (600^{o}C), sulfur has a moderate pressure (around 200 pounds per square inch gauge [psig]), which allows the use of thinner tubes (schedule 10 pipe) to store sulfur and, consequently, a lower containment cost. The containment was found to have a negligible influence on the pressure-temperature characteristics of elemental sulfur. Further, allotropic and species transformation in sulfur were analyzed to quantify the contribution of the thermochemical reactions in the thermal energy storage capacity of the sulfur. The thermochemical energy storage has a notable contribution to the total thermal energy storage, and this contribution can be enhanced by operating the system at favorable thermodynamic conditions.

Pressure-Temperature Characteristics

Experimental Set-Up

The objective of this analysis was to determine the pressure-temperature characteristics of elemental sulfur isochorically stored in the container. A schematic and the picture of the experimental set-up are shown in Figure 5. The experimental set-up comprised of a SS316/Inconel tube with a 1.5-inch nominal pipe size diameter (schedule 40) and a length of 9 inches. The tube was equipped with a K-type thermocouple immersed in the sulfur to measure its temperature. In addition, multiple K-type thermocouples were placed axially along the tube to measure the surface temperatures and thermal losses. A high temperature pressure gauge and pressure transducer were used to measure pressure within the system. Pressure and temperature measurements were recorded using the data acquisition (DAQ) system coupled with LabVIEW. A high temperature tape heater was wrapped around the containment vessel and heat input was controlled using a proportional–integral–derivative controller. The system was wrapped with aluminum silicate thermal insulation to minimize losses and to ensure safety.

Figure 5: Experimental Set-Up for the Sulfur Pressure; Temperature Characterization Up to 600°C

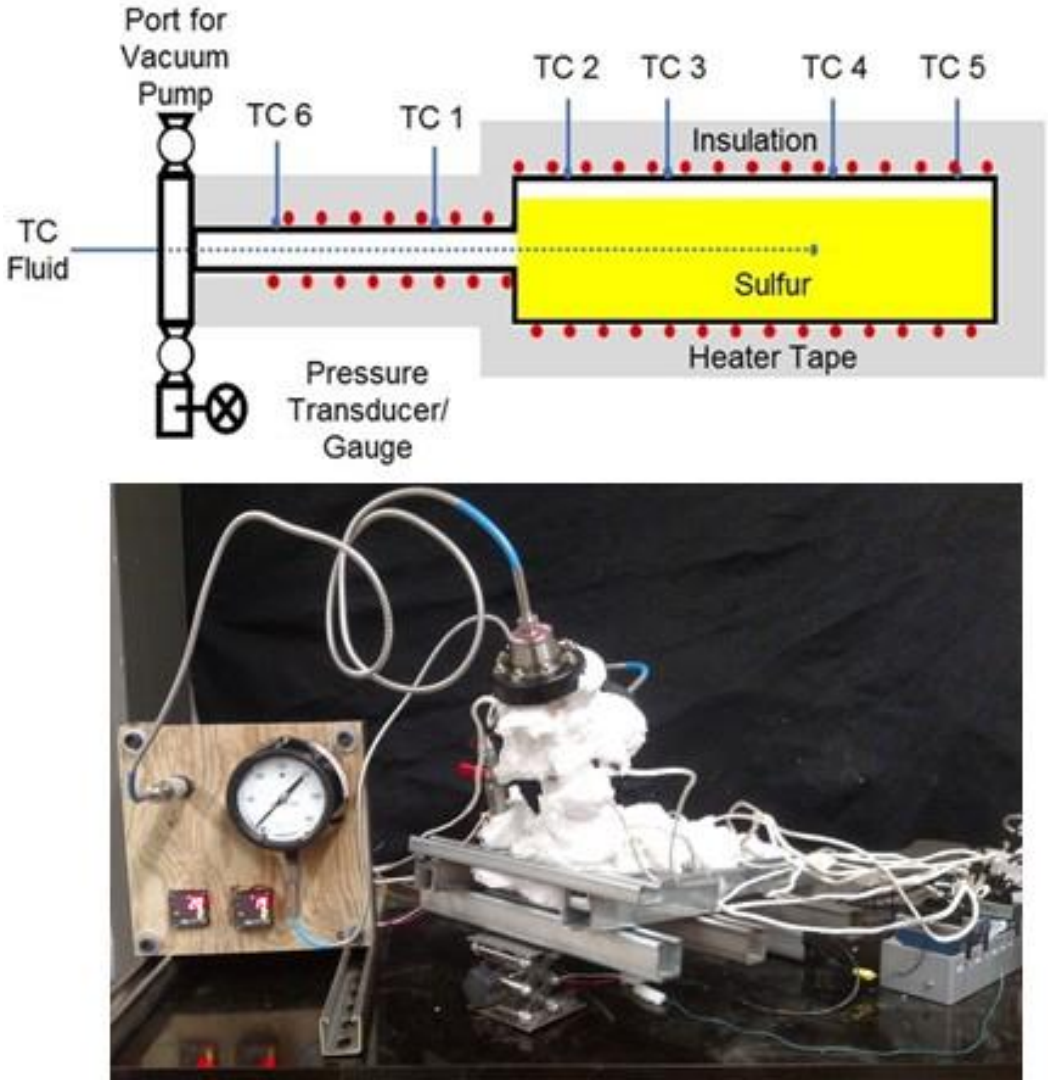

Source: UCLA, Wirz Research Group

Experimental Procedure

Sulfur can react with contaminants including air, water vapor, and organic compounds to form undesirable gases, including H_2S, SO_2, and CS_2, that can influence the system pressure. To remove these contaminants, the system and accessories were cleaned with acetone and the containment vessel was then heated to 600°C to further remove organic contaminants, as needed. The system was then loaded with the measured amount of sulfur to achieve desired sulfur loading fraction. The system was purged with argon to ensure an inert environment in the containment vessel. The system was then closed, and essential instruments, including thermocouples and a pressure gauge/transducer were installed. Further, the system was wrapped with heater tape and insulated with high-temperature ceramic insulation. Researchers observed that, despite thorough cleaning of the tubes before filling, some gases were generated as the system was heated to 600°C, due to contaminants in the sulfur powder as shown in Figure 6. The qualitative analysis of these gases is presented in Figure 7. Thus, after the first few cycles, the system was opened, and a vacuum pump was used to remove these

gases. The system was then filled with argon and sealed. At this point in time, experiments could be performed to obtain reliable pressure-temperature characteristics.

Figure 6: First Cycle of Pressure-Temperature Characteristics for Different Loading Fraction Showing Generation of Gases

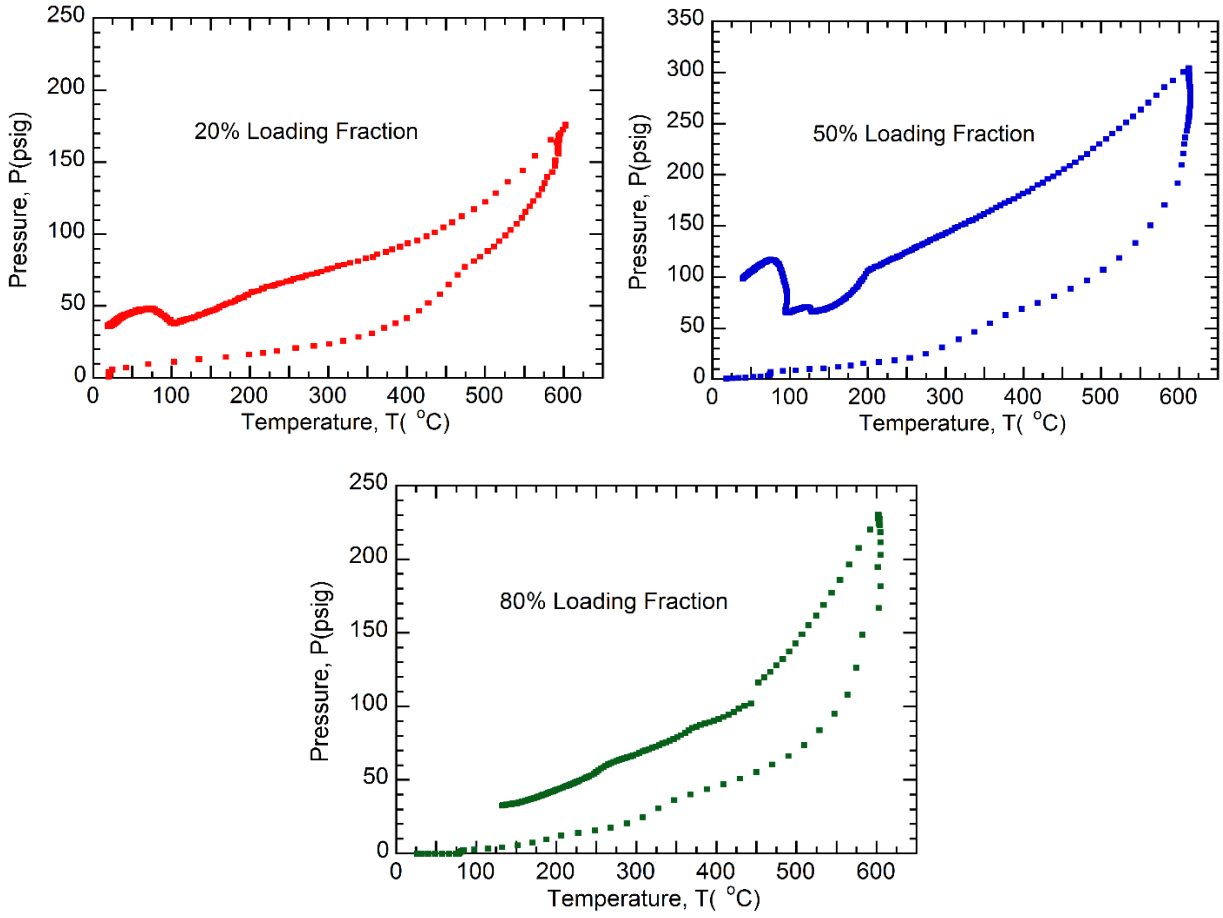

Source: UCLA, Wirz Research Group

Figure 7: Qualitative Abundance of Gases Generated in the System During Thermal Charging-Discharging Cycle

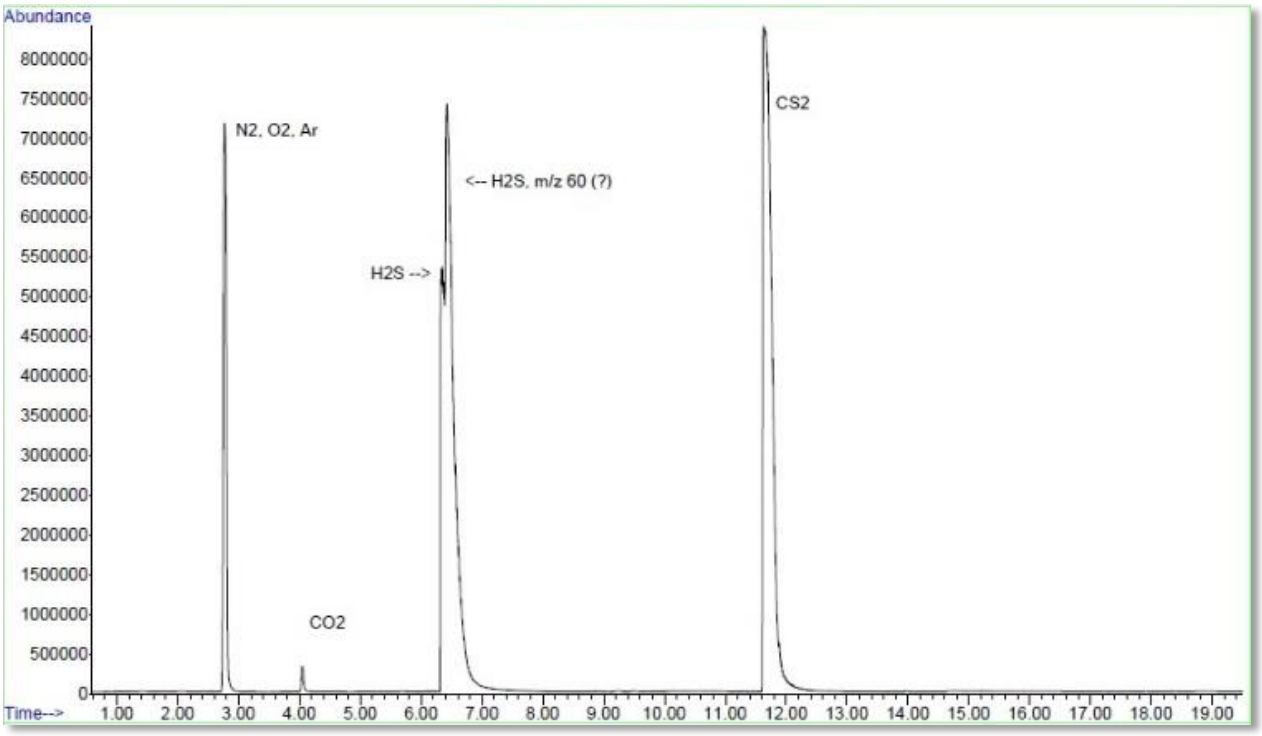

Source: UCLA, Wirz Research Group

Results and Analysis

The experiments were conducted to study the effect of different sulfur loading fraction and containment vessel. The selected sulfur loading fractions (LF) were 20 percent, 50 percent and 80 percent, while the experiments were conducted in two independent containment vessels fabricated from SS316 and Inconel 800. The loading fraction of sulfur was defined as:

$$Sulfur\ LF = \frac{Volume\ of\ sulfur\ at\ melting}{Volume\ of\ vessel}$$

For each sulfur LF, multiple thermal cycles were conducted to establish the reliability of the experimental measurements. Figure 8 shows pressure-temperature characteristics for various sulfur LF for three consecutive thermal charging-discharging cycles in the SS316 containment vessel. It can be observed that the pressure-temperature characteristics are repeatable for each sulfur loading fraction. The team observed that as the loading fraction increases, the maximum pressure of sulfur increases. However, the rise in maximum pressure was moderate and not linearly related to the sulfur LF.

Figure 8: Pressure-Temperature Characteristics for 20%, 50%, and 80% Sulfur Loading Fractions

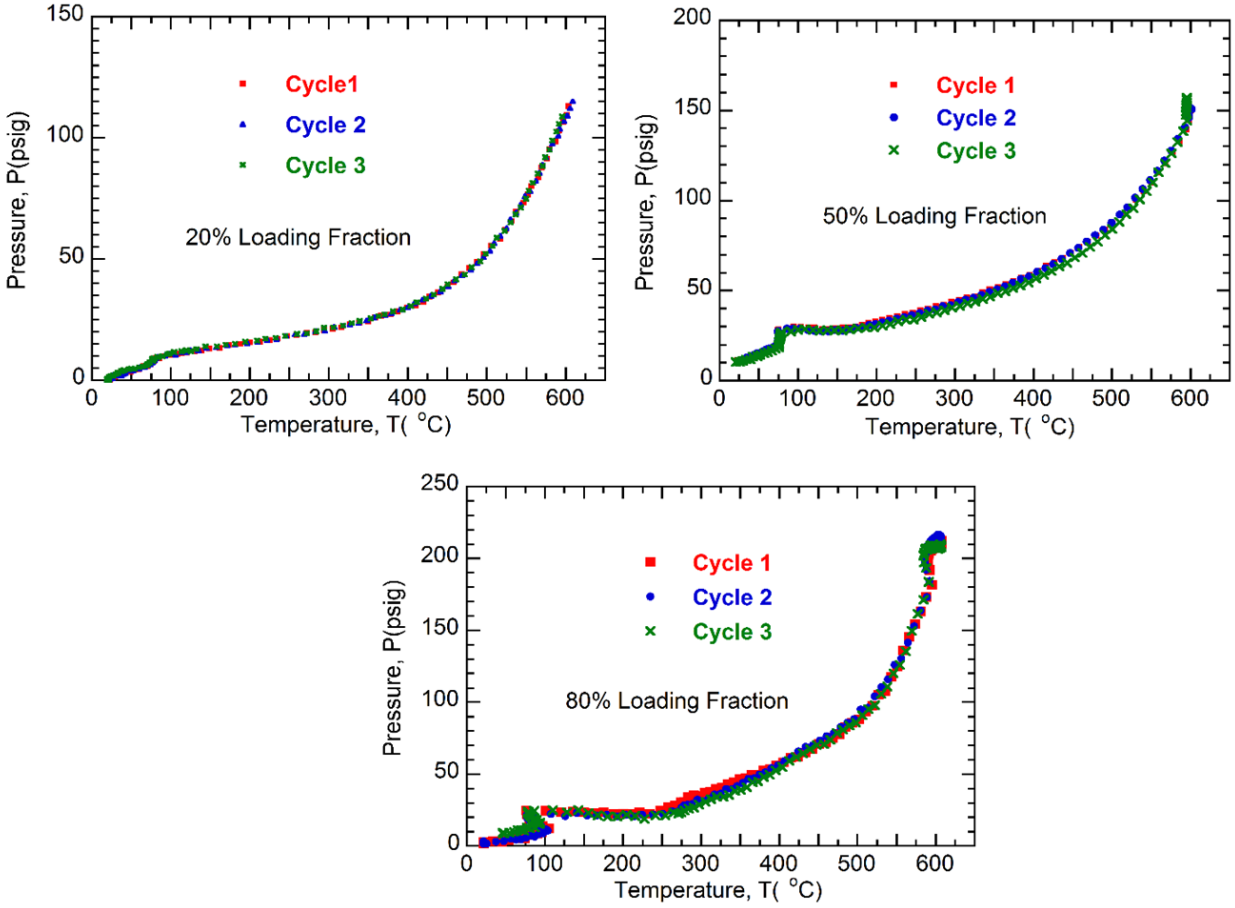

Source: UCLA, Wirz Research Group

Similar experiments were conducted in Inconel 800 container to examine the effect of containment vessel on the pressure-temperature characteristics. Figure 9 shows a comparison between sulfur pressure-temperature characteristics obtained using SS316 and Inconel 800 containment vessels. The pressure-temperature characteristics for different loading fractions were identical and containment vessel had no discernible effect on them.

Figure 9: Pressure-Temperature Characteristics

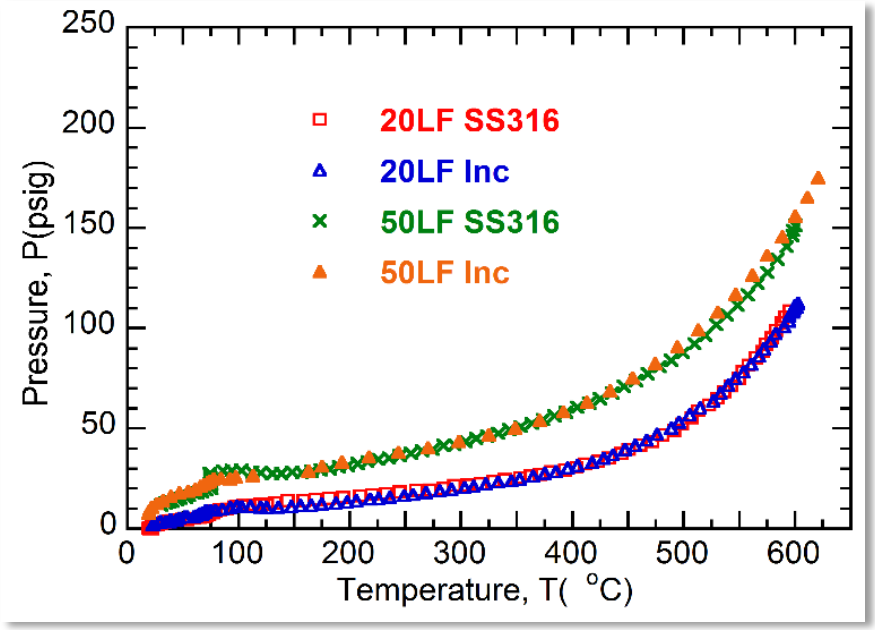

Using Containment Vessels of SS316 and Inconel 800 for 20% and 50% Sulfur Loading Fractions

Source: UCLA, Wirz Research Group

The team acknowledged that for some cycles, initial pressure existed due to residual gases that expanded with temperature and contributed to the total pressure. A simple thermodynamic model was developed to predict the system pressure as a function of temperature. The system pressure has two components, sulfur pressure and gas pressure. The saturation sulfur pressure can be obtained from literature based on previous studies. The sulfur density significantly decreased with temperature as shown in Figure 10, thus its volume increased as a function of temperature [41]. Accordingly, gas in the system was pressurized due to the rise in temperature as well as to the decrease in the relative volume of gas. The gas pressure can be estimated using fundamental ideal gas law.

$$P_{gas} = \left(\frac{PV}{T}\right)_{initial} \times \left(\frac{T}{V}\right)_{final}$$

The saturation pressure of sulfur can be expressed using empirical correlation by Rau et al. [42]

$$\log_{10} P_{Sulfur} = 60.9106 - \frac{24971}{T} + \frac{1.0817e7}{T^2} - \frac{2.2060e9}{T^3} - 14.4102 \log_{10} T \qquad (1)$$

$$P_{system} = P_{gas} + P_{sulfur} \qquad (2)$$

Figure 10: Density of Sulfur as a Function of Temperature

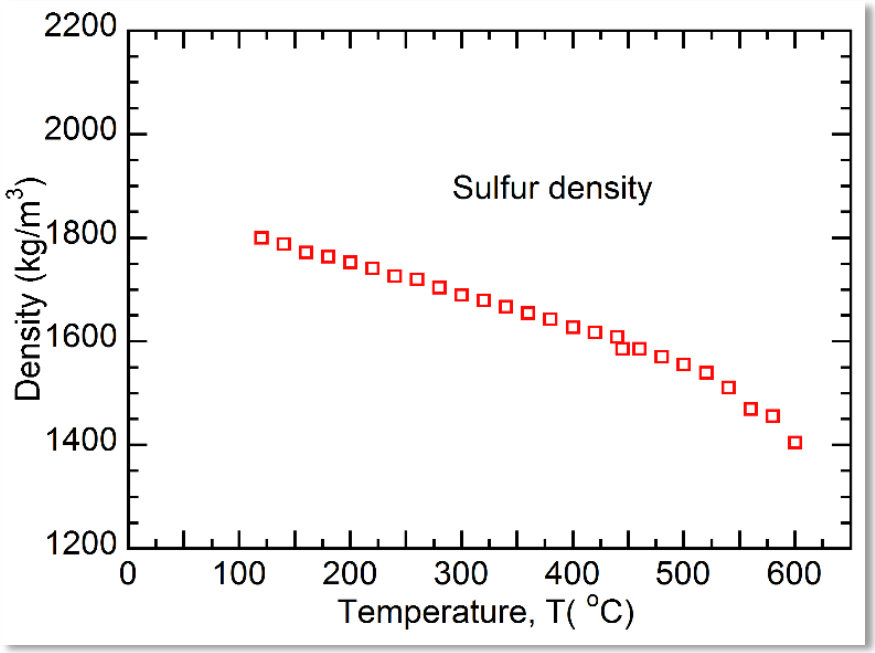

Source: UCLA, Wirz Research Group

Figure 11 shows the comparison of system pressure estimated using this simple thermodynamic model and the experimental pressure measurements for 20 percent sulfur LF. The model predictions are qualitatively in accordance with experimental measurements. However, the study showed that other physical factors contributed to the system pressure and an advanced model is required to account for their effects. One of the potential factors is the estimation of sulfur pressure. For the current analysis, saturated sulfur vapor pressure was used as the actual sulfur pressure in the system. The saturated sulfur pressure is very low for temperatures less than 300°C, and only at high temperatures can it have a discernible contribution to the total system pressure. However, the system is at moderate pressures at 300°C, which may suppress the vaporization of liquid sulfur into the vapor phase. This phenomenon may result in lower sulfur pressure than corresponding saturated sulfur pressure, which is not accounted for in the analytical model.

Figure 11: Comparison of Experimental Measurements and Model Predictions for Pressure Temperature Characteristics for 20% Loading Fraction

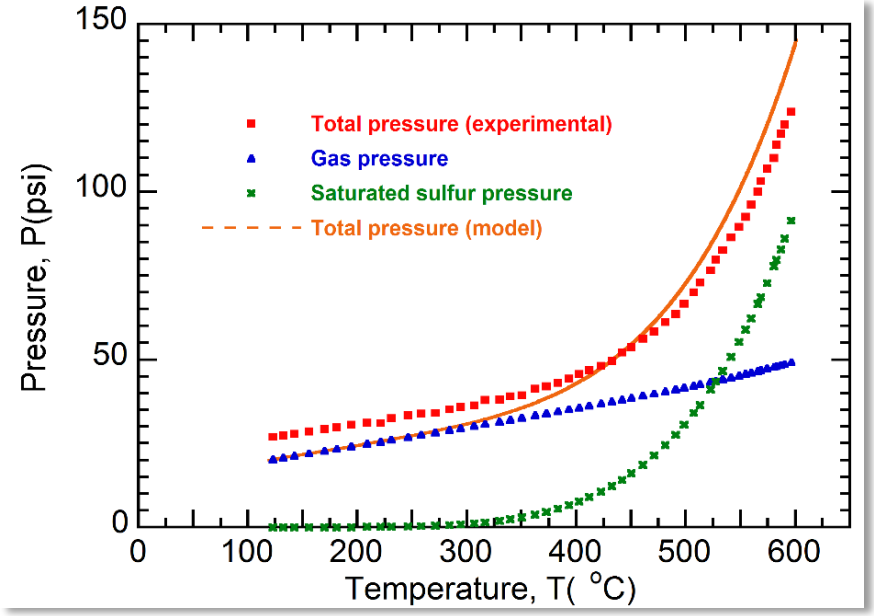

Source: UCLA, Wirz Research Group

Quantification of Thermochemical Benefits

Elemental sulfur undergoes allotropic and species changes at various temperatures. These changes occur in different physical states of sulfur and are accompanied with a high enthalpy of transformation. These transformations contribute toward the effective heat capacity of the sulfur and are advantageous for the thermal energy storage application. In this section, the allotropic and species changes in sulfur were studied and their contribution in the thermal energy storage were estimated.

Allotropic Transformations

Allotropic transformations primarily occurred in solid and liquid sulfur. At room temperature, solid sulfur was present in the orthorhombic α-sulfur and monoclinic β-sulfur forms. At 95°C, α-sulfur transformed into monoclinic β-sulfur, and the enthalpy of transformation was 12.5 kilojoules per kilogram (kJ/kg) [43].

$$\alpha - sulfur \rightarrow \beta - sulfur \qquad \Delta H = 12.5 kJ/kg \qquad (3)$$

In the liquid phase, sulfur existed in three different allotropic forms: λ-sulfur, π-sulfur, and μ-sulfur. λ-sulfur transformed into π-sulfur and μ-sulfur as the sulfur temperature was increased. At 159°C, the enthalpy of transformation of λ to π conversion was 535 kJ/kg. Similarly, at 170°C the enthalpy of transformation of λ-sulfur to μ-sulfur was 52 kJ/kg [43]. The details of these transformations are provided in Table 3.

Table 3: Allotropic Transformations in Liquid Sulfur

Transformation Reaction	Temperature (°C)	Enthalpy of Transformation (kJ/kg)	% Change in # Moles
λ-sulfur→ π-sulfur	159	535	3.82
λ, π -sulfur→ μ-sulfur	170	52	10.5

Source: UCLA, Wirz Research Group

Species Transformations

As sulfur was heated further, it also underwent species transformation from S_8 to S_2, with the presence of intermediate species. In the vapor phase, three sulfur species, S_8, S_6, and S_2 coexisted in an equilibrium state; their composition varied with temperature as shown in Figure 12. The concentration of S_8 molecules decreased while that of S_6 and S_2 increased with a higher temperature [44]. The dissociation of S_8 molecules to form S_6 and S_2 molecules is represented as follows [43]:

$$\frac{3}{4}\, S_8\,(g) \;\leftrightarrow\; S_6(g) \quad \Delta H = 101.8\ kJ/mol \qquad (4)$$

$$S_8\,(g) \leftrightarrow 4S_2\,(g) \quad \Delta H = 101.6\ kJ/mol \qquad (5)$$

Figure 12: Equilibrium Composition of Sulfur Species as a Function of Temperature

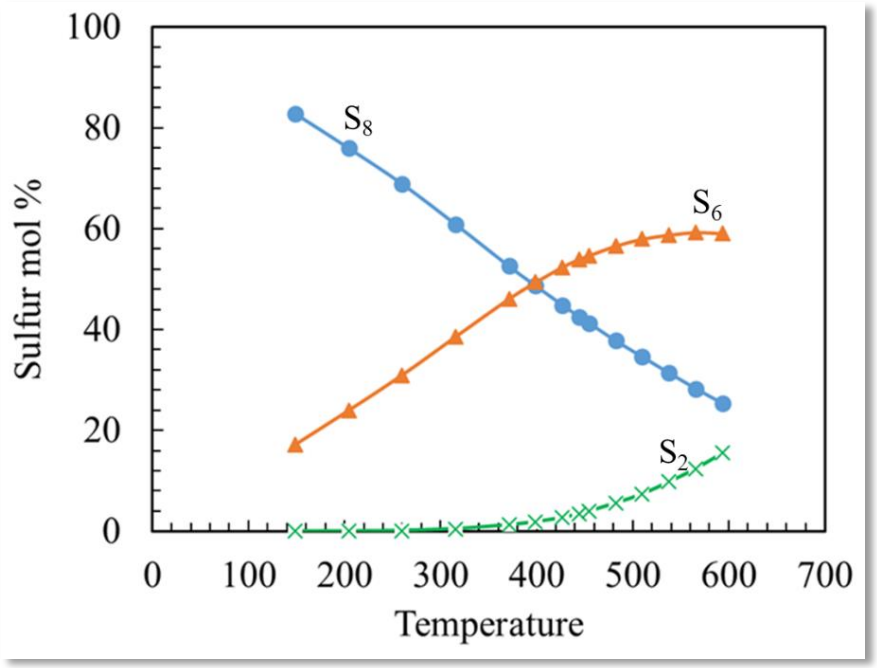

Source: UCLA, Wirz Research Group

Determining the number of molecules of different sulfur species present in the vapor phase was important to estimate the thermal energy absorbed to drive these dissociation reactions. Thus, researchers used the pressure-temperature characteristic to estimate the number of sulfur moles present in the vapor phase during thermal charging. Then, using the concentration ratios at a given temperature as shown in Figure 12, the composition of each sulfur species was determined. In the following section, the analysis to determine moles of

sulfur species was discussed for the case of 20 percent LF of the sulfur. A similar analysis can be used for different sulfur content.

As discussed earlier, the total pressure recorded during pressure-temperature characterization had two components to it: (a) gas pressure (argon and other nonsulfur species), and (b) sulfur pressure.

$$P_{total} = P_{Gas} + P_S \quad (6)$$

It is difficult to directly determine the sulfur pressure as the evaporation of liquid sulfur into the vapor phase was a dynamic process and depended on the system pressure and temperature. However, moles of argon in the system were constant. The ideal gas law can be used to determine the argon pressure (henceforth termed as gas pressure) at different temperatures during the thermal charging process. The gas pressure in the container rose due to: (a) expansion of sulfur, and (b) increase in temperature. The effect of these processes can be captured using the ideal gas law:

$$P_{Gas,final} = \left(\frac{PV}{T}\right)_{Gas,final} \times \left(\frac{T}{V}\right)_{Gas,final} \quad (7)$$

The expansion of the sulfur was the result of a decrease in density with temperature as shown in Figure 10. Thus, for a given sulfur mass, the sulfur volume was a function of temperature. Gas pressure can be represented as a function of temperature:

$$P_{Gas,final} = Cf(T) \quad (8)$$

Therefore,

$$P_s = P_{total} - Cf\ (T) \quad (9)$$

Figure 13a shows the total system pressure and individual contribution from gas and sulfur species. The study showed that the contribution of the sulfur vapor began at around 300°C, which was in accordance with the saturated pressure of sulfur. The comparison between saturated sulfur pressure and sulfur vapor pressure (Figure 13b) showed that the latter followed the saturated vapor pressure curve up to ~350°C, beyond which the sulfur vapor pressure was lower than corresponding saturation pressure.

Figure 13: Gas and Sulfur Vapor Pressure

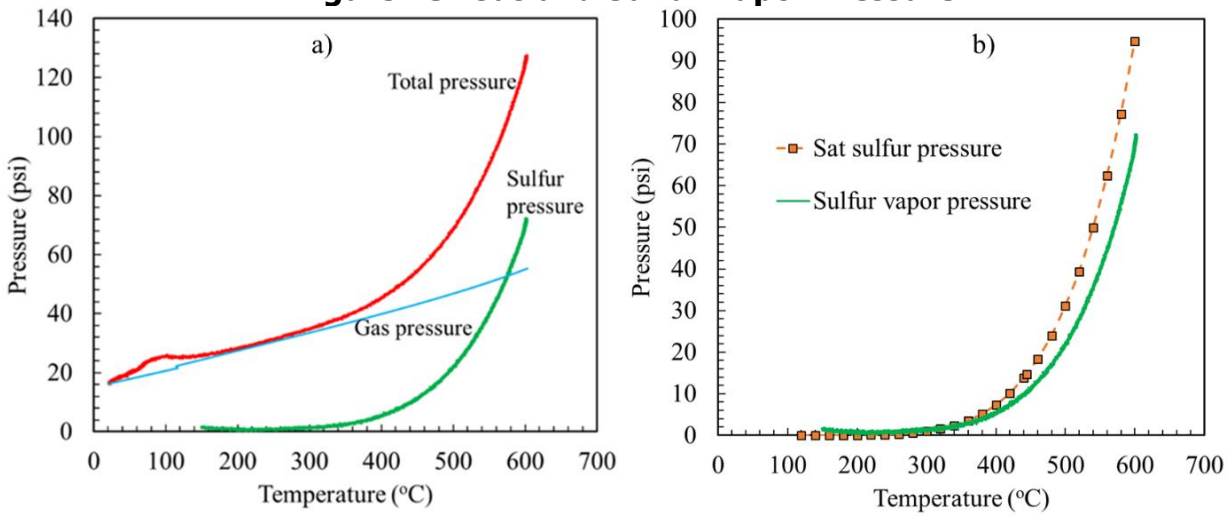

(a)Contribution of Gas Sulfur Vapor and Sulfur Vapor Pressure in the Total System Pressure, (b) Comparison Between Sulfur Vapor Pressure and Saturated Sulfur Pressure

Source: Freeport Sulphur Company

The isochoric heating increased the system pressure so that it may have suppressed the sulfur vaporization leading to lower sulfur vapor pressure than corresponding saturation pressure. For the mixture of gases, the ratio of their partial pressures can be represented as a corresponding molar ratio:

$$n_s = \frac{p_s}{p_{gas}} \times n_{gas} \qquad (10)$$

At room temperature, argon was the only gaseous species in the container. Based on the thermodynamic conditions at room temperature, gas (argon) moles can be calculated as:

$$n_{Gas} = \frac{PV}{RT} = .01 \qquad (11)$$

Thus, at the end of thermal charging, the estimated number of sulfur moles was:

$$n_s = \frac{72.47}{55.2} \times .011 \qquad (12)$$

$$n_S = 0.015$$

Using the equilibrium composition of various sulfur species as a function of temperature (Figure 12), the moles of different sulfur species (S_2, S_6, and S_8) were determined at 600°C. Further, using equations 4 and 5, total enthalpy of dissociation was calculated and shown in Table 4.

Table 4: Species Transformations in Sulfur Vapor at 600°C

Sulfur Species	Mole % at 600°C	Number of Moles	Total Enthalpy of Transformation (kJ)
S_2	15.5	0.0023	0.06
S_6	59.1	0.0089	0.67
S_8	25.4	0.0040	0.0
		Total	0.73

Source: Freeport Sulphur Company

The total enthalpy of species transformation was low since a small number of sulfur moles were present in the vapor form that participated in the dissociation process. Thus, there was a scope for further analysis to determine favorable thermodynamic and operating conditions to accelerate the vaporization process, thereby increasing the thermochemical energy storage contribution.

Thermochemical Energy Storage Capacity

The analysis of the thermochemical transformation in sulfur showed that the contribution of these transformations in the thermal energy storage varied with the physical state of the sulfur. Based on the thermochemical reactions discussed earlier, the energy stored in the sulfur in different physical states was calculated for the system with 20 percent LF (131g of sulfur) as shown in Figure 14a. Further, the energy stored in sulfur via thermochemical transformations was compared with sensible and latent (solid-liquid) modes of thermal storage in the temperature range of 25 °C —600°C (Figure 14b). The study observed that the thermochemical energy storage is ~7 percent of the sensible energy stored in sulfur. However, it was approximately the same as the thermal energy stored via phase change (latent) mechanism.

Figure 14: Energy Stored in Sulfur

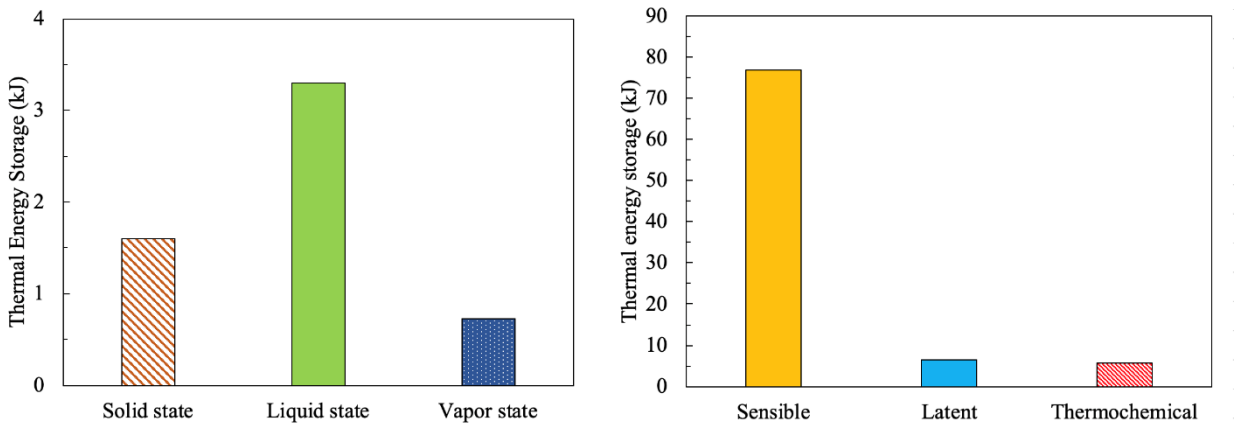

(a)Thermochemical Energy Stored in Physical States of the Sulfur, (b) Sensible, Latent, and Thermochemical Energy Stored in Sulfur

Source: Freeport Sulphur Company

Conclusion

Wirz Research Group's Energy Innovation Lab successfully conducted the thermal analysis of the elemental sulfur in the temperature range of 25 ^{o}C – 600^{o}C. This analysis has provided a valuable insight into the thermodynamic behavior of sulfur in the temperature range of interest. These important design inputs were applied for the development of a 10-kWh laboratory-scale thermal battery (Task 6). The pressure-temperature characteristics of sulfur showed that the maximum sulfur pressure increased with increased sulfur loading fraction. However, the rise in pressure was relatively moderate and did not increase linearly with the loading fraction. Moderate sulfur pressure (~200 psig) was at high operating temperatures (~600^{o}C), allowing the use of thin walled tubes (sch. 10) to contain the sulfur, which significantly reduced the thermal storage cost. Moreover, investigation of the allotropic and species transformations in sulfur revealed the contribution of these thermochemical reactions to the total thermal energy storage capacity of the sulfur. In the temperature range of 25 ^{o}C – 600^{o}C, the thermochemical energy storage was approximately 8 percent of the sensible energy storage, and equal to the latent energy storage. This contribution can be increased by adopting favorable thermodynamic and operating conditions, especially at high temperatures (greater than 300^{o}C) to accelerate the species transformations in sulfur at gaseous state. Overall, thermal analysis of the elemental sulfur availed important design tools for the development of low-cost, safe, and reliable thermal energy storage systems for high-temperature applications.

CHAPTER 4:
Heat Transfer Analysis

Introduction

The predominant goal of the heat transfer analysis task was to develop an experimentally validated computational model for predicting the heat transfer effectiveness at component and system levels. The main objectives of this task were to: (1) develop a computational heat transfer model to simulate the natural convection heat transfer from the container wall to the storage fluid (component level), and (2) develop a computational heat transfer model to quantify the heat transfer performance (system level). A computational model was developed and validated against experiments of a single tube with well-defined temperature boundary conditions and internal temperature measurements to simulate the heat transfer performance at the component and system level. Researchers achieved excellent correlation between both the experimental and computational results. Through careful analyses of these results, the team developed an unprecedented understanding of the heat transfer behavior of isochorically stored sulfur for a wide range of desirable storage temperatures. Most notably, the results clearly showed excellent charge/discharge rates — much faster than competing phase change material (PCM) and solid based TES — due to the strong assistance of buoyancy driven convection currents within the sulfur containment system. A numerical model involving a 3D computational domain of the shell and tube thermal battery to study the heat transfer performance at the system level was also developed. The experimental measurements from the full cycle testing of lab demo (Task 6) was used for validation of the model. The model was then used to provide insights to the heat transfer fluid (HTF) flow, temperature distribution and heat transfer characteristics of the thermal battery during the charge and discharge process.

Experimental Heat Transfer Analysis

This section presents the details of an experimental analysis conducted to understand the sulfur heat transfer behavior for relevant temperature operating conditions. The results of the experimental analysis were used to validate the computational model developed to predict the thermo-fluidic behavior of sulfur at high temperatures (600^{o}C).

Experimental Set-Up

Figure 15 shows the schematic of the experimental facility developed to investigate the heat transfer behavior of sulfur. The experimental facility comprised the SS316 tube with 2-inch NPS Sch. 40 OD and 1-meter length. The tube was filled with 3.2 kg of sulfur, which corresponded to 80 percent of volumetric loading fraction. A half-inch thick cap sealed either end of the tube. These caps were equipped with instrumentation ports that provided access to six K-type thermocouples to record sulfur temperature at different axial and radial locations, as shown in Figure 16. The steel tube was wrapped with eight heaters tapes; each heater was independently controlled using a proportional–integral–derivative controller. Sixteen K-type thermocouples were installed to measure the tube surface temperatures as well as to monitor the electrical power input to the heater tapes. A LabVIEW program coupled with NI cDAQ

9178 data acquisition chassis was used to record the temperature measurements and to control the heater tape functioning. The steel tube was insulated with ceramic insulation to minimize heat loss from the system and to ensure the safety of personnel.

Figure 15: Schematic of the Experimental Facility for Sulfur Heat Transfer Analysis

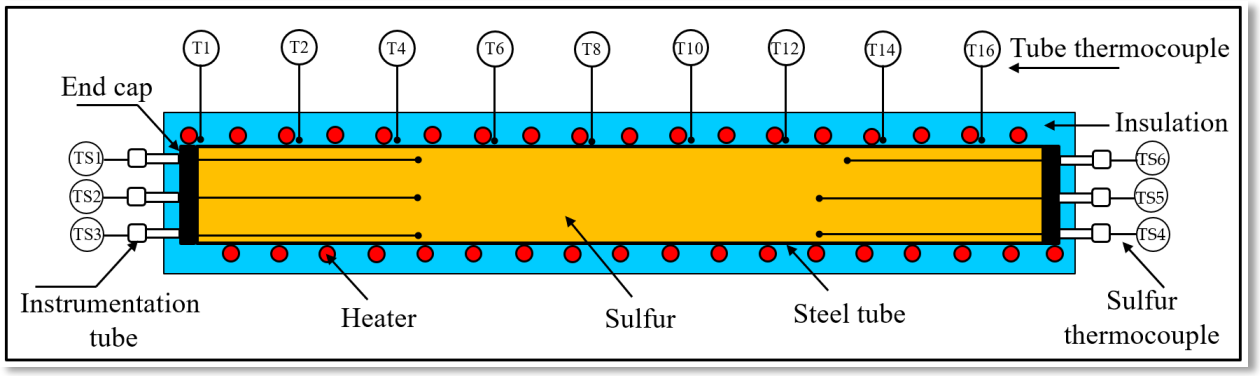

Source: UCLA, Wirz Research Group

Figure 16: Position of Sulfur and Tube Thermocouples

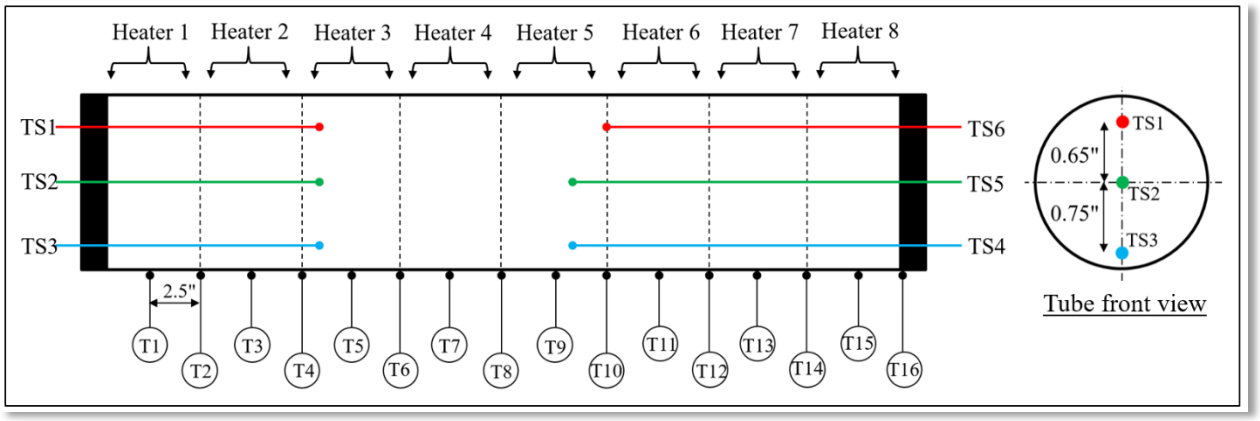

Source: UCLA, Wirz Research Group

Experimental Procedure

In this study, sulfur heat transfer behavior was investigated for two conditions: uniform and nonuniform thermal charging. For the uniform thermal charging, the tube surface was maintained at a uniform temperature without any spatial gradient. Initially, the tube surface was heated to 200°C until the sulfur temperatures achieved a steady state. Then, the tube surface was heated from 200 °C – 600°C at a predetermined ramp rate and sulfur temperatures were recorded until the entire system reached 600°C. For the nonuniform thermal charging, individual sections of the tubes (Figure 16) were heated to predetermined temperatures to establish a constant temperature gradient along the tube length with the hot end (heater 1) at 600°C and the cold end (heater 8) at 250°C. At the end of thermal charging, the heaters were turned off and the system was naturally cooled to room temperature.

Results and Discussion

In this section, the effect of sulfur properties and key physical mechanisms on the sulfur heat transfer behavior is discussed for uniform and nonuniform charging conditions using experimental, analytical, and computational techniques.

Uniform Thermal Charging

The uniform thermal charging condition represents the thermal charging in the cross-flow configuration of the SulfurTES battery. For this condition, a maximum possible temperature difference between HTF and sulfur can be achieved resulting in a superior heat transfer performance of sulfur.

In this study, the sulfur-filled steel tube was uniformly heated in two-stages, from 50 °C–200°C, and 200 °C–600°C, as discussed earlier. Figure 17a shows the temporal variation in the sulfur temperatures over 50 °C–200°C as recorded by thermocouples TS1, TS2, and TS3. In the early stages (up to ~10 minutes), the rates of temperature rise, recorded by TS1 and TS2 were lower compared to TS3. During this period, most of the sulfur mass was solid-state, thus, heat transfer within sulfur was dominated by the solid-state conduction with a thermal conductivity of 0.205 W/m-K [44]. As shown in Figure 16, TS3 was closest to the tube wall resulting in a higher ramp rate compared to TS1 and TS2. After this initial stage, the TS1 showed a rapid increase in the sulfur temperature from ~118°C to 175°C over a short period of ~three minutes. Similarly, TS2 recorded a rapid temperature rise from ~100°C to 170°C. During this rapid temperature rise of TS1 and TS2, the sulfur temperature recorded by TS3 remained quasi-steady with a slight temperature decrease (~5°C). At ~170°C, the sulfur thermocouples, TS1, and TS2 showed a sudden drop in the temperature ramp rate and continued to rise very slowly until 200°C. During this period, TS3 increased from ~125°C until it reached a steady state at 200°C.

In Stage II (Figure 17b) of the uniform thermal charging, sulfur showed a significantly higher thermal charge rate. Initially, the temperature difference between the heater and sulfur temperatures was noticeable, but it continued to decrease at higher temperatures. Moreover, the temperature difference between TS1, TS2, and TS3 was negligible beyond 500°C.

Figure 17: Temporal Variation in Sulfur Temperature in the Range of (a) 50—200°C, and (b) 200—600°C

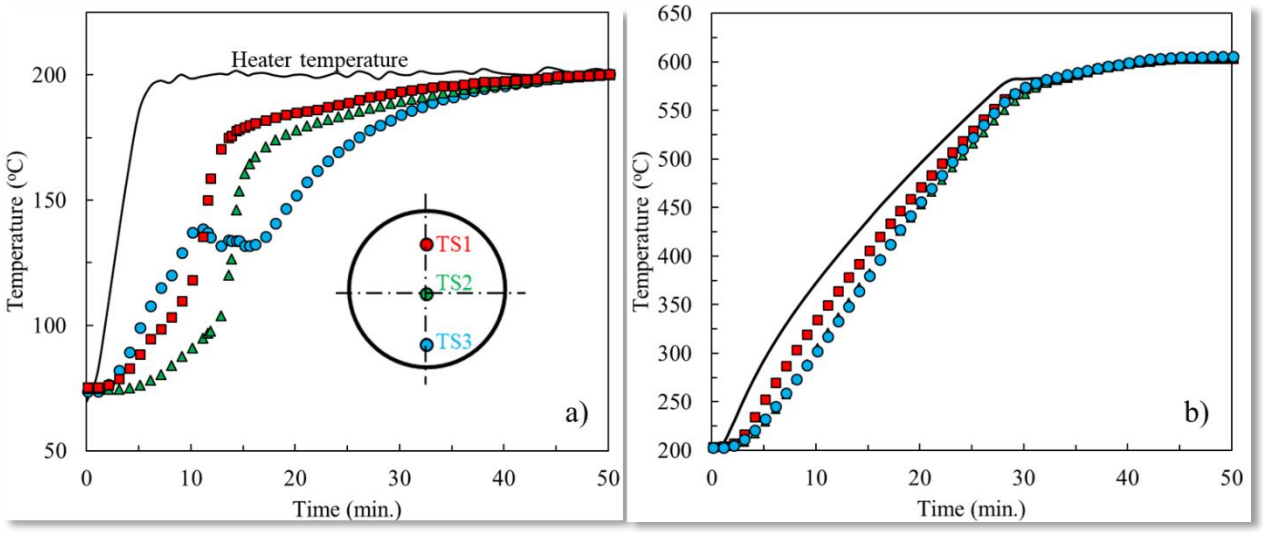

Source: UCLA, Wirz Research Group

The sulfur heat transfer behavior in the temperature range of 50 °C —200°C was governed by two important mechanisms: (1) solid-liquid phase change, and (2) a significant increase in the sulfur viscosity beyond 170°C. At temperatures higher than 200°C, the natural convection was a dominant mode of heat transfer characterized by the decrease in the sulfur viscosity.

Figure 18 shows the variation in the sulfur viscosity with temperature for two grades of sulfur: pure sulfur, and sulfur with 0.4 percent (molar concentration) of impurities. The viscosity of pure sulfur dramatically increased beyond 170°C and achieves a peak value at 200°C. The viscosity of sulfur with 0.4 percent impurities was significantly lower than that of pure sulfur, however, it showed similar variation with the temperature. The viscosity of doped sulfur increased beyond 170°C and achieved a peak value at ~270°C. This noticeable variation in the sulfur viscosity was reflected in the sulfur temperature evolution as shown in Figure 17. Nithyanandam et al., [45, 46] conducted a comprehensive computational analysis to investigate the sulfur heat transfer behavior for uniform and nonuniform charging conditions. These analyses showed that the computational model predictions are in greater agreement with experimental results for doped sulfur (0.4 percent impurities) with a lower viscosity as compared to the pure sulfur. As a result, henceforth, this report will refer to the viscosity of doped sulfur only.

Figure 18: Sulfur Viscosity Variation with Temperature

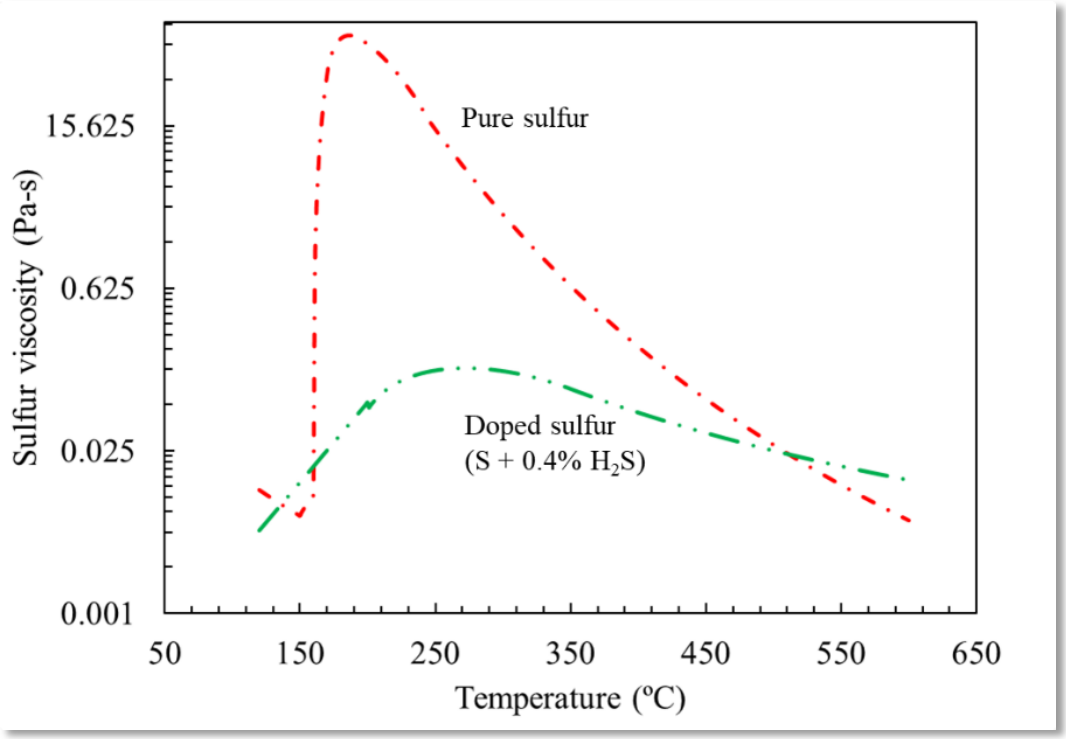

Source: American Chemical Society

The details of the computational model development are presented in an independent study [45,46]; however, results of the analysis are discussed here to explain the underlying physics of the sulfur heat transfer behavior. Figure 19 shows the temperature and flow contours within sulfur during thermal charging in the temperature range of 50 °C–200°C. In the initial stages, (~10 minutes), the sulfur at the inner wall of the steel tube melted and a layer of liquid sulfur was formed. In this peripheral region, buoyancy-driven convective currents were formed that transported the thermal energy from the wall to the sulfur. However, the impact of this convective heat transfer was limited to the liquid sulfur at the periphery, while heat transfer in the solid sulfur core was dominated by the solid-state conduction. As a result, the temperature recorded by TS3 was higher than TS1 and TS2, as shown in Figure 17. As thermal charging progressed, the solid-liquid front propagated through the sulfur mass, increasing the liquid sulfur fraction. Therefore, the intensity of the buoyancy-driven heat transfer increased, resulting in stronger convection currents, as shown in Figure 19. These convective currents transported hot liquid to the top region of the tube, where it discharged the thermal energy and descended to the bottom of the tube. Thus, the top region of the tube was preferentially heated, resulting in the rapid temperature rise of TS1 to ~175°C (Figure 17a). At this temperature, a sudden increase in the sulfur viscosity (Figure 18) dampened the convective currents and reduced the sulfur heat transfer rate, as evident from the low ramp rate of TS1 from 175 °C–200°C (Figure 17). During this period, the convective currents were restricted to the central region of the tube, preferentially heating TS2, as shown in Figure 19. The sulfur temperature TS2 followed a similar profile to that of TS1, as it was thermally charged to 200°C. During the rapid increase in TS1 and TS2, the sulfur temperature TS3 showed an unexpected plateau at ~136°C. During this period, the high-temperature sulfur was thermally discharged in the top and central region of the tube, and the bottom region received relatively

colder liquid sulfur. As a result, there was no thermal transport to the lower region of the tube until top and central regions, represented by TS1 and TS2, were thermally charged to ~170°C. As the sulfur heat transfer rate in the top and bottom regions slowed beyond 170°C due to a rise in sulfur viscosity, the buoyancy driven currents were restricted to the bottom region of the tube, resulting in the rise in sulfur temperature TS3 until it reached 200°C (Figure 17).

Figure 19: The Temperature and Flow Contours Within Sulfur During Thermal Changing

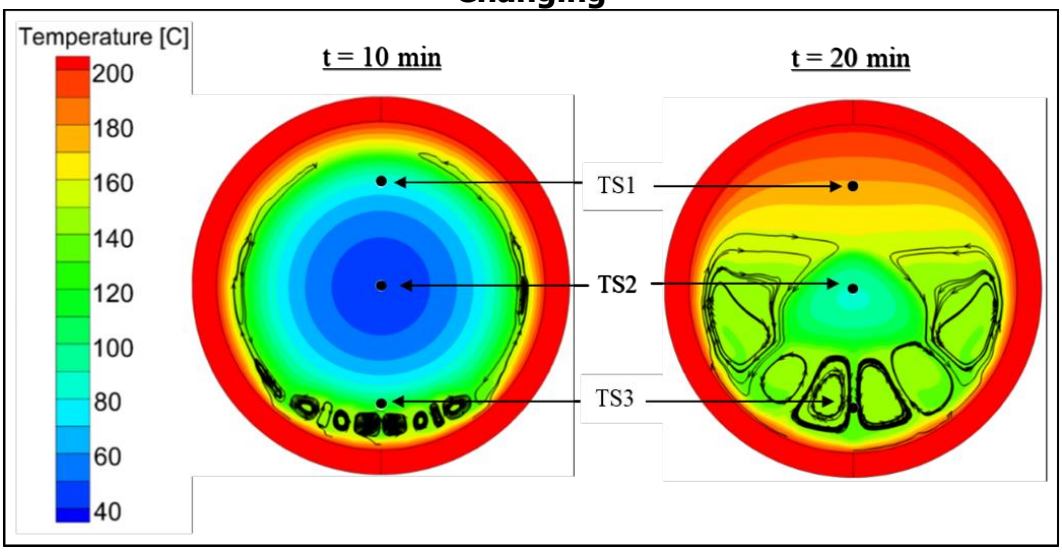

After 10 Minutes (Left) and 20 Minutes (Right) During Thermal Charging

Source: UCLA, Wirz Research Group

In Stage II of the thermal charging, all sulfur temperatures followed a similar profile over 200°C–600°C. Initially, the sulfur and tube temperatures showed a noticeable difference due to a rise in sulfur viscosity until 270°C (Figure 18). Beyond this temperature, the sulfur viscosity continuously decreased, resulting in a higher heat transfer rate and a decrease in the difference between wall and sulfur temperatures. The buoyancy-driven convective structures developed within sulfur during thermal charging were found in the computational heat transfer.

The effect of distinct heat transfer mechanisms in Stage I and Stage II of the uniform thermal charging was realized through the time delay for the sulfur temperatures in attaining the steady state temperature. The time delay for TS1 was defined as,

$$\textit{Time delay (TS1)} = t(\textit{surface temperature} = \textit{set point}) - t(\textit{TS1}=\textit{set point})$$

The time delay for sulfur temperatures in Stage I (50 °C–200°C) was ~35 minutes, an order of magnitude higher than the time delay of ~3 minutes for Stage II (200 °C–600°C). The longer time delay in Stage I was a result of poor solid-state conduction within sulfur and weak convective heat transfer at temperatures greater than 170°C. In Stage II, low-viscosity liquid sulfur was thermally charged via buoyancy driven natural convection, resulting in the high thermal charge rate and a lower time delay. This analysis indicated that temperature range of 200 °C–600°C was suitable to operate SulfurTES systems to achieve a superior heat transfer performance.

Nonuniform Thermal Charging

For the nonuniform thermal charging, a constant axial temperature gradient was imposed on the tube surface with the hot end at 600°C and the cold end at 200°C. As shown in Figure 20a and 20b, the actual tube temperatures, especially in the relatively colder region, were higher than the imposed temperatures, indicating the transport of thermal energy from the hot end to the cold end of the tube. Initially, the solid-state conduction through the steel tube was considered as the mechanism for this axial heat transfer, and the analytical solution was developed (see Appendix A) to assess its impact. Figure 20c shows the evolution of tube temperatures at various axial locations with time. Although the conduction heat transfer increased the tube temperatures from the initial value, it was not sufficient to achieve the steady state tube temperatures achieved after 2.5 hours of thermal charging (Figure 20c). At this time the temperature distribution due to the conduction heat transfer was significantly lower than the actual temperatures, and it would take ~15 hours for conduction heat transfer alone to heat the tube to the temperatures observed during the experiments. Thus, another dominant heat transfer mechanism should be used for the axial distribution of the heat that resulted in the higher tube temperatures. The thermal diffusivity of sulfur was an order of magnitude lower than SS316 (Table 5) and, therefore, solid-state conduction through sulfur was practically negligible.

Table 5: Thermal Properties of SS316 and Sulfur

Material property	SS316	Sulfur
Thermal conductivity (W/m-K)	20	0.2
Density (kg/m^3)	8000	1685
Specific heat capacity (J/kg-K)	550	1165
Thermal diffusivity (m^2/s)	$4.5*10^{-6}$	$1.02*10^{-7}$

Source: Freeport Sulphur Company

Figure 20c and 20d show the evolution of the sulfur temperatures during thermal charging and compare it with corresponding tube temperatures at the similar axial positions (Figure 16). Moreover, Figure 20f shows the steady state temperature distribution along the tube surface as well as the sulfur temperatures, TS1-TS6. Figure 20f reveals that the temperatures, TS1, and TS5 are higher than the wall temperature at an identical axial location, while TS2, TS3, TS4, and TS6 are the same as or lower than wall temperatures. These observations further strengthen the hypothesis of thermal energy transport within sulfur from a hot end to the cold end of the tube. In the absence of a significant contribution from conduction heat transfer, axial natural convection is a possible heat transfer mechanism for the axial thermal transport within the sulfur mass.

Figure 20: Temperature Distribution for Axial Temperature Gradient

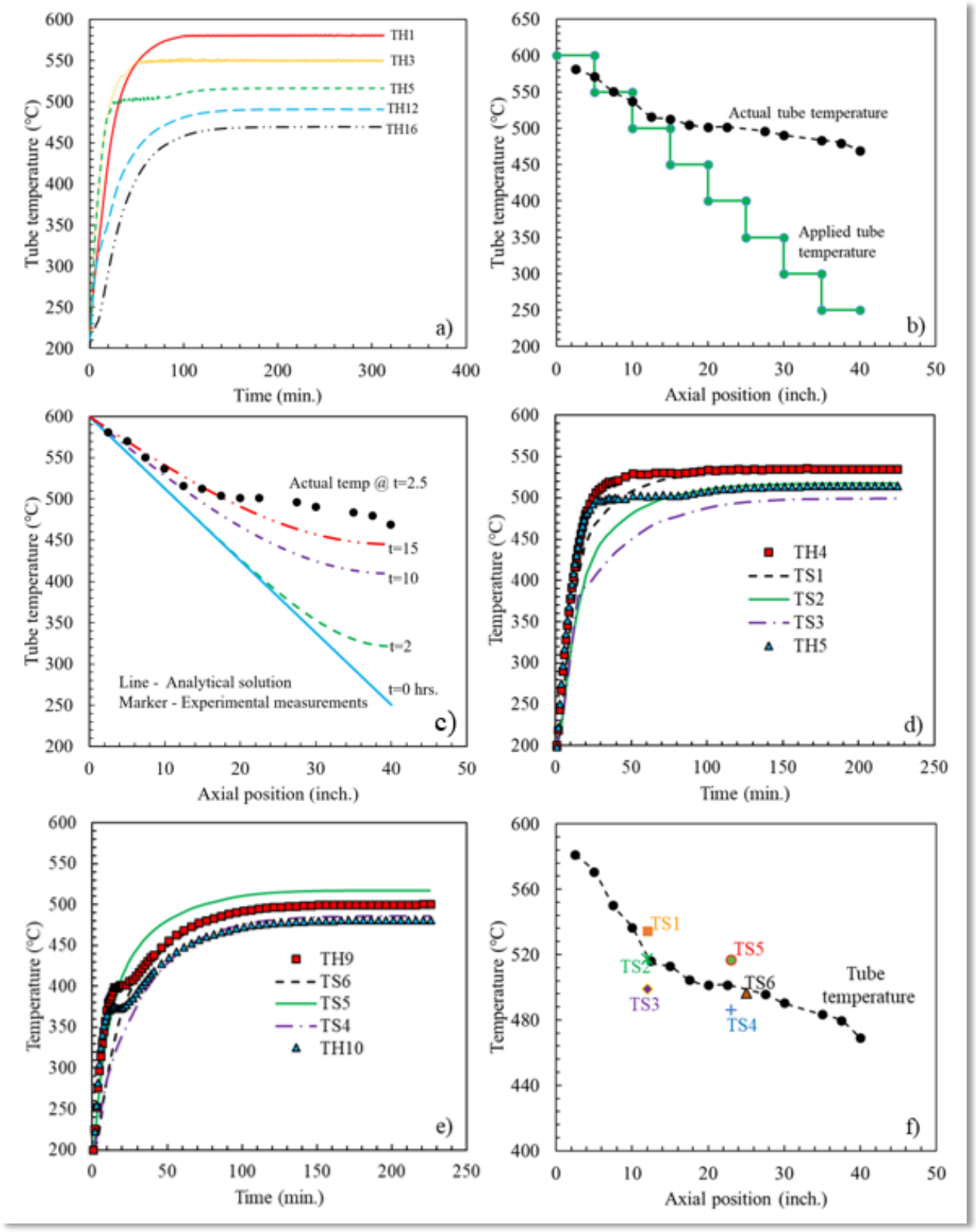

Source: UCLA, Wirz Research Group, Wirz Research Group

Computational Heat Transfer Analysis

In order to understand the heat transfer characteristics of sulfur at temperature ranges of 50°C to 600°C — applicable for CSP, waste heat recovery, low temperature power cycles, such as an organic Rankine cycle, geothermal applications, CHP, and so on — a detailed computational model solving for the conjugate heat transfer and solid-liquid phase change dynamics of the sulfur based thermal energy storage system was developed. This model elucidated the complex interplay between the governing heat transfer and fluid flow phenomena during charge and discharge operations. Within the temperature range of interest, sulfur exhibited two important characteristics: the solid-liquid phase transition at Tm = 119℃ [43] and the significant change in viscosity of molten sulfur due to polymerization in liquid phase [44]. The variation in the viscosity of the molten sulfur as a function of temperature is shown in Figure 18 for two purity grades of sulfur. The red line denotes the viscosity variation of pure sulfur as reported by Bacon and Fanelli [47] while the green line denotes the viscosity variation of sulfur with trace amount of dopant (H2S, for example), which resulted in a significant decrease (order of ~103) in the viscosity spike as reported by Fanelli [48], Rubero [49], and Timrot et al. [50]. The two viscosities were selected to understand the sensitivity of the viscosity parameter on the prediction capability and accuracy of numerical model to experimental results. The temperature-dependent thermo-physical properties of sulfur were obtained from the literature [43,44,51].

Numerical Model

The computation domain considered is shown in Figure 21. Sulfur was stored inside the circular two-inch NPS SS316 pipes of schedule 40 thickness, as explained in the section on experimental setup. The melting and solidification process of sulfur was modeled by the enthalpy-porosity technique as introduced by Voller, et al. [52]. With this approach, the porosity in each cell was set equal to the liquid fraction, γ, in the cell, which takes either the value of 1 for a fully liquid region, 0 for a solid region, or 0 < γ < 1 for a partially solidified region (mushy zone). The coupled system of continuity, momentum, and energy equations governing the thermo-fluidic behavior of sulfur in the temperature range of 50 °C–600°C can be presented in a unified manner as follows:

$$\textit{Continuity:} \qquad \nabla \cdot \left(\rho \vec{V}\right) = 0$$

$$\textit{Momentum:} \qquad \rho \frac{D\vec{V}}{Dt} = -\nabla p + \nabla \cdot \bar{\bar{\tau}} + S_g$$

$$\textit{Energy:} \qquad \rho c \frac{DT}{Dt} = -\nabla \cdot (k \Delta T) + S_h$$

where ρ is the phase density, k is the thermal conductivity of the PCM, p is the pressure, t denotes time, T is the temperature, $\vec{V}$ denotes the superficial velocity vector with components u, and v in the x-, and y- directions, respectively, and $\bar{\bar{\tau}}$ is the stress tensor. The momentum equation incorporates a source term for natural convection $S_g = \rho \vec{g} \beta (T - T_{ref}) - A(\gamma)\vec{V}$ in which the second term includes a porosity function, $A(\gamma) = C(1-\gamma)^2/(\gamma^3 + \varepsilon)$ to mimic the Carman-Kozeny equation for flow in a porous media, where ε = 0.001 is a small computational constant to avoid division by zero and C is a constant reflecting the morphology of the melting front, set to be 1.6×10^6; g is the gravity vector; and β is the thermal expansion coefficient of

sulfur. The latent heat source term is incorporated in the energy equation as $S_h = \rho \frac{\partial \Delta H}{\partial t}$ where the change in latent enthalpy takes the value of, $\Delta H = \gamma h_{sl}$ where $h_{sl} \sim 52$ kJ/kg denotes the latent heat content of sulfur [43]. For the wall of the SS316 pipe only the energy equation with $S_h = 0$ was solved. The density, specific heat and thermal conductivity of SS316 pipe were 7900 kg/m3, 559.9 J/kg-K and 20.1 W/m-K, respectively.

The numerical model was solved in ANSYS Fluent 14.0. The computational grid was built of quadrilateral cells in the wall, and fluid (sulfur) region (Figure 21), with mesh density greater than 700 cells/cm2 (typically cell elements of 4,000—250,000 for the pipe sizes were considered in this study) were determined based on a systematic grid refinement process. The ANSYS Fluent SIMPLE algorithm was used for the pressure-velocity coupling and the time step in the calculation was set at 0.1 second, since further decrease did not show any noticeable changes in the transient results for the temperature and velocity. The convective-diffusive terms in the momentum and energy equations was solved using the second-order upwind scheme. At each time step during the simulation, residual convergence values of 10^{-6} and 10^{-4} were imposed for the momentum and continuity equations respectively, and a value of 10^{-8} was used for the energy equation. To accurately predict the liquid fraction in the fixed-grid enthalpy-based procedure, the latent heat content of each computational cell, ΔH_i in conjunction with the temperature predicted by energy equation, was updated at each iteration within a time step using a user-defined function (UDF) [53].

Figure 21: Computational Domain

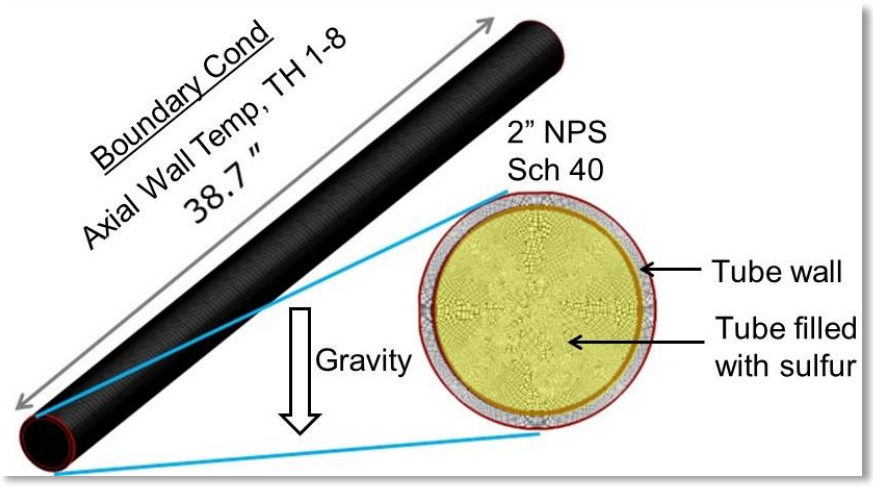

Source: UCLA, Wirz Research Group, Wirz Research Group

Component Level Heat Transfer Analysis

The computational model was validated by comparing the simulated results obtained for thermal charging of sulfur stored inside stainless-steel pipes. The details of the experimental test facility with resistive heating fabricated for validation of the computational model are discussed in the experimental set up section. Following model validation, the computational model was to investigate the heat transfer mechanism inside the storage pipes of the sulfur-based TES system for temperature ranges between 200℃ and 600℃ which may be of interest to many important applications, such as high temperature CSP, and industrial CHP.

Model Validation with Uniform Surface Temperature Experiments

Since the experiment involved constant set-point temperatures and the internal thermocouples (TS1-3 in Figure 16) were well inside the tubes to be influenced by end effects, a two-dimensional model was relevant. The transient wall temperature profile measured using the surface thermocouples in the experiments was imposed as a boundary condition for the numerical model. The results obtained from the computational model for the temporal variation in temperature at the location of the internal thermocouples TS1, TS2, and TS3 were compared with the experimental results as shown in Figure 22 and Figure 23. The computational result obtained using the high viscosity variations for pure sulfur reported by Bacon and Fanelli [47] is depicted as a chain-dashed line, while the numerical result obtained using the low-viscosity variations for sulfur with trace amounts of dopant such as H_2S [48-50] is shown as the solid line, and the experimental results are denoted by markers. The predictions of the trends in temporal variation of sulfur temperatures concurred well with experimental results.

Figure 22: Comparison of Numerical Results with Experimental Results for a Wall Surface Set Point Temperature of 200°C

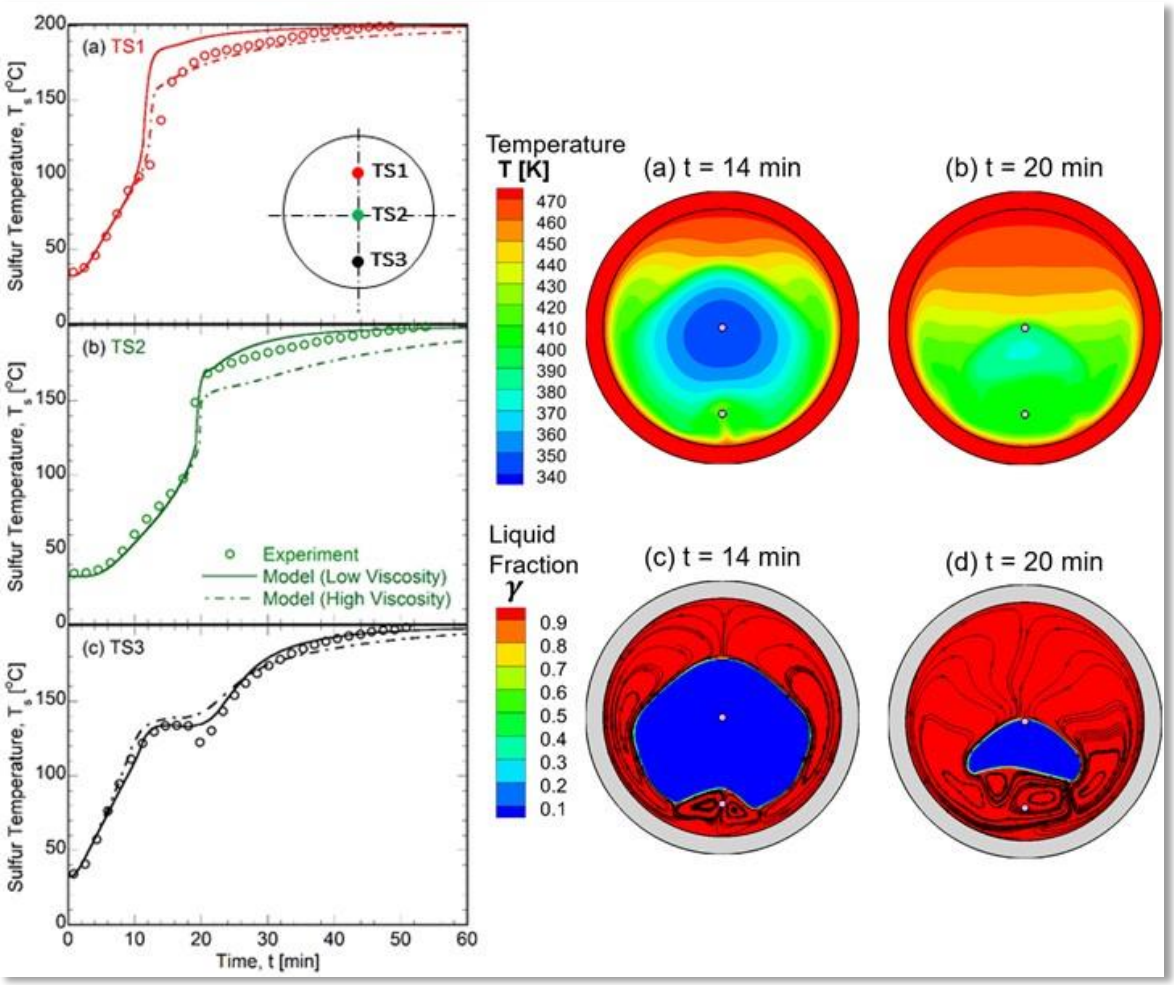

Contours of Temperature, and Liquid Fraction, Along with Velocity Streamlines for the Experimental Conditions Used for the Validation of Numerical Model, are also shown.

Source: UCLA, Wirz Research Group

An interesting trend observed in the study was that the temperature of the bottom thermocouple (TS3) in Figure 22 stayed at a constant temperature between ~10 to 20 minutes. However, the constant temperature was not at the phase transition temperature, but at a slightly higher temperature. The liquid fraction contour plots presented in Figure 22 can explain this. As seen from contour plot Figure 22d, the buoyancy driven convection currents were restricted to small convection cell pockets, due to the high viscous regime surrounding the pipe wall. The convection pockets near the bottom thermocouple rose from the vicinity of high viscous molten sulfur layer to the cold solid sulfur, where it lost its thermal energy in melting the solid sulfur and returns to the bottom at a lower temperature. Due to the finite heat transfer resistance at the interface between the rising hot molten sulfur and the cold solid sulfur, it cooled to a temperature slightly higher than the phase transition temperature. Hence, the bottom thermocouple saw a constant feed of uniform cold temperature that was slightly higher than Tm between the time periods of 10 to 20 minutes as shown in Figure 22c.

Figure 23: Comparison of Numerical Results with Experimental Results for Wall Surface Set-Point Temperature Of 600°C

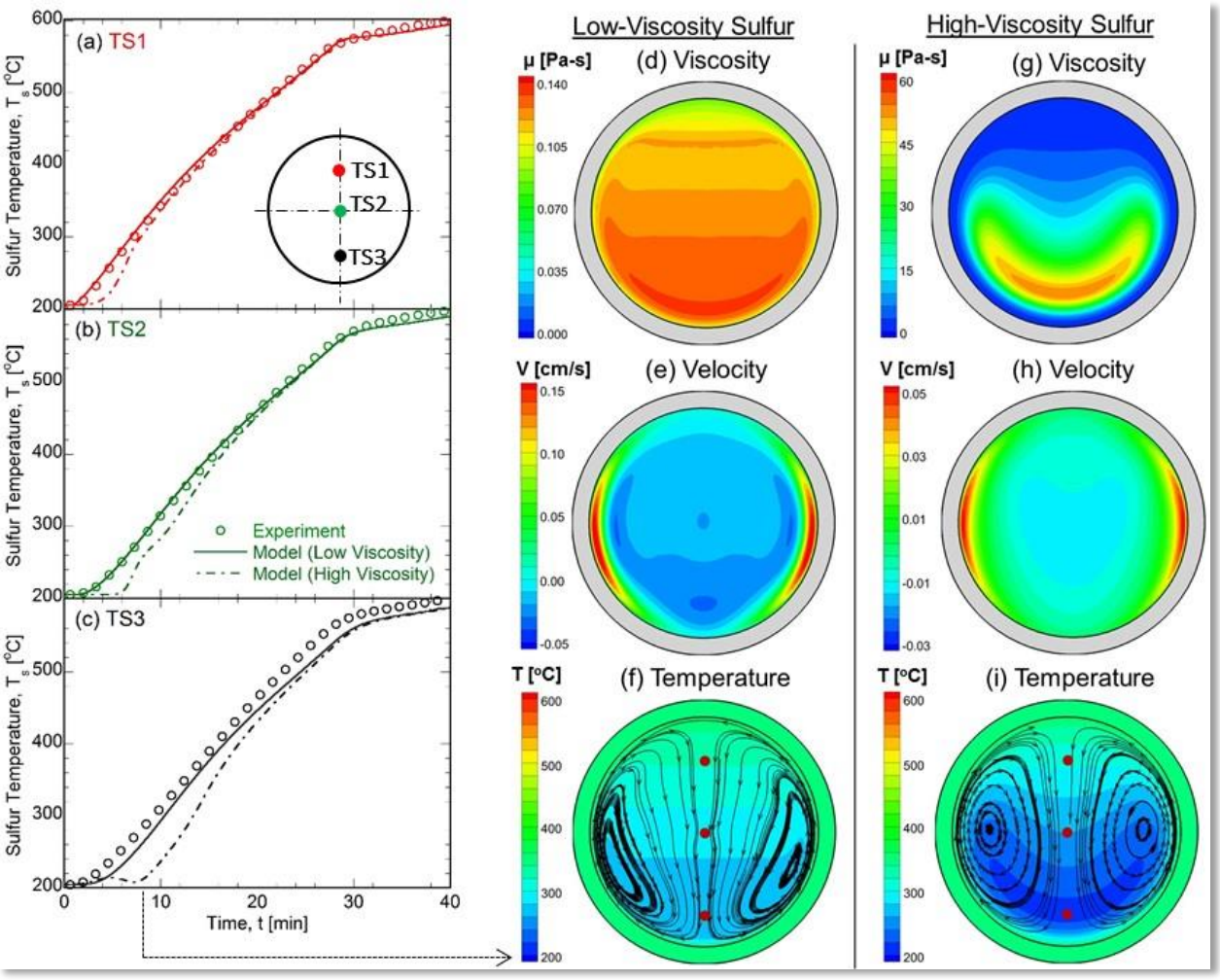

Contours of (D,G) Temperature, (E,H) Velocity, and (F,I) Viscosity Obtained for Low-Viscosity and High-Viscosity Sulfur at Time Instant of *T* = 8 Minute.

Source: UCLA, Wirz Research Group

Figure 23d and 23f depict the viscosity, velocity, and temperature contours at a time instant of eight minutes for low-viscosity sulfur, while the contours illustrated in Figure 23g, 23h, and 23i correspond to high-viscosity sulfur. The locations of the thermocouples TS1-3 are shown by the white circles in the temperature contours. The low viscosity of sulfur with dopants (Figure 23d) relative to that of pure sulfur (Figure 23g) contributed to stronger convection currents as observed by the difference in magnitude of velocity (Figure 23e and h). This culminates in a slower evolution of temperature field in high-viscosity sulfur (Figure 23f) compared to low-viscosity sulfur (Figure 23). Hence, the predicted temperatures at the thermocouple locations were lower for high-viscosity sulfur (Figure 23a-c) compared to experimental results, especially at temperatures between 200—400°C. At later time instants, the temperature predictions from both high- (pure sulfur) and low- (doped sulfur) viscosity models converged, because of relatively smaller difference in viscosity values at high temperatures (Figure 18). Overall, the sulfur viscosity with trace amounts of dopants agreed very closely with the experimental result for the full temperature range of room temperature to 600°C.

Results and Discussion

Uniform Temperature Distribution

A parametric study of the effects of pipe diameter on the charge and discharge performance of the storage system was conducted. For the case of charging, the initial and the outer wall boundary temperatures were 200℃ and 600℃, respectively and vice-versa for discharging. The contour plots in Figure 24 show the temperature profile and the streamlines of the buoyancy-driven flow field for various pipe diameters during charge (Figure 24a-d) and discharge (Figure 24e-h) at time instants corresponding to when the mean temperature of sulfur is 400℃. The buoyancy-driven flow field during charge was characterized by a pair of counter-rotating vortices with rising flow along the hot pipe wall for small pipe diameters (Figure 24a-c) and an additional pair of secondary vortices were formed near the bottom of the pipe for larger pipe diameters (Figure 24d). Counter-rotating vortices were also formed during discharge (Figure 24e-h) with the flow descending along the cold pipe wall. In contrast to charge, the secondary vortices at larger pipe diameter were established near the top of the pipe (Figure 24g and h) because of the reversal in rotation direction of the recirculation cells. The cooling of sulfur from high temperature (60℃) and low-viscous state (Figure 18) during discharge was accompanied by higher activity of the natural convection currents initially that lead to the onset of secondary vortices at comparatively smaller pipe diameters (Figure 24e-h) than during thermal charge process (Figure 24a-d). The secondary convection cells were most likely induced by curvature-driven centrifugal instability that took the form of counter-rotating Taylor-Görtler vortices [54] and were observed for larger pipe diameters (larger Rayleigh number).

Figure 24: Streamlines of the Buoyancy-Driven Flow and the Temperature Contours for Different Pipe Diameters at Time Instants Corresponding to Mean Sulfur Temperature Of 400°C

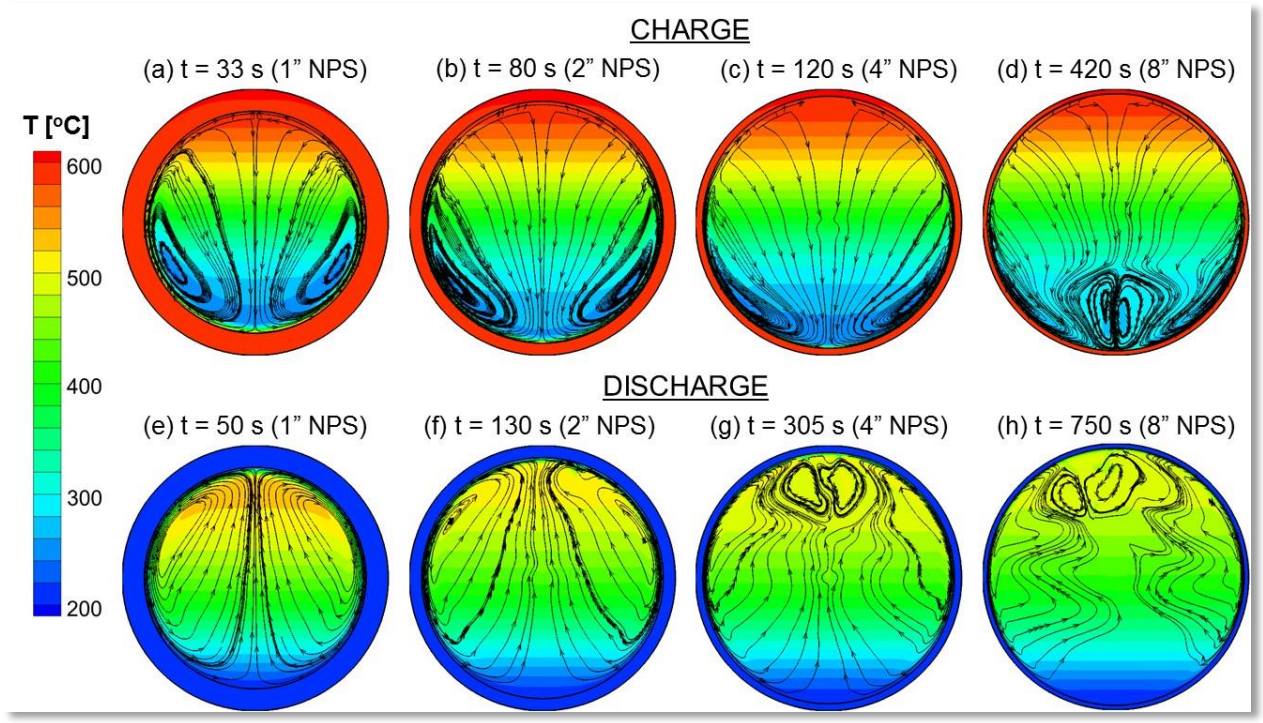

Source: UCLA, Wirz Research Group

Figure 25: Transient Evolution Sulfur for Various Pipe Diameters

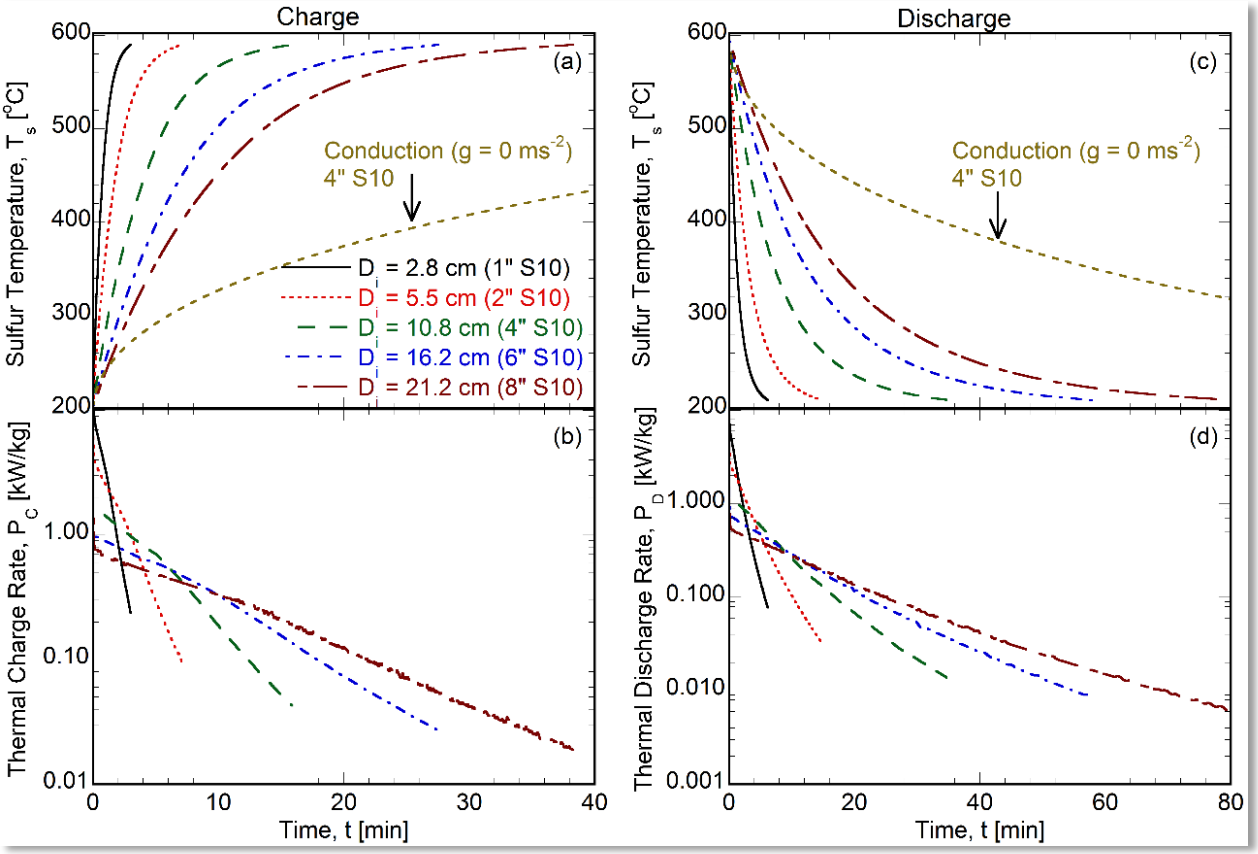

(a) sulfur temperature, (b) charge rate during thermal charge process, and (c) sulfur temperature, (d) discharge rate during thermal discharge process for various pipe diameters.

Source: UCLA, Wirz Research Group

Figure 25a and 25c present the temporal evolution of volume-averaged temperature of sulfur during charging and discharging, respectively for various pipe dimensions. The temporal variations were illustrated until the dimensionless mean temperature of sulfur defined as $\theta_s = \frac{(T_s - T_D)}{(T_C - T_D)}$, reached 0.95 and 0.05 for charge and discharge, respectively. Additionally, the predictions of the numerical model for pipe diameter of D_i = 0.108 m corresponding to 4-inch NPS schedule 10, without accounting for the buoyancy-driven convection currents (g = 0 ms-2) was also plotted to emphasize the role of buoyancy-driven convection currents in augmenting the charge and discharge performance. In general, with increase in pipe diameter, it took more time to charge and discharge, primarily due to the increase in energy content within the pipe. As explained earlier, the buoyancy-driven convection currents assisted in improving the charge and discharge performance as seen by the longer charge and discharge times observed for conduction dominated case in Figure 25a and c. Completion of discharge process took longer than charge as observed from comparing Figure 25a and c. The temperature difference between the wall and sulfur ($T_w - T_s$) was the driving force for charge and discharge process, which decreased with time. In contrast to charge, the increase in viscosity with decreasing sulfur temperature near pipe wall combined with decreasing driving force during discharge moderated the intensity of convection currents, resulting in slightly longer discharge time compared to charge.

Figure 25b and Figure 25d depict the instantaneous specific thermal charge and discharge rate of sulfur, respectively, which followed the slopes of transient evolution of temperature curves (Figure 25a and Figure 25c). The rates of thermal charge and discharge were initially higher due to the strong effects of buoyancy-driven convection currents (Figure 25b and Figure 25d). With progression of time, the slope reduced, due to the slowdown of the activity of natural convection currents with a concomitant decrease in the temperature difference between the wall and temporally varying sulfur (Figure 25a and Figure 25c). For a given pipe diameter, thermal charge rate was slightly higher than discharge rate, owing to the reasons mentioned earlier for the relatively longer completion of discharge compared to charge. The specific rates of thermal charge and discharge were higher for smaller pipe diameters, due to larger surface area per unit volume of pipe. Small temporal oscillations materialized at larger pipe diameters — observed for 8-inch NPS in Figure 25b and Figure 25d — due to the weak turbulent effects in the transitional natural convection regime.

System performance for various pipe diameters was quantified in terms of charge and discharge time, charge and discharge average thermal convective conductance, and the Nusselt number in Figure 26. The thermal convective conductance was higher for larger pipe diameters compared to smaller pipe diameters, because of the higher surface area available for heat transfer interaction between the wall and sulfur, and stronger convection currents due to a larger Rayleigh number (Figure 26b). The Nusselt number in Figure 26c increased with greater pipe diameter or Rayleigh number. The Nusselt number for discharge was lower than charge for reasons mentioned earlier. Nevertheless, depending on the Rayleigh number, the average Nusselt number obtained for discharge was 3 to 15 times higher than competing molten salt PCM-based technologies ($Nu_{avg} \sim 8$) that were glacially slow in their discharge performance due to conduction-based solidification and low thermal conductivity [55]. Overall, elemental sulfur showed a rapid thermal charge and discharge rate of sulfur and did not require the expense and complexity of heat transfer enhancement techniques. A validated fundamental correlation for the Nusselt number as a function of the Rayleigh number for charge and discharge was also developed. It can be used to effectively design the sulfur-based thermal storage system for transient operation, which is discussed in Reference [45].

Figure 26: Influence of Pipe Diameter on Charge and Discharge Times

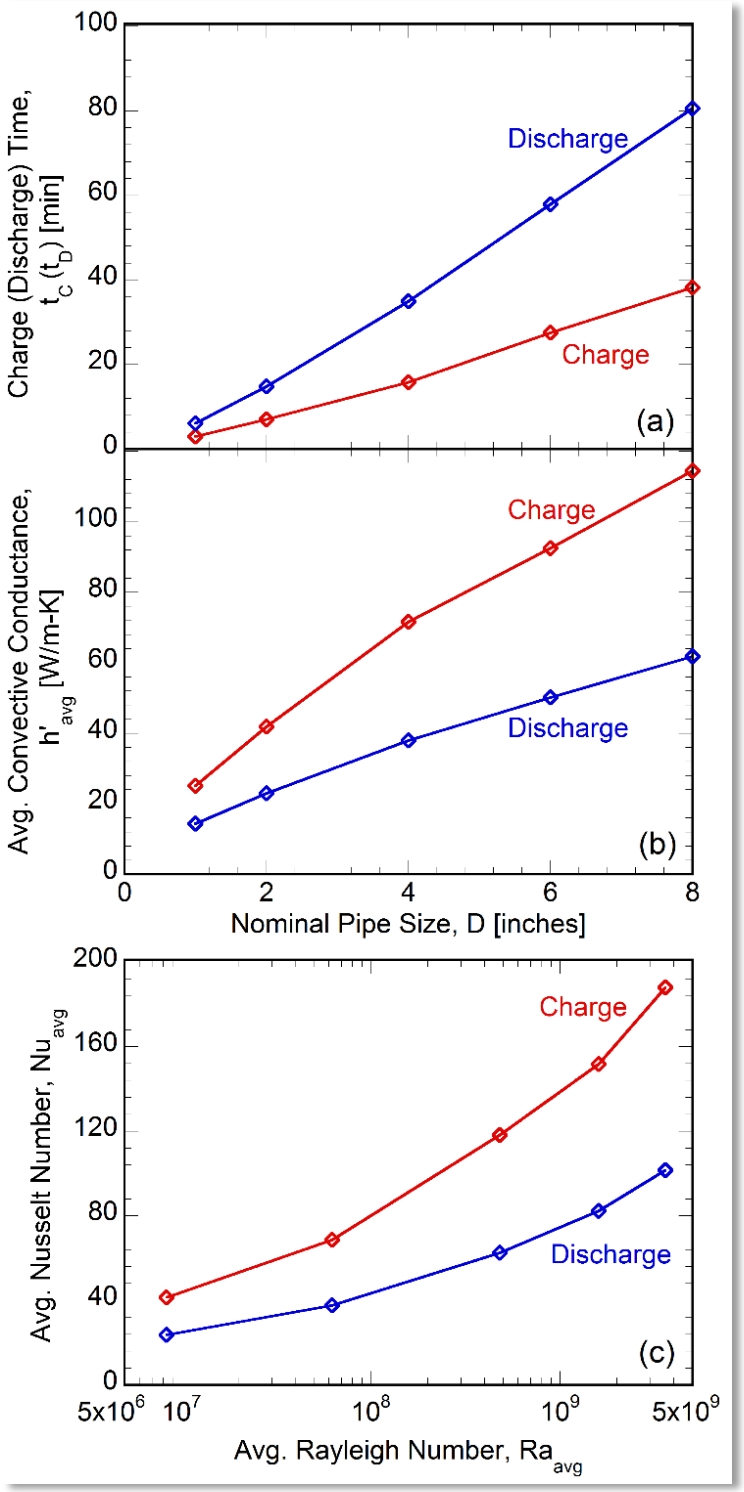

(a) Charge and Discharge Time, (b) Average Thermal Convective Conductance; and (c) Variation of Average Nusselt Number with Average Rayleigh Number.

Source: UCLA, Wirz Research Group

Axial Temperature Distribution

The results obtained from the numerical model are compared with the experimental results for the constant axial gradient experimental condition as explained earlier in the experimental procedure section. Researchers observed from Figure 27 that a good agreement exists between the numerical and experimental results. The top thermocouple (TS1) recorded the highest temperature, while the bottom thermocouple (TS3) recorded the lowest temperature due to natural convection currents (Figure 27a). The sulfur temperature measured by TS1-TS5 closely followed the surface temperature at respective axial positions, as shown in Figure 27. Thus, the axial temperature gradient was established within sulfur that contributes to the heat transfer within sulfur. This is also confirmed by the snapshots of temperature contours illustrated in Figure 28a. The influence of axial convection within sulfur can be realized from the fact the temperatures recorded by TS1 and TS5 were higher than the corresponding surface temperatures at identical axial position. However, from numerical simulation results, the team inferred that the axial temperature gradient gave rise to axial pressure and shear stress gradient that contributed to the formation of axial convection currents (Figure 28). Thus, the study concluded that the axial convection played a significant role in the redistribution of the thermal energy, and its effect must be realized in the design of the thermal storage system.

The researchers proposed a novel, thermally segregated monolithic thermal energy storage system design in an effort to minimize the redistribution of energy within the storage system — due to axial conduction and axial convection currents — and maximize the exergetic efficiency of the system [56].

Figure 27: Comparison of Numerical and Experimental Results of Sulfur Temperature

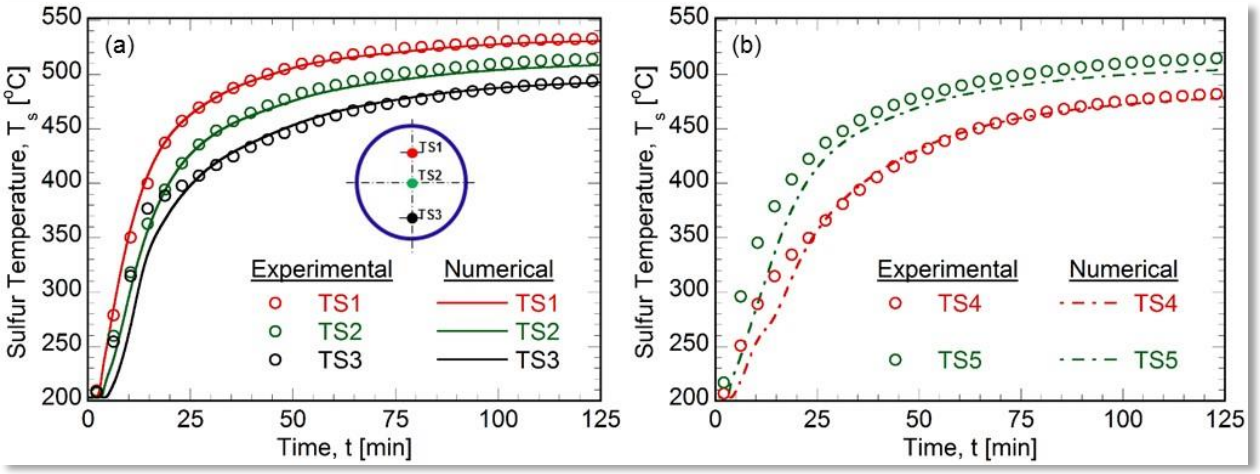

Source: UCLA, Wirz Research Group

Figure 28: Temperature and Flow Contours of Axial Convection Within Sulfur

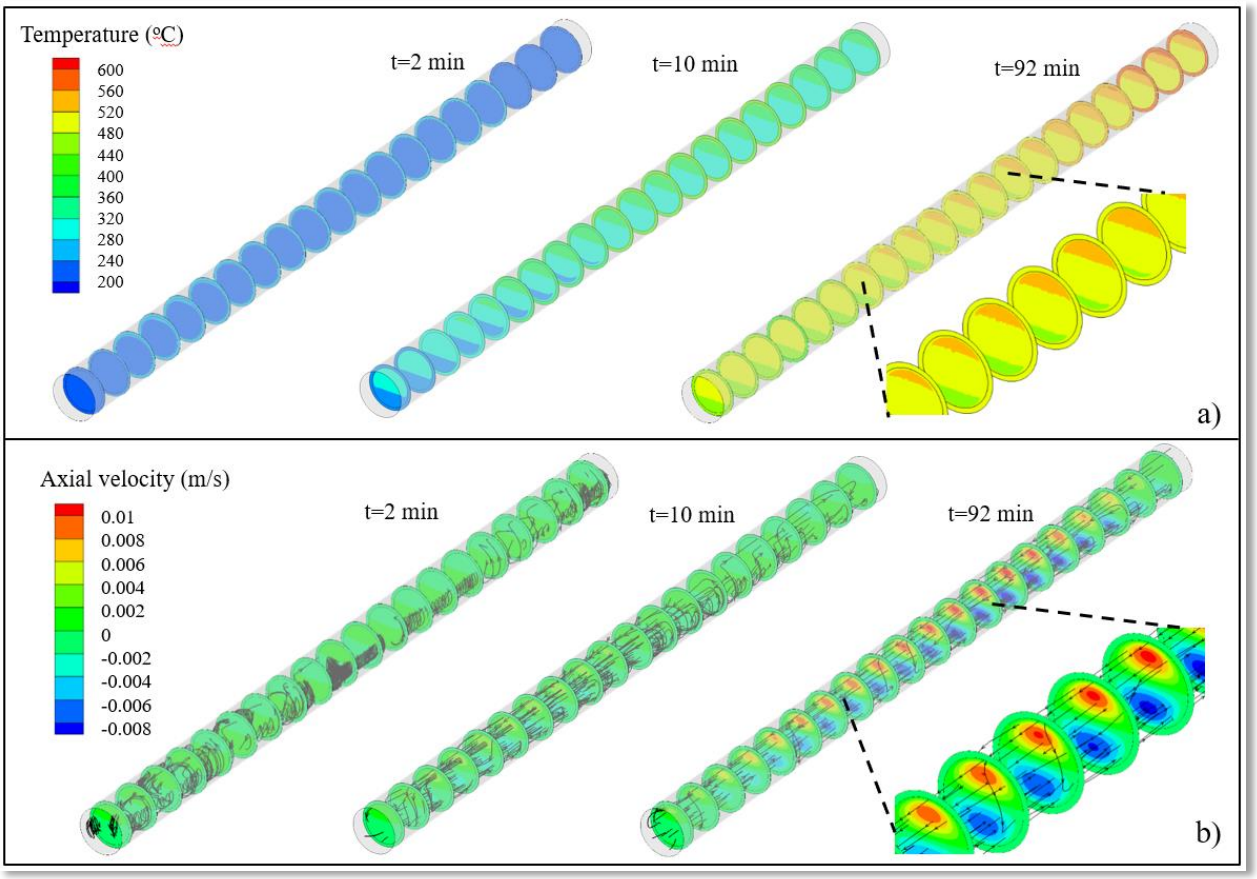

Source: UCLA, Wirz Research Group

System Level Heat Transfer Analysis

A numerical model involving a 3D computational domain of the thermal battery was developed to study the system level performance. The experimental measurements from the full cycle testing as reported in the *Task 6: Lab Demo Report* were used for validation of the numerical model. The model was then used to provide insights to the HTF flow and temperature distribution within the thermal battery during thermal charge and discharge operation.

Numerical Model

The three-dimensional computation domain considered in this study as shown in Figure 29 includes the shell for the HTF flow, sulfur tubes, and baffles. The coupled system of continuity, momentum and energy equations governing the thermo-fluidic behavior of HTF (air) can be presented in indicial notation as follows:

$$\textit{Continuity (Air):} \qquad \frac{\partial \rho}{\partial t} + \frac{\partial (\rho v_j)}{\partial x_j} = 0$$

$$\textit{Momentum (Air):} \qquad \frac{\partial (\rho v_i)}{\partial t} + \frac{\partial (\rho v_j v_j)}{\partial x_j} = -\frac{\partial P}{\partial x_j} + \frac{\partial}{\partial x_j}\left[(\mu)\left(\frac{\partial v_i}{\partial x_j} + \frac{\partial v_j}{\partial x_i}\right)\right] + \rho g_i$$

$$\textit{Energy (Air):} \qquad \frac{\partial (\rho H)}{\partial t} + \frac{\partial (\rho v_j H)}{\partial x_j} = \frac{\partial}{\partial x_j}\left[(\lambda)\frac{\partial T}{\partial x_j}\right]$$

where v_i, P, H, and T represent the mean velocity, pressure, enthalpy, and temperature, respectively. ρ, μ and λ denotes the density, viscosity, and thermal conductivity of the fluid. For the sulfur within the tubes only the energy equation was solved with an enhanced thermal conductivity that accounted for the heat transfer enhancement due to the buoyancy-driven convection currents within sulfur as informed by experimental and numerical efforts discussed earlier in the Results and Discussion and Component Level Heat Transfer Analysis sections. In the case of stainless-steel tube wall, only the conduction equation was solved.

Energy (sulfur): $$\rho_s c_s \frac{\partial T}{\partial t} = \lambda_{s,eff} \frac{\partial^2 T}{\partial x_i^2}$$

Energy (SS wall): $$\rho_w c_w \frac{\partial T}{\partial t} = \lambda_w \frac{\partial^2 T}{\partial x_i^2}$$

Figure 29: Computational Domain

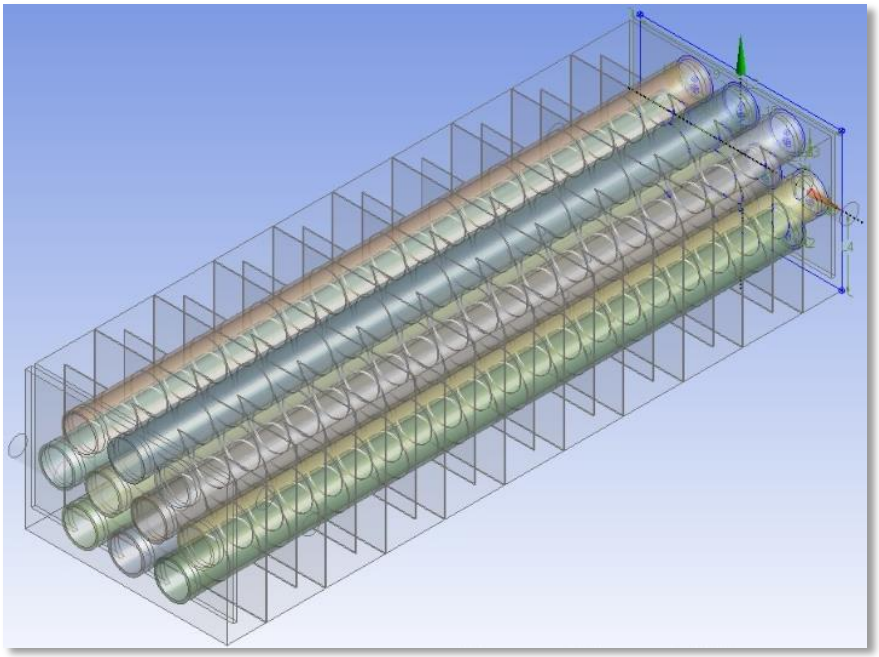

Source: UCLA, Wirz Research Group

The numerical model was solved in ANSYS Fluent 14.0. The computational grid was built of ~2.5 million — 3 million tetrahedral elements. The SIMPLE algorithm was used for the pressure-velocity coupling and the time step in the calculation was set at 0.5 second, since further decrease did not show any noticeable changes in the transient results for the temperature and melt fraction. At each time step during the simulation, residual convergence values of 10^{-5} and 10^{-3} were imposed for the momentum and continuity equations respectively, and a value of 10^{-6} was used for the energy equation.

Model Validation

The results from the numerical model were compared with experimental results obtained for one of the cycles. The boundary condition for the numerical model involved the inlet air mass flow rate and temperature recorded during the experimental runs. Figure 30 borrowed from Chapter 5 shows the location of the thermocouples within the thermal battery. Sulfur temperatures were recorded using 19 sulfur thermocouples. TS1 to TS9 were in direct contact

with sulfur, while TH1 through TH10 were integrated with the cartridge heaters embedded in steel tubes. Further details of the thermal battery setup can be found in Chapter 5 and is not repeated here. Figure 31 compares the temperature measurements obtained from numerical model with those of the experiments at various locations within the thermal battery. In general, this study observed that there was a good agreement between the experimental and numerical results within the calculated experimental and numerical uncertainties. The contour plots showed the temperature field in the thermal battery and the liquid fraction of sulfur at different axial location within the tubes at a time instant of 75 minutes.

Figure 30: Position of Thermocouples within SulfurTES Battery for Measurement of Sulfur and Steel Tube Temperatures

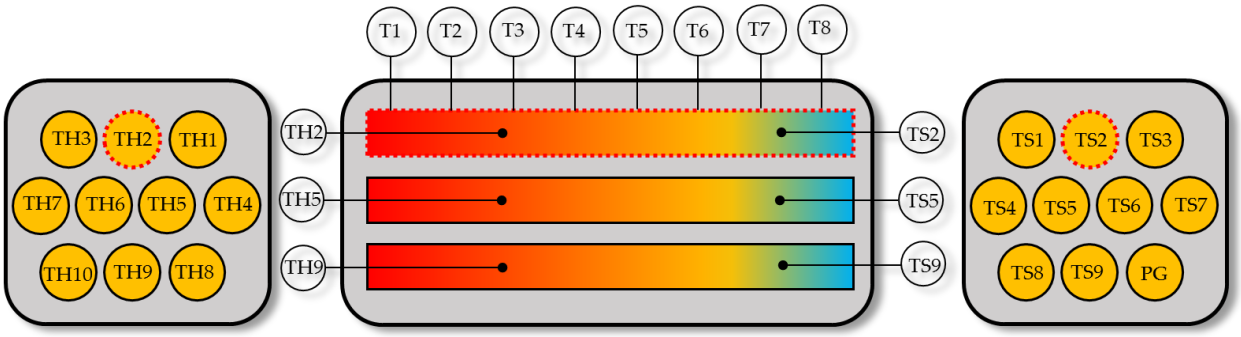

Source: UCLA, Wirz Research Group

Figure 31: Comparison of Numerical Results with Experimental Measurements for a Representative Charging Cycle

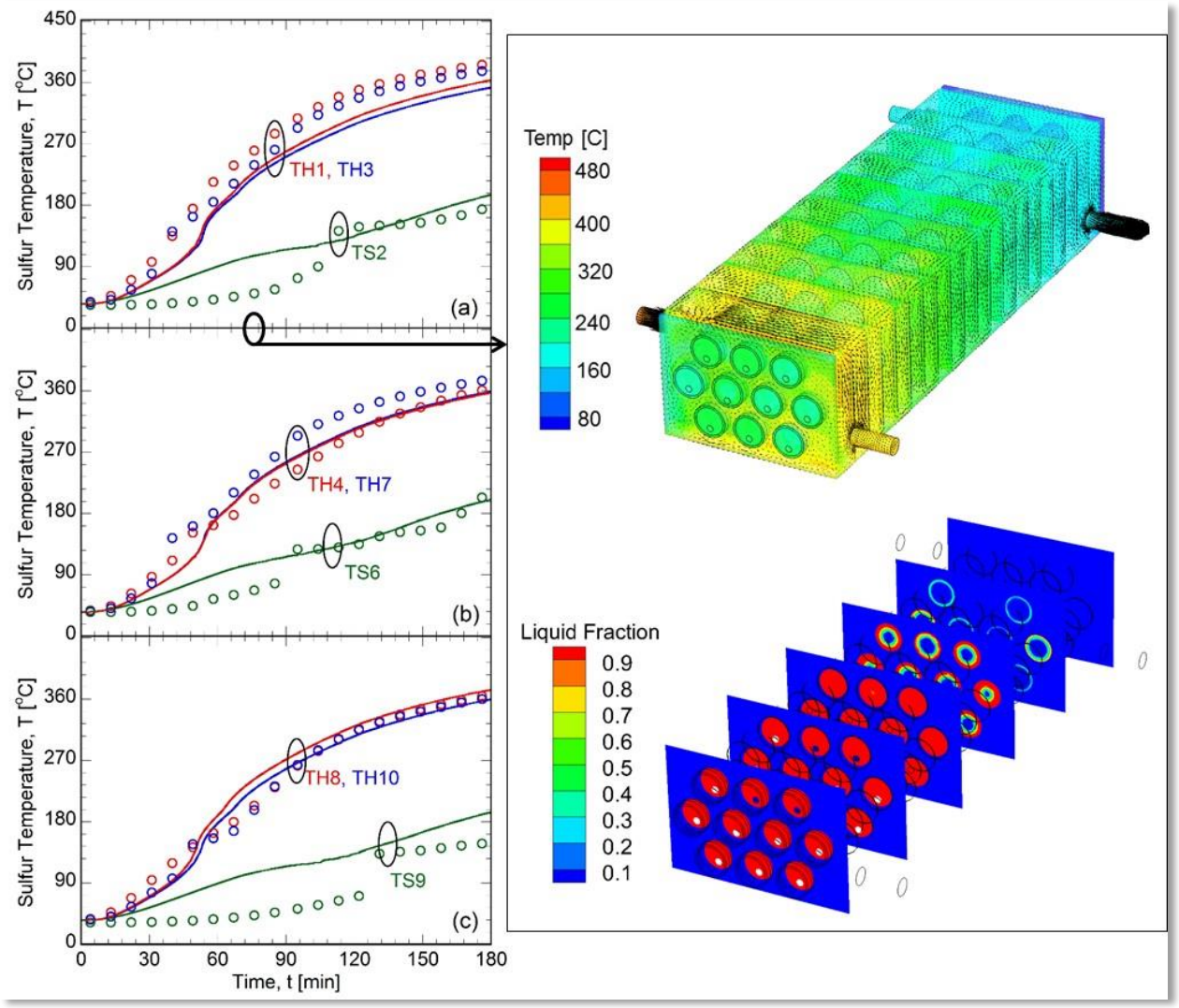

Source: UCLA, Wirz Research Group

Flow and Heat Transfer Analysis

Following the validation of the numerical model, the numerical results were used to illustrate the flow and temperature field within the thermal battery during charging. As seen in Figure 32, the flow field was highly impacted by the presence of baffles to ensure that the flow did not bypass the tube bank. In addition, the baffles turned the flow around, creating a tortuous HTF flow path that enhanced the heat transfer interaction between the HTF (air) and storage tubes.

Figure 32: Velocity Contour for Heat Transfer Fluid (Air) Flow

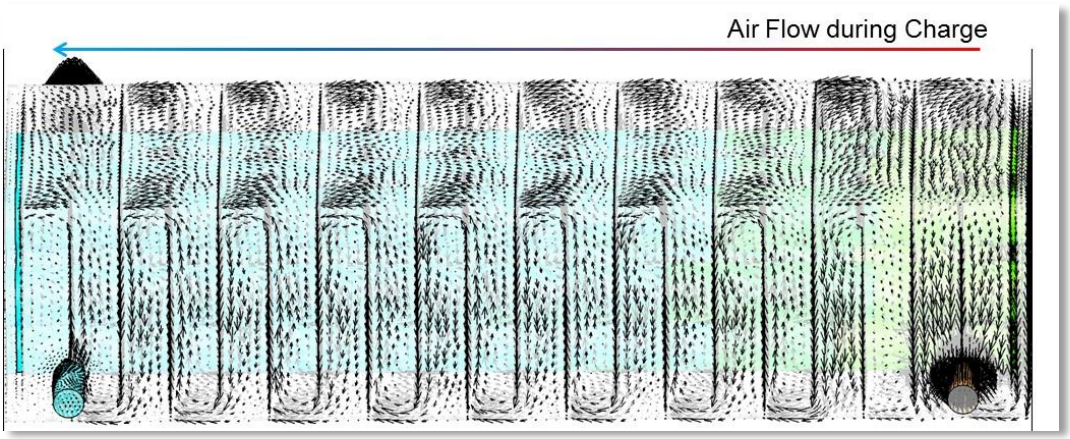

Source: UCLA, Wirz Research Group

Figure 33: Temperature Distribution with the Thermal Battery at Various Times During Thermal Discharge

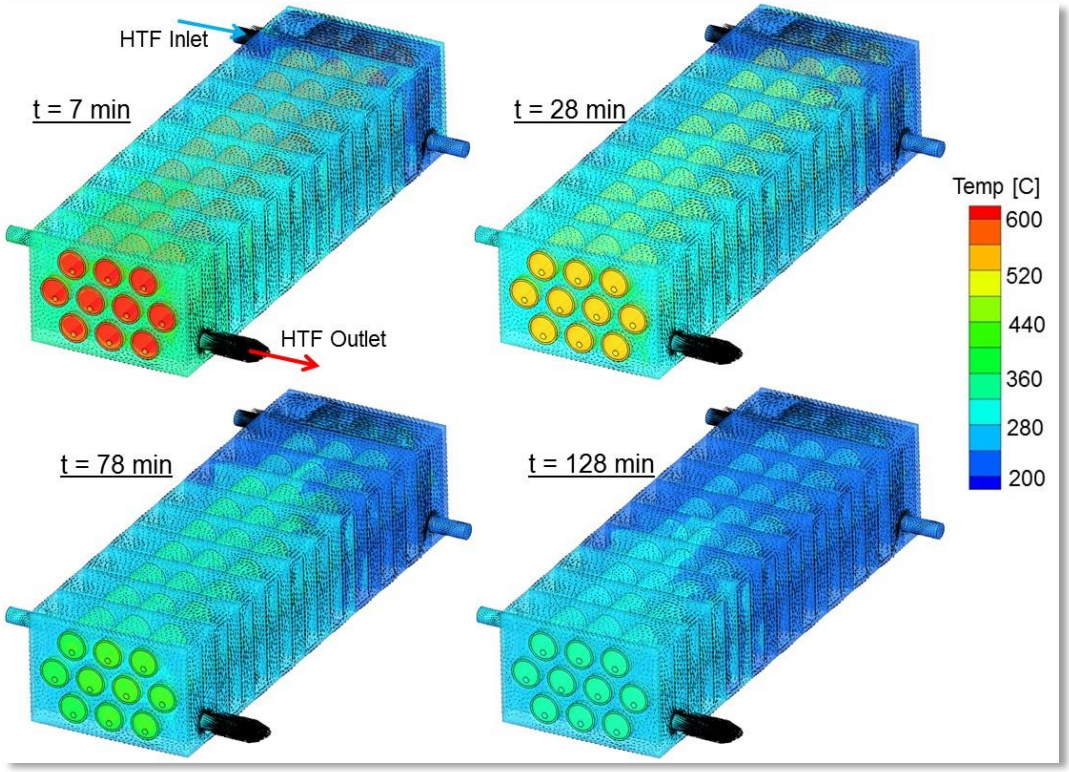

HTF Mass Flow Rate of 0.05 Kg/S and Operating Between 200°C and 600°C.

Source: UCLA, Wirz Research Group

Figure 34: Temperature Distribution with the Thermal Battery at Various Times During Thermal Charge

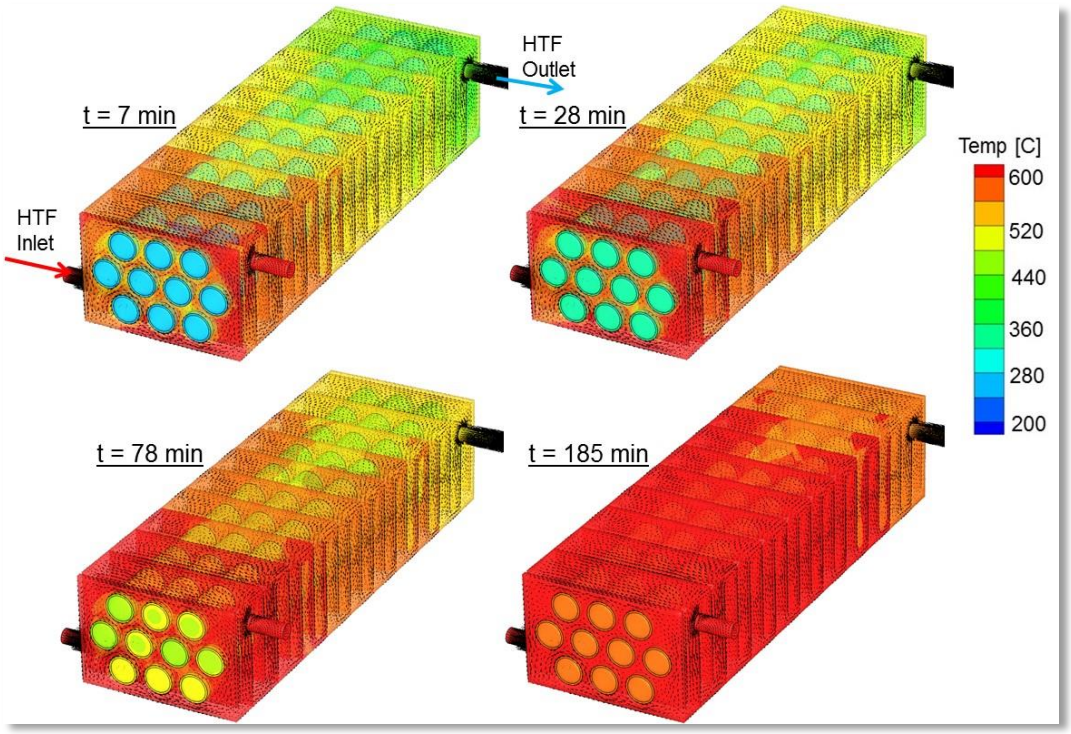

HTF Mass Flow Rate of 0.025 Kg/S and Operating Between 200°C and 600°C.

Source: UCLA, Wirz Research Group

Figure 33 and Figure 34 present the temperature distribution within the thermal battery during the thermal charge and discharge process at various time intervals. An axial temperature gradient inside the storage tubes are shown as a result of heat exchange between the HTF and sulfur from the inlet toward the exit of the thermal battery. The results from the validated numerical model showed that thermal energy was effectively transferred between the HTF and sulfur. To elucidate this further, a plot of volumetric average temperature of sulfur within one of the tubes and the corresponding tube wall was plotted in Figure 35. The study observed that that a negligible temperature difference exists between tube wall and sulfur highlighting the high charge and discharge rate exhibited by sulfur.

Figure 35: Temporal Variation of Volumetric Average Temperature of Sulfur and Tube Wall

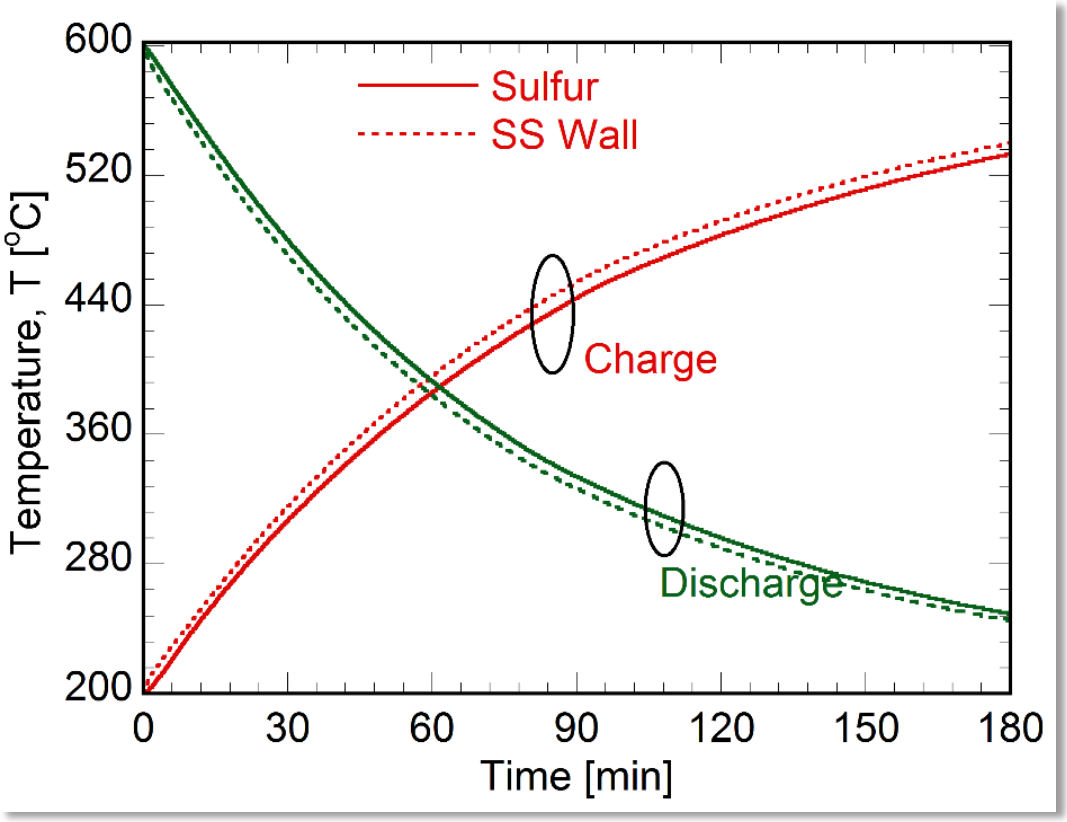

Source: UCLA, Wirz Research Group

Conclusion

The Wirz Research Group has successfully characterized the heat transfer mechanism inside sulfur for temperature ranges of 50˚C–600˚C. These results were directly applicable for thermal energy storage systems in CSP and CHP plants. The team developed strong understanding of the sulfur heat transfer behavior based on the excellent correlation between the computational and experimental efforts. Depending on the Rayleigh number (pipe diameter), the average Nusselt number obtained for discharge was three to 14 times higher than competing PCM and solid based thermal storage technologies, which were limited in their performance due to the inherent disadvantage of conduction-dominated heat transfer for all or most of their heat transfer during a given cycle. This study showed the utility of the models for providing critical insight into the sulfur heat transfer physics for making informed engineering choices. Also, the analysis tool developed as part of this effort predicted the heat transfer behavior of sulfur under real-time dynamic operating conditions of the TES system and has been used to design and characterize the SulfurTES battery effectively. Precise diagnosis of heat transfer behavior of sulfur lead to the invention of a novel segregated TES design concept. Overall, researchers found that the study's approach to sulfur thermal energy storage provided attractive charge/discharge performance for demand-responsive energy storage applications and did not require the expense and complexity of heat transfer enhancement techniques that must be employed by competing technologies.

CHAPTER 5:
Lab Demonstration

Introduction

The overarching goal of the *Lab Demonstration* task was to design, build, and test a laboratory scale 10kWh TES prototype using elemental sulfur as the storage fluid. The laboratory–scale, multi-tube TES system ("SulfurTES") was successfully designed and operated to demonstrate the viability of sulfur-based TES systems for a wide range of applications, including concentrated solar power (CSP) and combined heat and power (CHP) systems. The main objectives of this task were to: (1) design and fabricate a safe and reliable sulfur-TES system, (2) demonstrate the ability of sulfur-TES system to operate up to 600 ^{o}C for multiple charge-discharge cycles, and (3) store at least 10 kWh thermal energy during each cycle. The SulfurTES system design follows shell and tube heat exchanger concept, wherein sulfur is stored in 10 closed steel tubes and air is used as heat transfer fluid. The sulfur-filled tubes were equipped with cartridge heaters to operate the SulfurTES system in hybrid thermal charging mode. Performance of the system is analyzed based on the operating temperature, thermal energy storage capacity, volumetric energy density, and successful implementation of hybrid (e.g., thermal and electric) charging. The SulfurTES system was successfully operated up to 600 oC for multiple thermal cycles to store at least 10 kWh of thermal energy. Moreover, the system achieved a high volumetric energy density of 403 kWh/m3, which demonstrates the ability for compact system footprints for full-scale applications. The SulfurTES system was operated in hybrid thermal mode which indicates its ability to integrate with multiple energy sources such as thermal (e.g., concentrated solar power CSP, solar thermal, hybrid solar, fossil, industrial, geothermal, waste heat) and electrical energy (for example, off-peak electricity surplus, solar PV, wind).

Experimental Facility

The experimental set-up was comprised of a SulfurTES battery integrated with an air-based HTF loop for thermal cycling. The configuration and function of the HTF loop and SulfurTES battery are described in this section.

Heat Transfer Fluid Loop

Figure 36 and Figure 37 show a schematic and pictures of the air loop setup for thermal cycling of the SulfurTES battery. A high pressure (80 psig) air compressor coupled with a pressure regulator supplied the air at the required flow rate and pressure. A coalescing air filter was installed to remove the oil and oil mist down to 0.2 ppm, and particles larger than 5 µm to ensure dry and clean air for thermal cycling experiments. A flowmeter coupled with pressure gauge was installed to measure the mass flow rate of air entering the system.

Figure 36: Schematic of the SulfurTES Battery and Open-Loop Charge/discharge Heat Transfer Fluid (Air) System

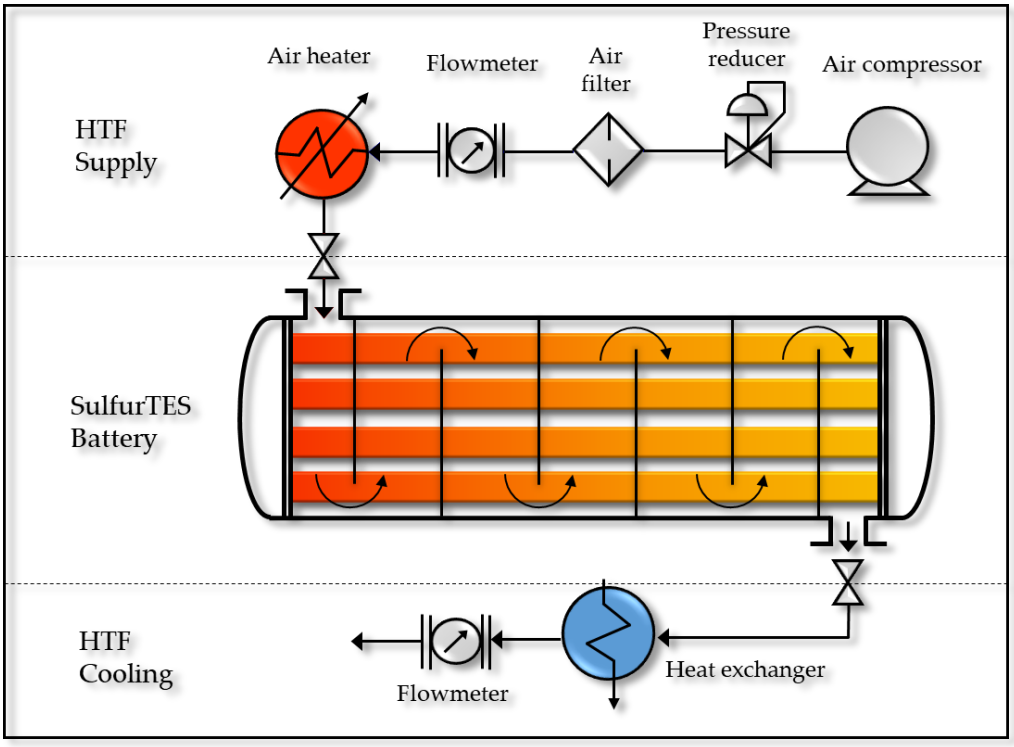

Source: UCLA, Wirz Research Group

A 10-kW air heater was installed at the inlet of the SulfurTES battery to heat the air up to 650°C for flow rates up to 35 standard cubic feet per minute (SCFM). A plate heat exchanger was installed at the SulfurTES battery outlet to cool the hot air before releasing to the ambient. The path of air flowing through SulfurTES battery was reversed when the operation was switched from charging to discharging mode, as discussed earlier.

Figure 37. SulfurTES Battery and Open-Loop Charge/Discharge Heat Transfer Fluid (Air) System

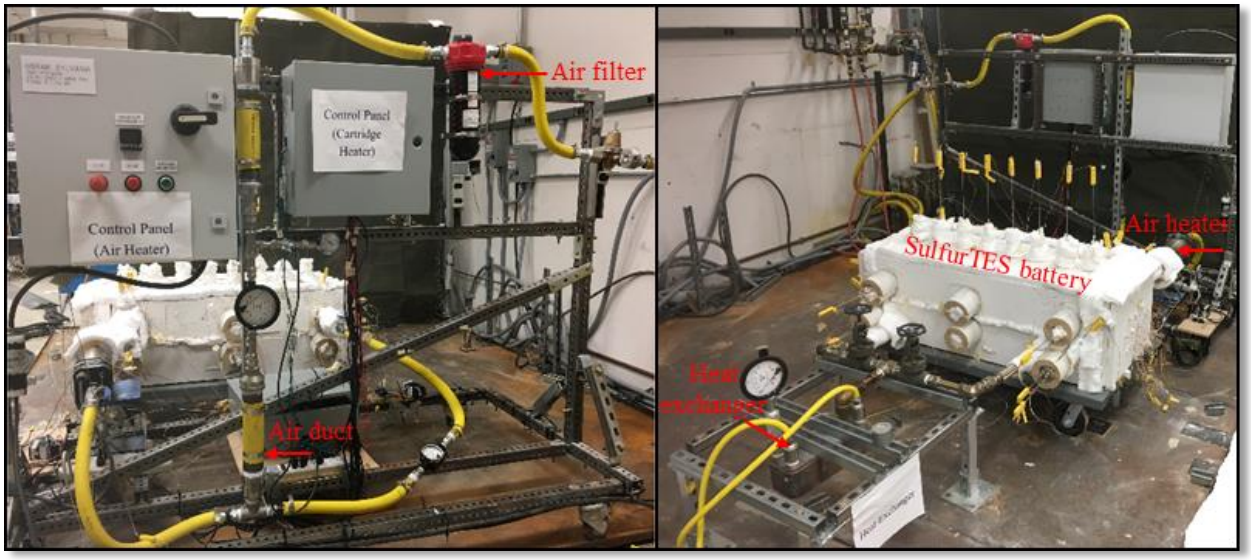

Source: UCLA, Wirz Research Group

SulfurTES Battery

The SulfurTES battery design was based on a shell and tube heat exchanger concept. It was fabricated using SS316 to enable its operation at a maximum operating temperature (600°C) and pressure (200 psig). SS316 is a cost-effective, high-strength alloy suitable for high-temperature (~650°C) thermal applications. A comprehensive material compatibility analysis showed that SS316 offered corrosion resistance to sulfur at high operating temperatures for a long period of operation. These features make SS316 a suitable material for the SulfurTES battery. Figure 38 shows the salient features of the SulfurTES battery.

Figure 38: Salient Features of a Sulfur TES Battery

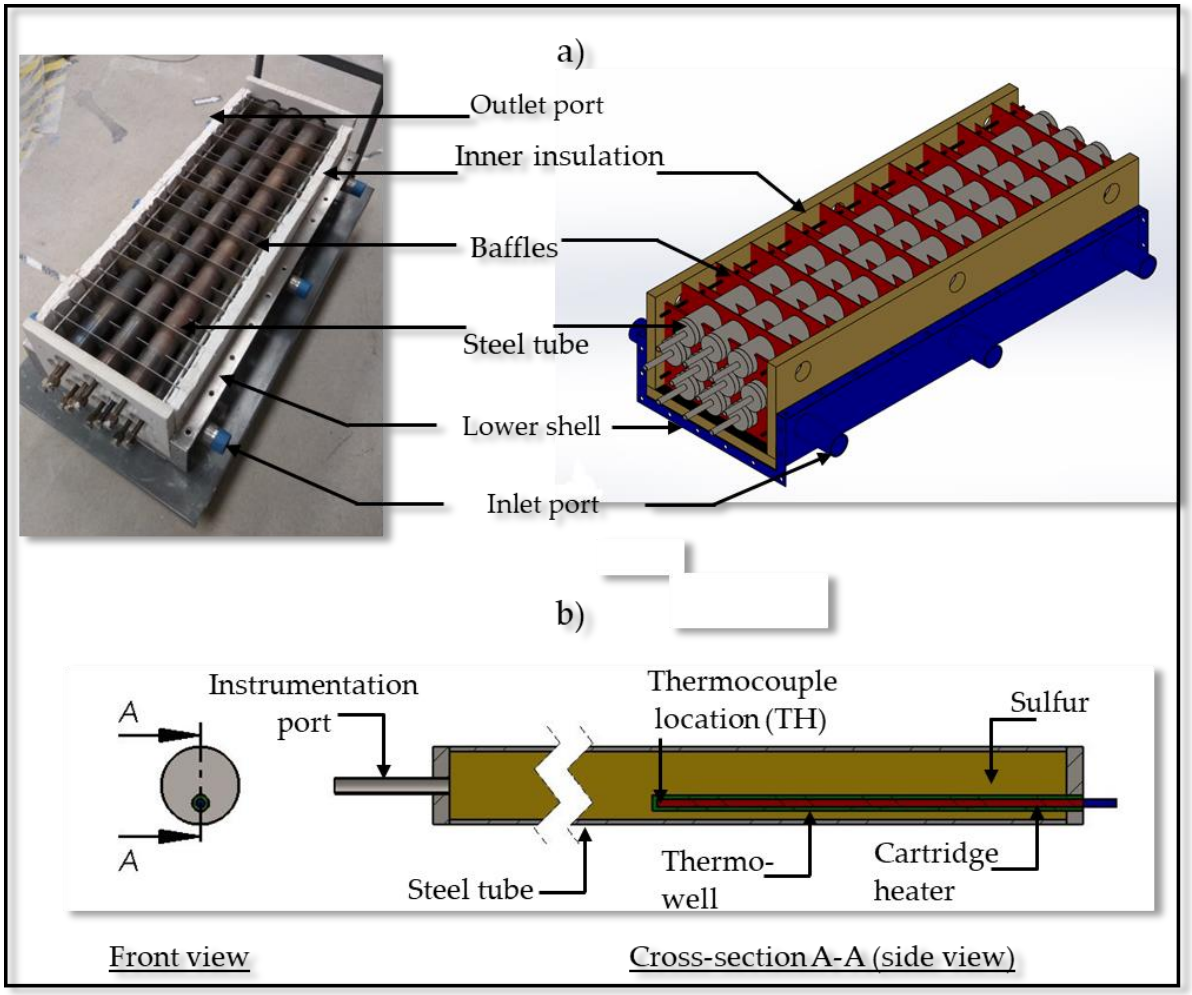

a) Schematic of the SulfurTES Battery, b) Salient Features of the Steel Tube

Source: UCLA, Wirz Research Group

A rectangular shell, 41"×14.5"×11" in size, enclosed 10 stainless steel tubes that were arranged in a triangular (30°) manner as per Tubular Exchanger Manufacturers Association (TEMA) standards [58]. The steel tubes were 2" NPS, Sch. 40 in diameter, 1 m in length, and sealed by 0.5"-thick caps at either end. Individual steel tube contained 3.2 kg of sulfur, thus total sulfur content in SulfurTES battery amounting to 32 kg. Each steel tube was equipped with a 3"-long instrumentation port and a 13"-long thermo-well. The instrumentation port was used to fill a steel tube with sulfur, and then a K-type thermocouple was installed through this

port to measure the sulfur temperature during thermal cycling. The thermo-well housed a cartridge heater (120V, 200W) that served as a secondary source of heat and allowed the SulfurTES battery to operate in a hybrid thermal charging mode. The cartridge heater was located below the axis to improve heat transfer to the sulfur [45].

The SulfurTES battery had 21 baffles; two end baffles (0.25" thick) that support the steel tubes, and 19 central baffles (0.0625" thick) that support the tubes and provide a tortuous path to the air to improve heat transfer.

The shell was equipped with eight access ports for thermocouples to measure the tube temperature along its length. In addition, 12 SS316 pipes were welded to the shell body that serve as inlet/outlet ports for the heat transfer fluid. There was one inlet and one outlet port for each charging and discharging process. Additional ports were provided in the midspan region to provide redundancy as well as flexibility (such as attachment of additional air heater) of the SulfurTES battery; however, these were not used for the test. The shell was closed by end plates, bolted to the flanges with a high-temperature gasket interstitially placed between them. The SulfurTES battery was insulated with high-temperature (~1,000°C) ceramic insulation to minimize the heat loss and ensure safe operation.

Instrumentation System

The instrumentation system was mainly comprised of K-type thermocouples, installed throughout the SulfurTES battery to measure temperatures of different components, including sulfur, steel tubes, shell, and insulation. Thermocouples were connected to the data acquisition system (DAQ) combined with LabVIEW to record temperature measurements. As shown in Figure 39, "tube thermocouples," T1 to T8, were installed to record the axial temperature gradient along the length of a steel tube.

Figure 39: Position of Thermocouples Within SulfurTES Battery for Measurement of Sulfur and Steel Tube Temperatures

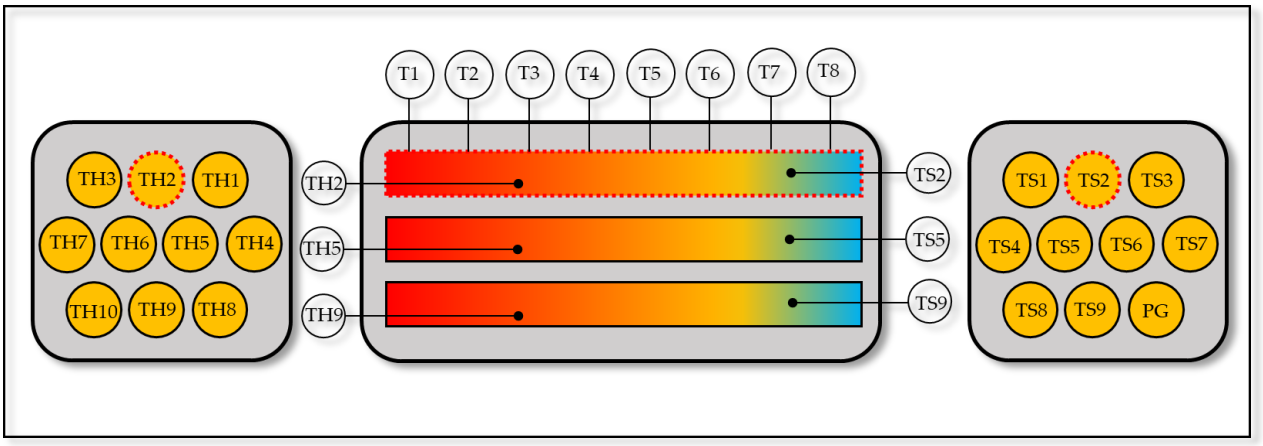

Thermocouples T1-T8 are installed on Tube 2 along its upper surface.

Source: UCLA, Wirz Research Group

In addition, these temperatures were used to estimate the thermal energy stored in steel tubes (stainless-steel mass). Sulfur temperatures were recorded using 19 'sulfur thermocouples'; TS1 to TS9 were in direct contact with sulfur, while TH1 through TH10 were integrated with the cartridge heaters embedded in steel tubes. Researchers acknowledged that the thermocouples TH1 through TH10 were not in a direct contact with sulfur (see Figure 38b), and a finite temperature difference between cartridge heater temperature (TH) and corresponding sulfur temperature may exist. The cartridge heater thermocouple (TH) and the location of interest for sulfur temperature were very close to each other and separated by a highly conductive, thin thermowell wall. Due to this fact, researchers assumed that the cartridge heater temperature (TH) represented the sulfur temperature at a tip of the thermowell. An industrially established practice was to use a thermowell-thermocouple assembly for temperature measurement of hot fluids, and a similar approach was adopted here. These sulfur temperatures were used to monitor the heat transfer behavior and thermal performance.

Experimental Procedure

This section discusses the thermal charge/discharge procedure for the SulfurTES battery. This procedure was used for multiple thermal cycles to investigate the thermal performance of the SulfurTES battery. In addition, a sulfur filling process is briefly discussed.

Sulfur Filling Process

The steel tubes were filled with molten sulfur using the sulfur filling device (SFD) to ensure safe and fast operation. In the beginning, 3.2 kg of sulfur powder was loaded in the SFD and the system was heated to melt the sulfur powder. Then, under gravity, the molten sulfur was transferred into the steel tube via the access port to fill 80 percent of the tube volume. This operation was conducted under an inert atmosphere to avoid generation of unwanted gases that would increase the system pressure.

Thermal Cycling of the SulfurTES Battery

The performance of SulfurTES battery was analyzed for multiple thermal cycles. At the beginning of thermal charging, a steady flow of air was set along the required flow path as shown in Figure 40. A supply of cooling water to the heat exchanger was used to ensure effective cooling of hot air exiting the SulfurTES battery. The air heater was used to provide high temperature (650^{o}C) air to the SulfurTES battery, which serves as a primary source of thermal energy. The thermal charging using hot air alone continued until the sulfur temperature, as recorded by TH1 through TH10 reached 350^{o}C. As this temperature was increased beyond 350^{o}C, cartridge heaters were activated and the SulfurTES battery was switched to a hybrid thermal charging mode. The thermal energy stored in the system was tracked in real time using the temperature measurements of thermal masses (sulfur and stainless steel) recorded in the LabView. The goal of the thermal charging process was to store greater than 5 kWh of the thermal energy, and thermal charging was continued until this goal was achieved. Then, the air heater and the cartridge heaters were switched off to terminate the thermal charging process. At the end of thermal charging, an axial thermal gradient developed along the SulfurTES battery, as indicated in Figure 40. After charging, cold air was supplied to the SulfurTES battery to start the thermal discharging process as shown in Figure 40. The path of HTF was reversed during discharge to reduce the local temperature

difference between the HTF and tube wall to improve exergetic efficiency and to ensure the HTF exits the SulfurTES battery at a higher temperature to improve energetic efficiency. The thermal discharging was continued until the average temperature of the SulfurTES battery was reduced to 200°C.

Figure 40: Heat Transfer Fluid Path During Thermal Charging and Discharging

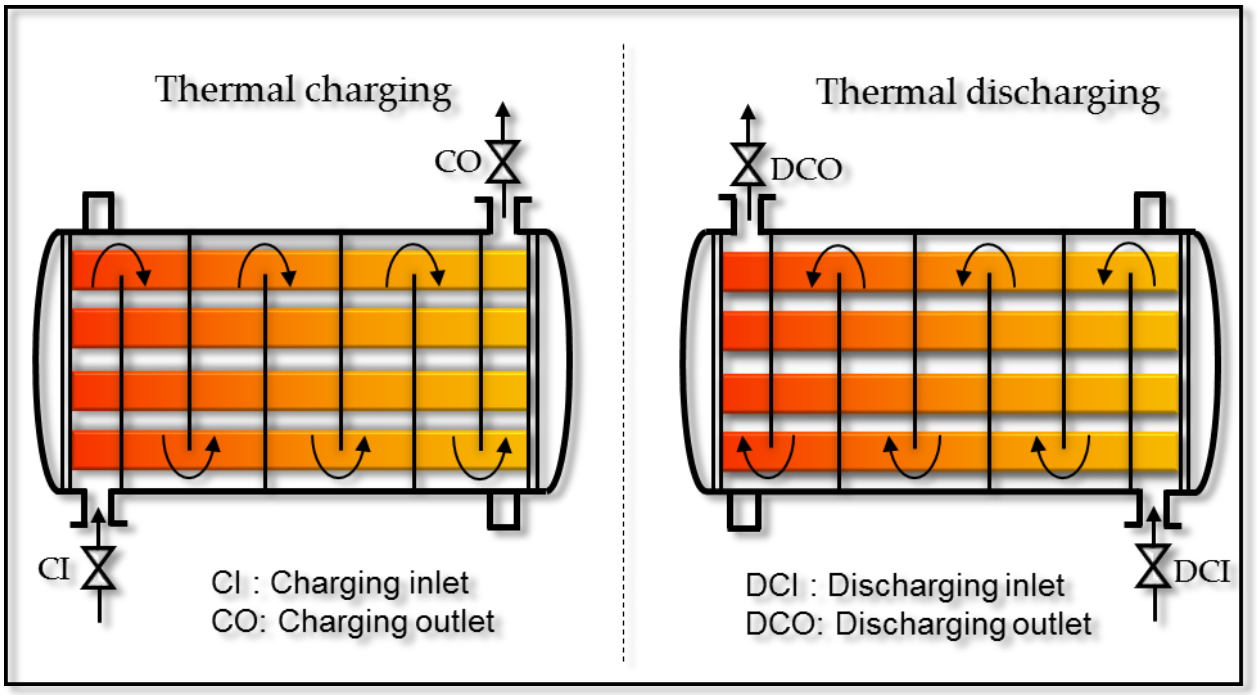

Source: UCLA, Wirz Research Group

Results and Discussion

Performance of the SulfurTES system was analyzed for multiple thermal charge/discharge cycles based on key parameters including operating temperature, thermal energy storage capacity, and volumetric energy density. The temperature of different components of SulfurTES was recorded using thermocouples and these measurements were used to calculate the energy stored in these components. Moreover, the temperature distribution in the SulfurTES provides physical insight into the heat transfer performance of the system.

Thermal Map of SulfurTES System

Figure 41a shows the inlet temperature of the SulfurTES for multiple thermal cycles. The SulfurTES operated up to 600°C, with peak inlet temperatures in the range of 575°C to 620°C. Multiple locations within the system were thermally charged to ~570°C. Figure 41b-d show the temperature of sulfur and steel tube for a representative cycle. Figure 41b shows the temperature of steel tube during charge/discharge cycle as recorded by thermocouples T1 through T8. The tube temperature ranged from 567°C to 480°C, with an average temperature of 513°C. Figure 41c-d show temperature distribution within sulfur. Each steel tube was equipped with two thermocouples. TH1 through TH10 were installed in a high-temperature region of the sulfur tube while thermocouples TS1 through TS9 were installed in a relatively cold section. Researchers observed that temperatures recorded by TH1 through TH10 were in the

range of 565°C to 570°C, while the sulfur temperature in a relatively colder region, recorded by TS1 through TS9, were in the range of 500°C to 510°C.

Figure 41: Thermal Map Within SulfurTES System During Thermal Charge/discharge Cycles

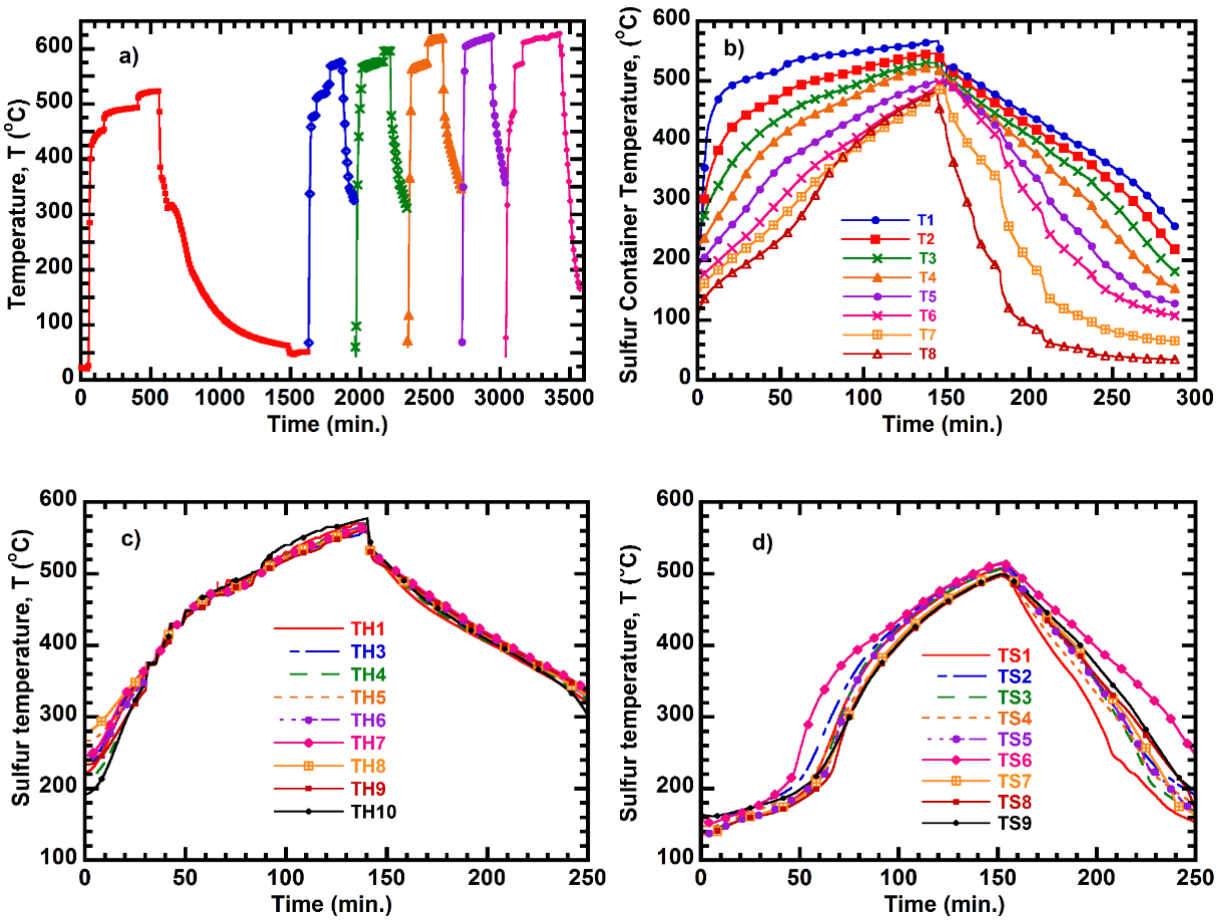

Source: UCLA, Wirz Research Group

Storage Capacity of SulfurTES System

Figure 42 shows the thermal energy stored within SulfurTES over the multiple thermal cycles. The thermal energy was primarily stored in sulfur and steel tubes. The study showed that the thermal energy stored in the SulfurTES was higher than 10 kWh, thus meeting the Energy Commission's goal of 10 kWh. The contribution of sulfur in total stored energy was ~43 percent. Based on the volume of thermal storage components, a significantly high volumetric energy density up to 403 kWh/m^3 was achieved that can lead to a compact footprint of industrial TES systems.

It is important to note that steel tubes were overdesigned to ensure safety for these tests. For this test, the project used schedule 2" NPS Sch. 40 SS316 tubes, which provided a factor of safety over five. Due to the relatively low vapor pressures of sulfur, as demonstrated in previous tests, researchers determined that schedule 2" NPS Sch. 10 SS316 tubes can be used, thereby greatly increasing the contribution of the sulfur storage energy to ~62 percent

of total energy stored. In addition, for larger diameter pipes such as 6-inch NPS, the contribution of sulfur in total energy stored can be as high as 81 percent.

Figure 42: Thermal Energy Stored in SulfurTES for Multiple Thermal Charge/Discharge Cycles

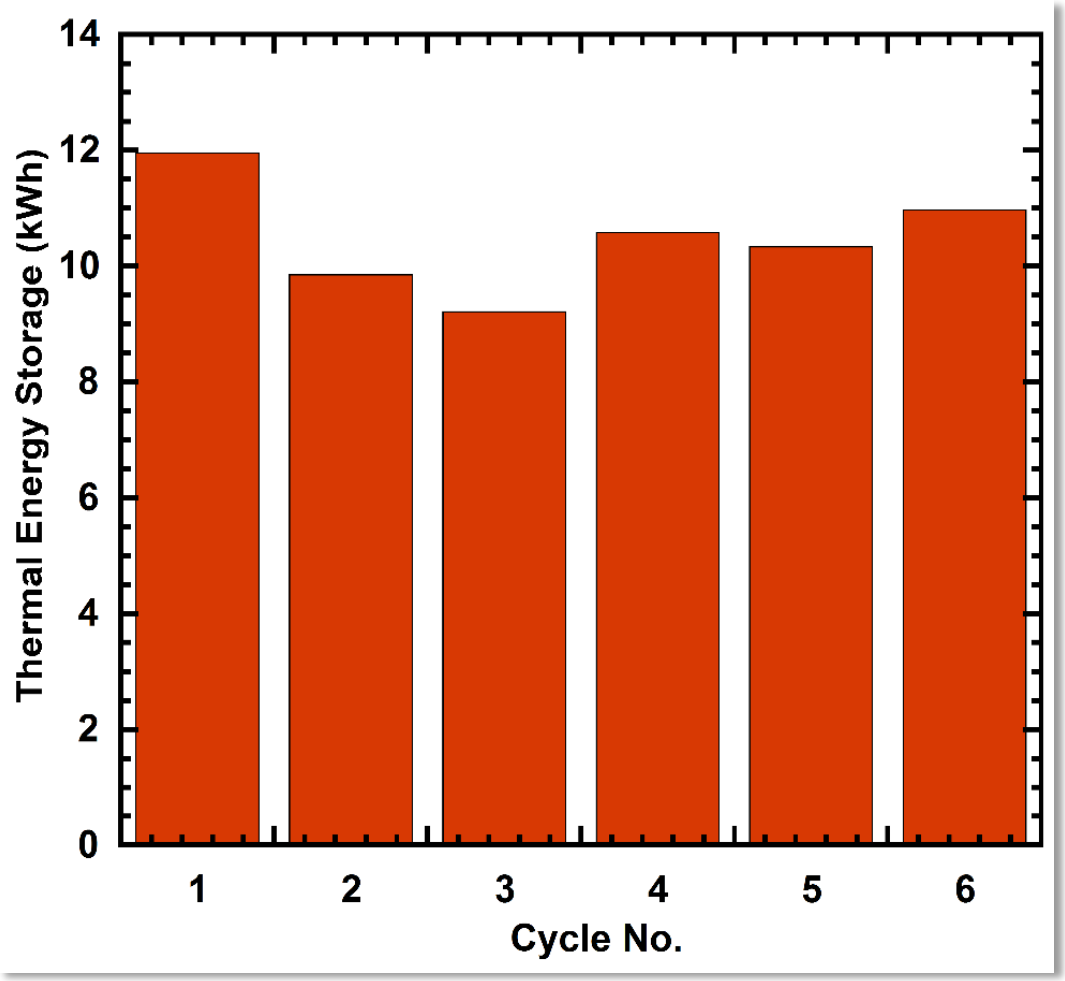

Source: UCLA, Wirz Research Group

Thermal Front Propagation

Figure 43 shows the thermal front propagation through the SulfurTES system during thermal charging. A thermal gradient was set in the SulfurTES at the end of thermal charging. This gradient represented the segregation of thermal energy in the system. Observations indicated that the temperature of the section of the SulfurTES near the inlet was quickly raised to ~500°C and then it gradually reached ~570°C, while the rest of the SulfurTES battery was charged via the propagating thermal front. During discharging, the flow of HTF was reversed as discussed earlier ithe thermal Cycling of the SulfurTES Battery section. Thus, HTF exiting the SulfurTES thermally interacted with the high-temperature zone of the SulfurTES system for a significant period of thermal discharging, leading to higher HTF exit temperature. As shown in Figure 44, the HTF exit temperature was raised and maintained at temperatures higher than 350°C for approximately two hours of thermal discharging. However, HTF exited at lower temperatures compared to SulfurTES system temperature. This was attributed to inherent limitation of air as a heat transfer fluid due to its thermo-physical properties.

Figure 43: Thermal Front Propagation Through SulfurTES System During Thermal Cycle

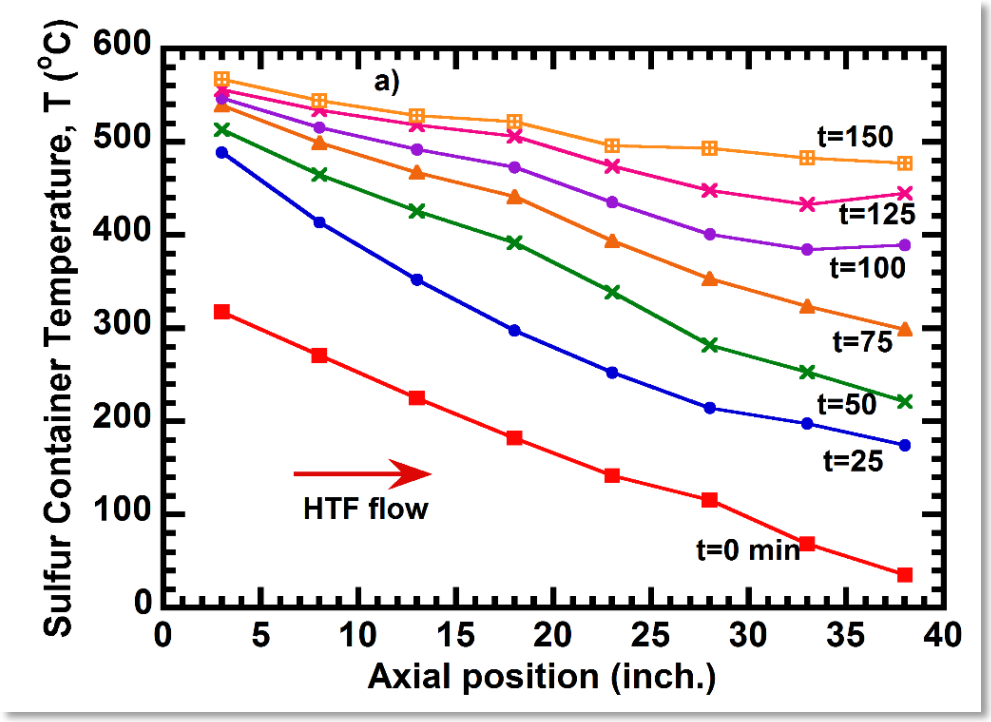

Source: UCLA, Wirz Research Group

Figure 44: Temperature of Heat Transfer Fluid Exiting the SulfurTES During Thermal Discharging

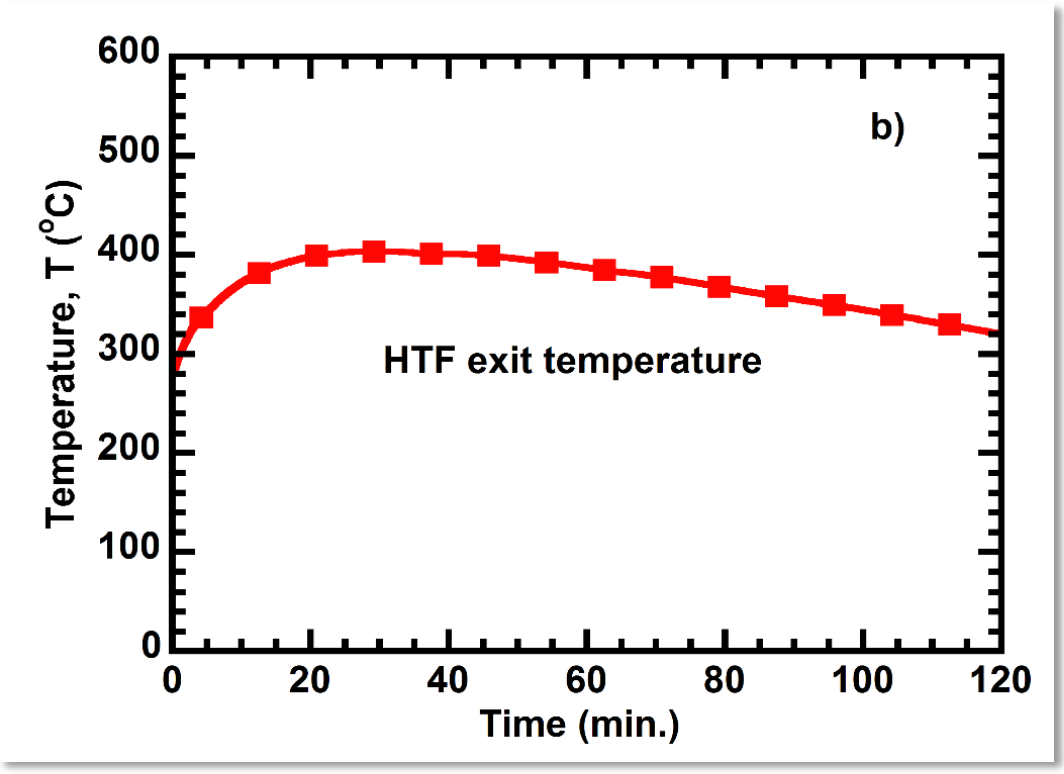

Source: UCLA, Wirz Research Group

Hybrid Thermal Charging

As mentioned previously, the SulfurTES was operated in hybrid mode in which the system was charged using high temperature heat transfer fluid as well as with cartridge heaters installed in steel tubes. The strategic location of the cartridge heater allowed for effective storage of surplus electricity available during low power demand period.

The cartridge heaters were equipped with an integrated thermocouple. Since the thermocouple was in close proximity to sulfur within the tube, researchers assumed that the cartridge heater temperature represented the sulfur temperature at that location. As the sulfur temperature reached 350°C, the cartridge heaters were activated as a secondary source of heat along with the high-temperature HTF. Figure 45a shows evolution of sulfur temperature before and after activation of the cartridge heaters. The system was charged with the high-temperature HTF until the temperature reached 350°C. Then the cartridge heaters were activated, and the system was switched to the hybrid charging mode. The effect of hybrid charging was observed in the rate of temperature rise beyond 350°C. Figure 45b shows an evolution of the sulfur temperature (TH) and steel tube temperatures (T1-T4) for a representative cycle. The study showed that within a few minutes of cartridge heater activation, the container temperatures increased at a higher ramp rate. This indicated that the effect of the cartridge heater was not localized but distributed throughout the steel tube. Thus, hybrid thermal charging facilitated SulfurTES to achieve a higher rate of thermal charging, which can be extremely important for the many target applications of this system.

Figure 45: Hybrid Thermal Charging of SulfurTES System Using High Temperature Heat Transfer Fluid and Cartridge Heaters

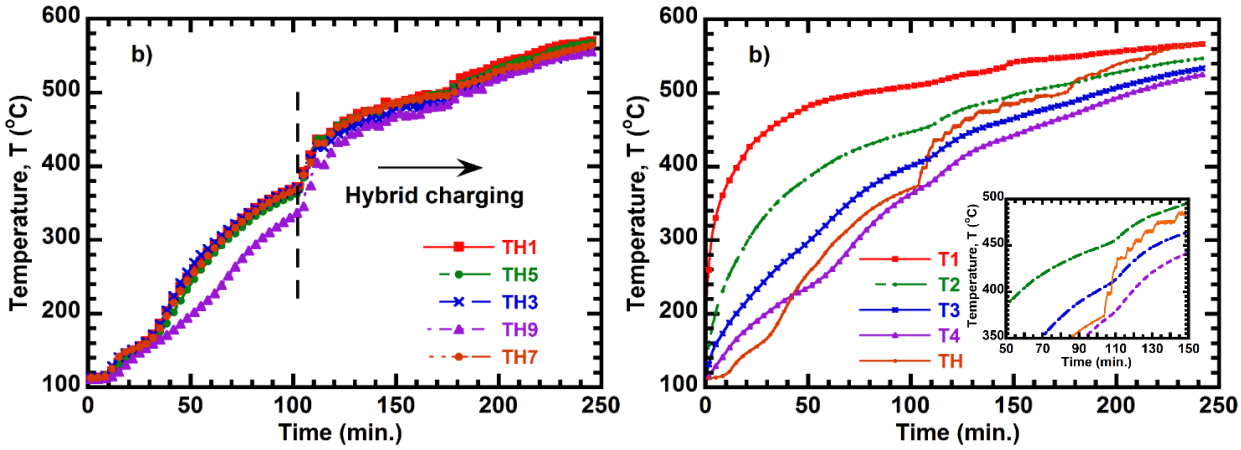

Source: UCLA, Wirz Research Group

Conclusion

The Wirz Research Group has successfully demonstrated the technical viability of a sulfur-based TES system as an energy storage technology for high temperature CSP and CHP applications. The multitube SulfurTES was designed and fabricated using well-established standards to ensure safe and reliable operation for multiple thermal cycles. The SulfurTES system was thermally charged to over 600°C to store thermal energy of 10 kWh or higher. In addition, a volumetric energy density up to 403 kWh/m^3 was achieved to demonstrate the

compact footprint of the TES system. The MacroTES system was successfully operated in the hybrid charging mode wherein electrical heaters served as a secondary heat source along with HTF. This showed the ability of the MacroTES system to integrate with various energy sources, including thermal (such as CSP, solar thermal, hybrid solar, fossil, industrial, geothermal, and waste heat) and electrical energy (such as off-peak electricity surplus, solar PV, and wind). This study has established the essential framework for the future design of the pilot-scale TES system that is to be demonstrated with a concentrated solar thermal facility at the conclusion of this project.

CHAPTER 6:
Pilot Demonstration

Introduction

The central goal of the Pilot Demonstration task was to design, build, and test a pilot scale SulfurTES battery integrated with CSP-dish system to store 30 kWh of thermal energy. The main objectives of this task were: (1) successful scaling of SulfurTES battery from laboratory-scale to pilot-scale testing, (2) successful integration of the SulfurTES battery with CSP-dish system for on-sun demonstration, and (3) storage of at least 30kWh thermal energy. The SulfurTES system design followed the shell and tube heat exchanger concept, where sulfur was stored in 10 closed steel tubes and air was used as heat transfer fluid. Performance of the system was analyzed based on the thermal energy storage capacity, receiver air outlet temperature, and thermal map of SulfurTES battery. The SulfurTES system was successfully operated up to 600oC to store greater than 30 kWh of thermal energy. This demonstration showed an effective integration between the CSP system and the SulfurTES battery to capture solar energy and store as heat that can be used for many industrial and commercial applications. The thermal performance of the SulfurTES battery will be used for system-level analysis of the utility-scale sulfur-based thermal energy storage systems.

Experimental Facility

In this section, details of the key system components, including SulfurTES battery, solar receiver, and HTF conduit are discussed in detail.

SulfurTES Battery

Design

Figure 46 shows the assembly of the SulfurTES battery with critical system components. The design of SulfurTES battery was based on the shell and tube heat exchanger, wherein sulfur-filled steel tubes were enclosed in a rectangular shell, and heat transfer fluid was passed over these tubes during thermal charge/discharge cycle. The SulfurTES battery was comprised of 12 4-inch NPS Sch. 40 SS316 tubes to achieve the thermal storage capacity of 30 kWh. Moreover, 12 transverse baffles were installed to provide a tortuous path to the heat transfer fluid for superior heat transfer. In addition, three longitudinal baffles were provided to ensure thermal segregation within SulfurTES battery during thermal charge/discharge process to achieve high exergetic efficiency of the system. The tube-baffle assembly was safely enclosed in a rectangular shell that was designed to provide the required path to the heat transfer fluid, and to accommodate instrumentation including thermocouple feedthroughs. In addition, 12 pipes were welded to the shell that will serve as inlet/outlet ports during thermal cycling. The shell was equipped with two thermocouple feedthroughs that provide access to 24 K-type thermocouples. The SulfurTES battery will be insulated with microporous insulation (thermal conductivity, k=0.03W/m-K) to minimize the heat loss and ensure safety of the personnel. Figure 46 shows the key components and assembly of the SulfurTES battery.

Figure 46: Schematic of the Critical Components and Assembly of the SulfurTES Battery

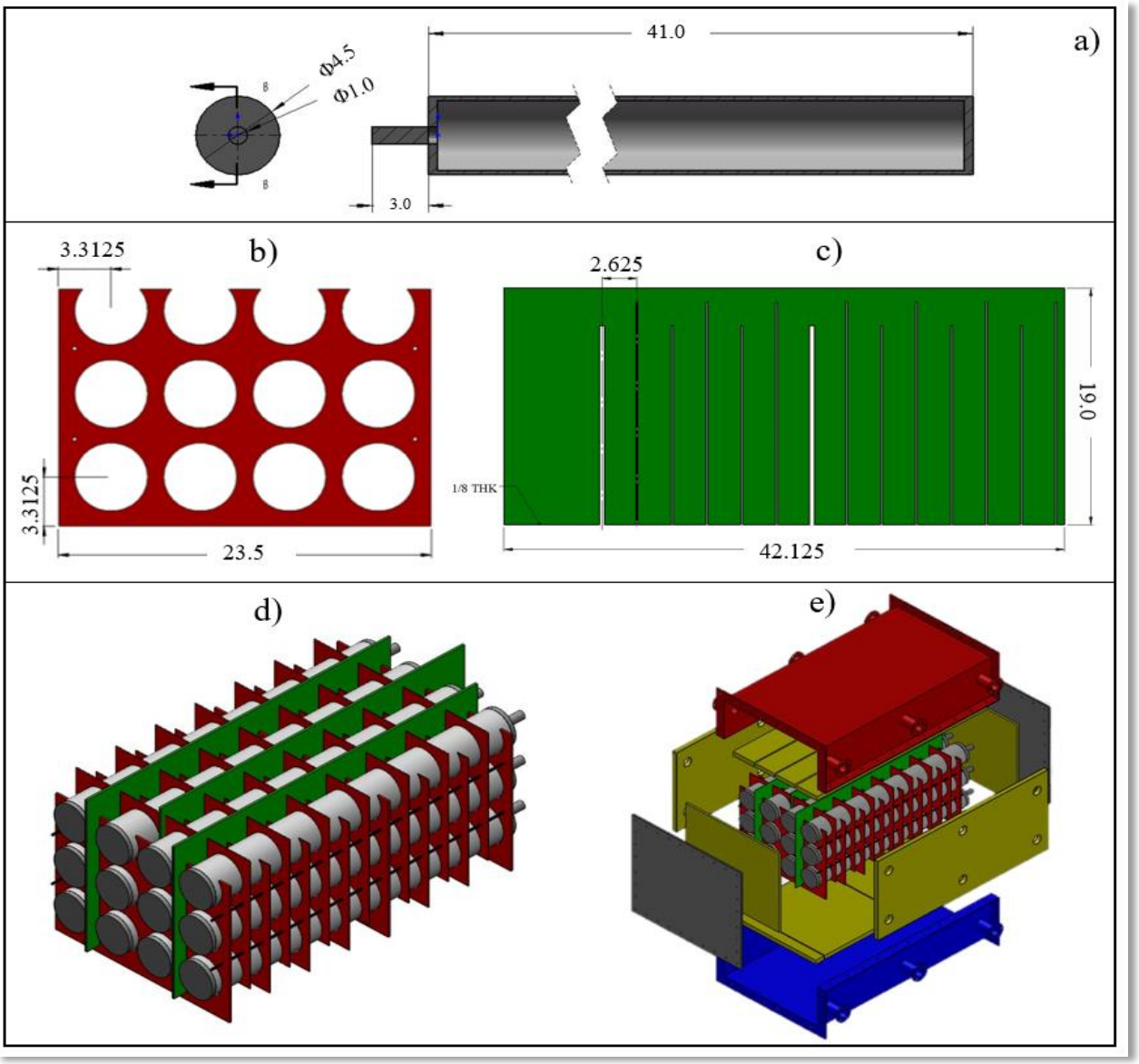

(a) SS316 Tube, (b) Transverse Baffle, (c) Longitudinal Baffle, (d) Tube-Baffle Assembly, (e) SulfurTES Assembly

Source: UCLA, Wirz Research Group

Fabrication and Assembly

The research team at UCLA worked with a manufacturing company, Safna, to fabricate the 30 kWh SulfurTES battery according to the design specifications. Figure 47 shows the process for the assembly of SulfurTES battery. The team used a heavy-duty platform truck as a base for the thermal battery for ease of transportation. Initially, a two-inch layer of microporous insulation was placed on the platform along with four high-strength ceramic blocks to support the battery. Then, a lower half of the shell was positioned on the ceramic blocks so that the microporous insulation did not have to bear the weight of the shell. Next, two high-temperature thermocouple feedthroughs were installed at each central inlet/outlet port of the shell. Each feedthrough provided 12 K-type thermocouples to be used to measure tube

temperatures as well as air inlet/outlet temperatures. A one-inch layer of inner insulation was installed on the inner surface (side and bottom) of the shell, followed by the installation of the assembly of transverse and longitudinal baffles.

At this point, the assembly established a support system for the installation of 12 sulfur-filled SS316 tubes. Each steel tube weighed ~30 kg, and thus required careful maneuvering during their installation. The team started installing the bottom-most tubes to ensure the stability of the tube-baffle assembly. Each tube was equipped with up to three K-type thermocouples depending on the tube position. Researchers used a spot-welding machine to securely attach each thermocouple at its designated positions. Then, a layer of one-inch insulation was installed on the top and at both ends of the tube-baffle assembly, followed by the installation of the upper half of the shell. Next, end plates were installed to close the shell. A high-temperature gasket was interstitially placed between two halves of shell as well as shell end plates and then bolted together to seal the system. The active inlet/outlet ports were connected to the required equipment, including the air heater, cold air inlet, and heat exchanger. The inactive inlet/outlet ports were closed using blank flanges. The SulfurTES battery was covered with a two-inch layer of outer insulation to prevent further heat loss and protection of lab personnel. After these steps were completed properly, the system was ready for the thermal charge/discharge cycles to store 30 kWh of energy.

Figure 47: Assembly of 30 kWh SulfurTES Battery

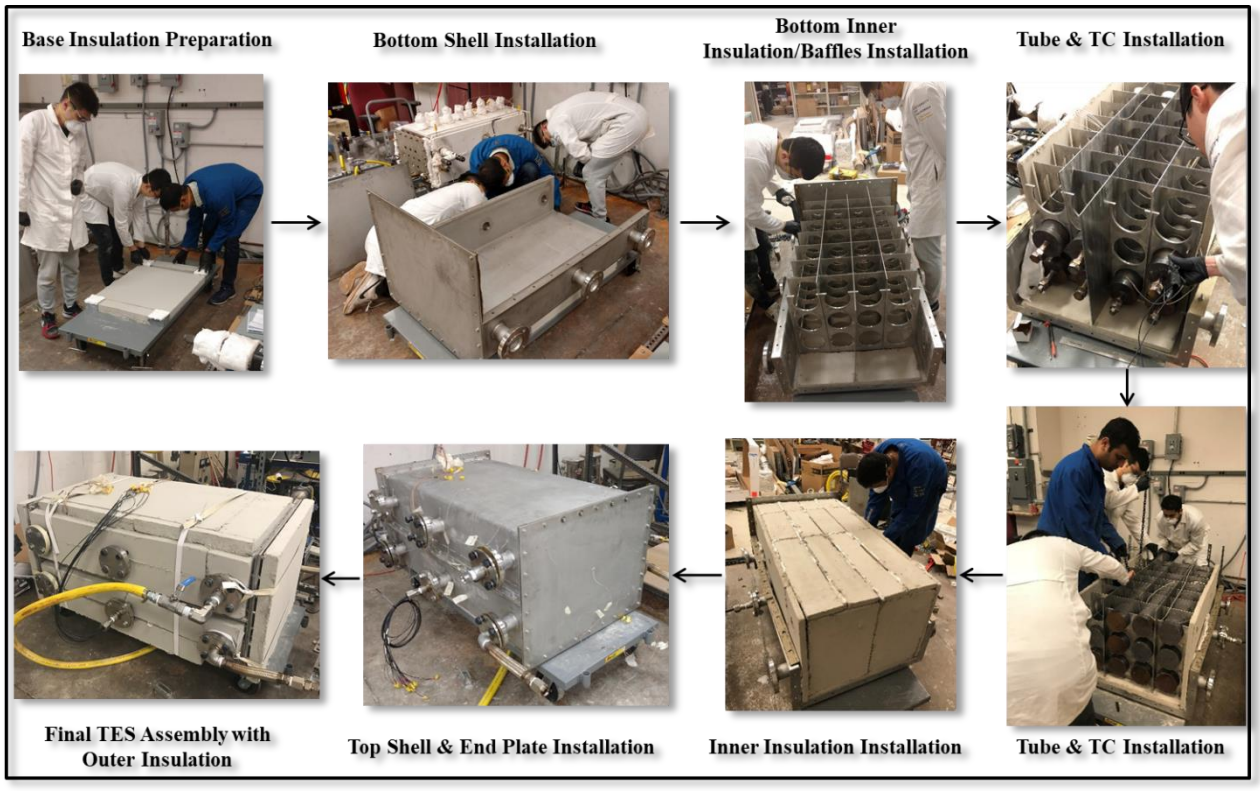

Source: UCLA, Wirz Research Group

Concentrating Solar Power-Dish System

Figure 48 shows the Helia CSP system developed by Thermal Storage System (TSS). The system was comprised of four parabolic mirrors that received solar radiation and concentrated

this solar energy at the focal point of the dish, so that the solar energy can be converted into thermal energy. The parabolic mirrors were installed on a frame that can rotate in horizontal and vertical planes, allowing the parabolic dish to track the sun. The CSP system was equipped with photosensors that detect the shift in the sun's position and provide the feedback signal to the control system. The control system adjusted the position of the dish using horizontal and vertical drives until the CSP-dish started pointing toward the sun to capture the maximum amount of solar radiation. This process continued throughout the day as the sun shifted its position from sunrise to sunset. At the end of the day, the CSP-dish was rotated back to the original position, making it ready for the next thermal cycle.

Figure 48: Key Components of the Helia Concentrating Solar Power System

(a) Parabolic Mirrors, (b) Concentration of Solar Energy at the Receiver, (c) Photosensor, (d) Vertical Drive, (e) Horizontal Drive

Source: UCLA, Wirz Research Group

Receiver

TSS developed the solar receiver to capture the solar energy as heat and transfer it to the heat transfer fluid (air) used to thermally charge the SulfurTES battery. Figure 49 shows the schematic of the solar receiver developed by TSS. The receiver was composed of five panels, assembled as five surfaces of a cuboid. The remaining sixth surface was comprised of an aperture to receive a concentrated solar power from the Helia system. Each panel was comprised of four SS316 serpentine tubes arranged in parallel, serving as the conduit for the

heat transfer fluid (air). These tubes were immersed in the liquid tin, which received the heat from the CSP dish at the front surface of the panel exposed to solar radiation, and then transferred that heat to the air flowing through the serpentine tubes. These tubes were connected to a common plenum that received high-temperature air from each panel and passed it to the air conduit connected to it. The air conduit transported this high-temperature air to the receiver for the thermal charging process.

Figure 49: Schematic and Picture of the Solar Receiver

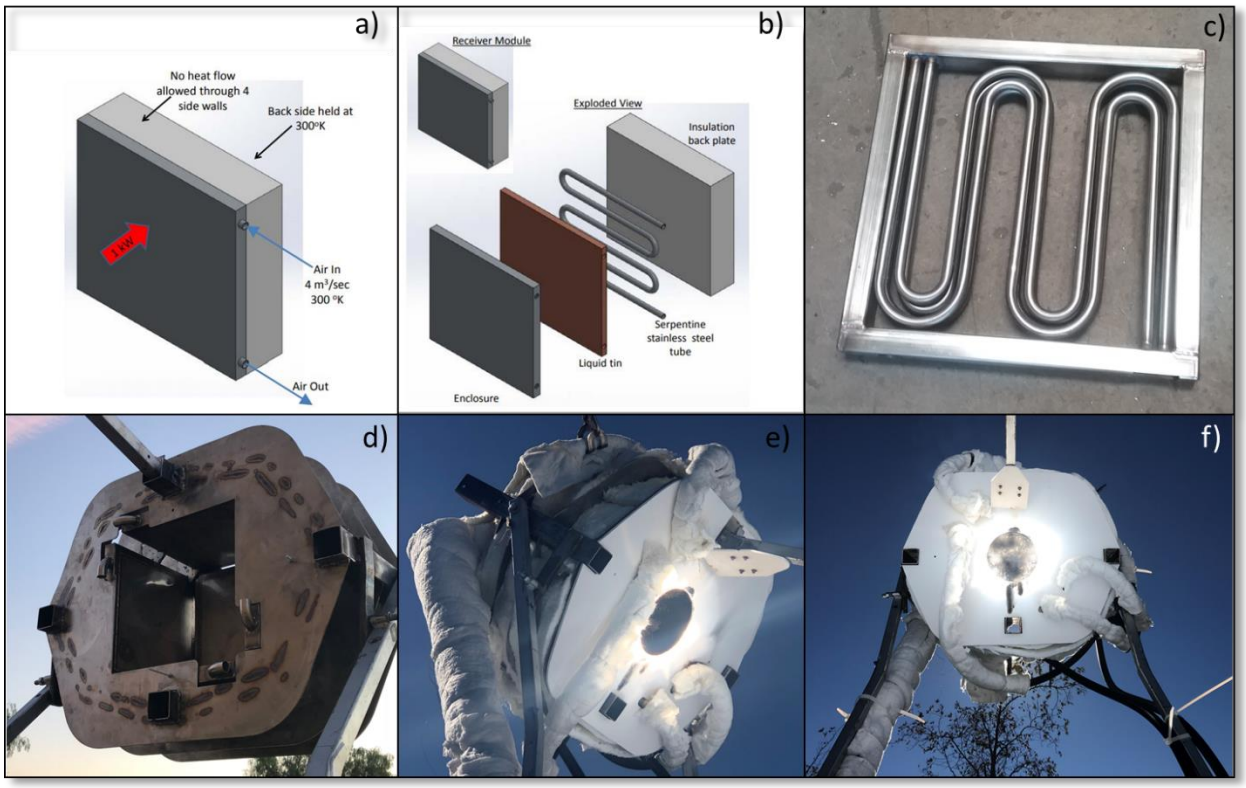

Source: UCLA, Wirz Research Group

Heat Transfer Fluid Conduit

To ensure a dependable supply of high-grade thermal energy from the TSS CSP solar receiver to UCLA's SulfurTES battery during thermal charge operation, the project developed a robust heat transfer fluid conduit. The team used experimental system and computational tools to determine the ability of the HTF conduit to retain the thermal energy of air flowing through it for many design parameters and operating conditions. Figure 50 shows the pictures of the HTF conduit, which at one end was connected to the receiver at the outlet of the plenum, while the end was connected to the charge inlet of the SulfurTES battery. The HTF conduit had two rigid sections connected by a flexible section that would allow the rotation of the CSP receiver while maintaining the secure connection to the stationary SulfurTES battery on the ground. The HTF conduit was comprised of the SS316 tube insulated with two layers of insulation: (1) flexible mineral wool insulation and, (2) rigid microporous insulation. This HTF conduit provided a safe and effective passage to the high-temperature air from the solar receiver to the SulfurTES battery during the on-sun demonstration.

Figure 50: Heat Transfer Fluid Conduit Connecting the Solar Receiver with SulfurTES Battery

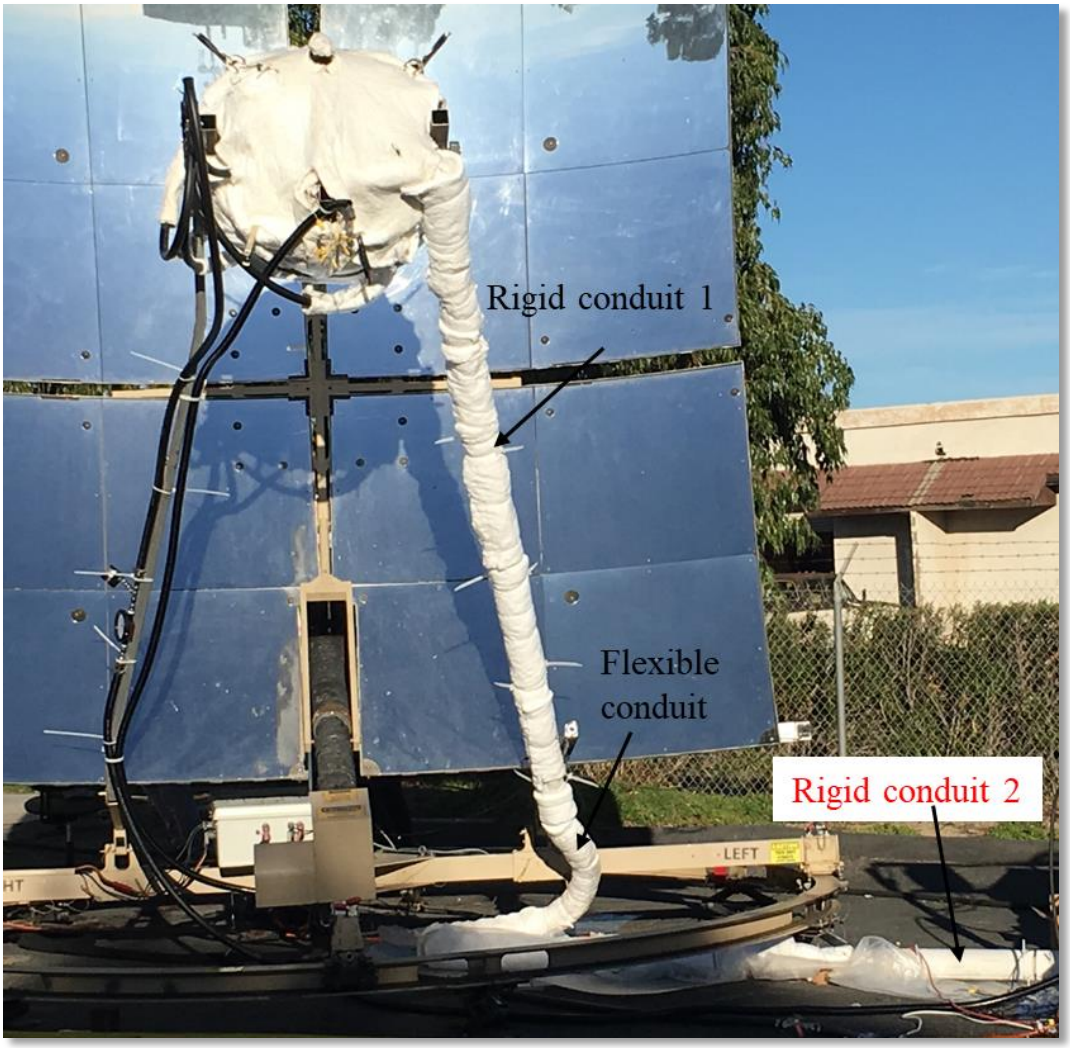

Source: UCLA, Wirz Research Group

Instrumentation

The CSP-TES system was equipped with instruments for the temperature, flow, and pressure measurement during the thermal cycling. A brief overview of the instrumentation system is provided in this section

Thermocouples

Thermocouples were necessary for the accurate calculation of the key performance parameters, including thermal storage capacity, and thermal charge/discharge rate. The SulfurTES battery was equipped with 24 K-type thermocouples, of which 20 were installed to measure the tube temperature, while four were installed to measure air inlet/outlet temperatures during thermal cycling. Figure 51 shows the position of tube thermocouples with SulfurTES battery. Longitudinal baffles divide the SulfurTES battery in four sections, with each section consisting of three tubes. One tube in each section was equipped with three thermocouples (shown with hatched cross section in Figure 51), while the rest of the tubes

had one thermocouple each. This arrangement allowed optimum use of available thermocouples to understand the thermal map of the SulfurTES battery during operation.

Figure 51: The Schematic Showing Position of Tube Thermocouples Within SulfurTES Battery

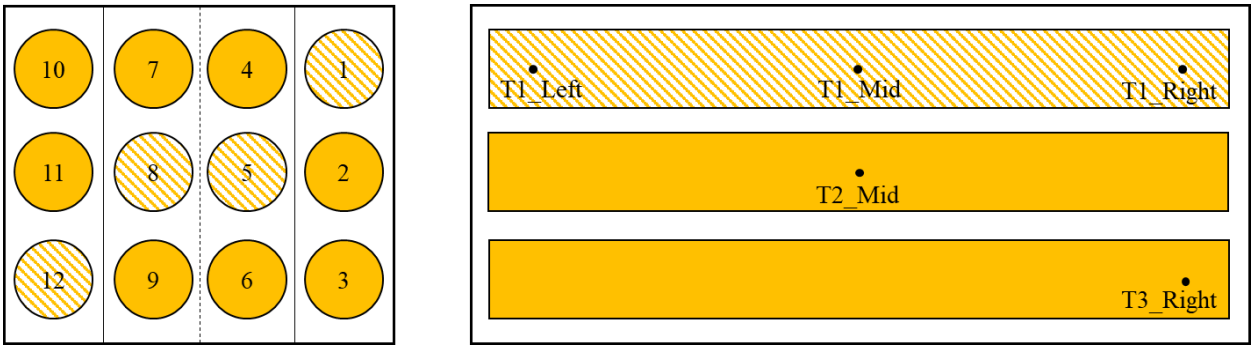

Source: UCLA, Wirz Research Group

Similarly, the team installed eight K-type thermocouples to measure the temperatures of the solar receiver at different locations, which would allow researchers to evaluate its performance. Of the five panels, the back panel was equipped with three thermocouples (BB, BC, BT), while left, right, and top panels were equipped with single thermocouple (LC, RC, TC). All these thermocouples were installed on the inner surface of the panels and were exposed to the concentrated solar radiation from the CSP dish. The team also installed one thermocouple on the outer surface of left panel (LO) to measure the temperature difference across the transverse cross section of the panel, and thus provided insight into the heat transfer performance within single panel. Finally, a thermocouple was installed at the outlet of the plenum to measure the temperature of the air exiting the receiver.

Flow Measurement

The accurate measurements of air flow conditions, namely, flow rate and pressure were required for the thermal analysis of the SulfurTES battery. As shown in Figure 53, researchers installed a flowmeter-pressure gauge assembly at the inlet of solar receiver as well as the air heater to measure the flow conditions of the air entering the system.

Figure 52: Flowmeter/Pressure Gauge Assembly at the Air Heater Inlet

Source: UCLA, Wirz Research Group

The critical components, including the SulfurTES battery, CSP-dish, solar receiver, HTF conduit, and instrumentation were carefully assembled to ensure the effective capture and conversion of solar energy into thermal energy, and the transport of this energy to the SulfurTES battery. Figure 53 shows the final assembly of the CSP-TES system, ready for the on-sun demonstration.

Figure 53: Final CSP-TES Assembly Used for the On-Sun Demonstration of the SulfurTES Technology

Source: UCLA, Wirz Research Group

Experimental Procedure

The solar receiver served as the primary source of thermal energy, while the air heater provided additional thermal energy to make up for the unavailability of sufficient solar energy in the winter. At the beginning of the thermal charging, a steady flow of air was established through the solar receiver as well as via the air heater. The team used a supply of cooling water to the heat exchanger to ensure effective cooling of hot air exiting the SulfurTES battery. Then, the tracking mechanism of the Helia CSP system was activated to ensure that the CSP dish always directed toward the sun during the charging process. The air passing through the receiver was heated to high-temperatures and transported to the SulfurTES battery using an air conduit. In parallel, the air heater provided additional thermal energy, thus enhancing the thermal charge rate of the SulfurTES system. The thermal charging continued until greater than30 kWh of thermal energy were stored in the thermal battery. Then, the tracking mechanism was used to position the CSP system directed toward the east, making it ready for the next cycle. Moreover, the air heater was switched off to terminate the additional supply of the thermal energy. After charging, cold air was supplied to the SulfurTES battery to start the thermal discharging process. The path of the HTF was reversed during discharge to reduce the local temperature difference between the HTF and the tube wall to improve exergetic efficiency and to ensure that the HTF exits the SulfurTES battery at a higher temperature to improve energetic efficiency. The thermal discharging was continued until the SulfurTES battery was cooled to safe temperatures (less than 150^{o}C).

Results and Discussion

In this section, the performance of CSP-TES system is discussed based on the thermal energy storage capacity, thermal map of solar receiver, and thermal map of SulfurTES battery.

Thermal Map of Solar Receiver

The thermal map of the solar receiver provided insight into the receiver's ability to absorb the concentrated solar energy and provide it to the HTF passing through it. The solar receiver was equipped with nine K-type thermocouples attached at different locations. The temperatures recorded by these thermocouples is shown in Figure 55a. The team observed that the back panel was heated to temperatures greater than 500^{o}C due to maximum exposure of its surface to the concentrated solar radiation. Other panels were heated to relatively lower temperatures (greater than 300^{o}C), due to partial exposure of their surface to solar radiation. Moreover, the average difference between the temperatures at inner and outer surface of the left panel was ~27^{o}C, indicating a high rate of heat transfer within the single panel of the receiver. Figure 55b shows the temperature of the air exiting the receiver, which peaked at 400^{o}C, indicating satisfactory performance of the solar receiver.

Figure 54: Temperature Distribution Within Solar Receivers

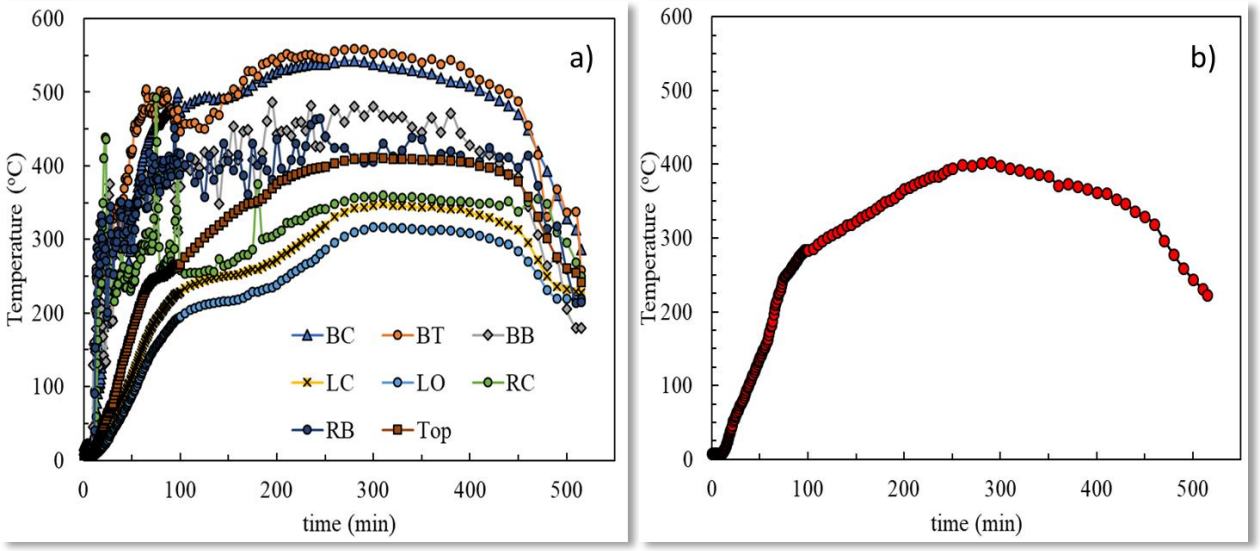

(a) Temperature Distribution within Solar Receiver During Thermal Charging, (b) Temperature of Air Exiting the Solar Receiver

Source: UCLA, Wirz Research Group

Thermal Map of SulfurTES Battery

The temperature distribution within a SulfurTES battery is an important parameter to understand the thermal performance of the system in the context of thermal storage capacity, heat transfer rate, exergetic, and energetic efficiency. Figure 56 shows the thermal map within the SulfurTES battery during thermal charging determined using the temperature measurements by tube thermocouples. Researchers observed that the SulfurTES battery successfully established a thermal gradient along its flow path established by the longitudinal baffles. At the end of thermal charging, sections one to four were successfully charged to temperature ranges of 500°C–400°C, 400°C–300°C, 300°C–200°C, and 200°C–100°C. This temperature distribution showed that the heat transfer fluid exited at a relatively low temperature during thermal charging leading to high exergetic and energetic efficiencies during thermal charging. Moreover, the SulfurTES battery can heat the heat transfer fluid to maximum possible temperature during thermal discharging, resulting in high discharge exergetic efficiency.

Figure 55: Tube Temperatures Within SulfurTES Battery During Thermal Charging

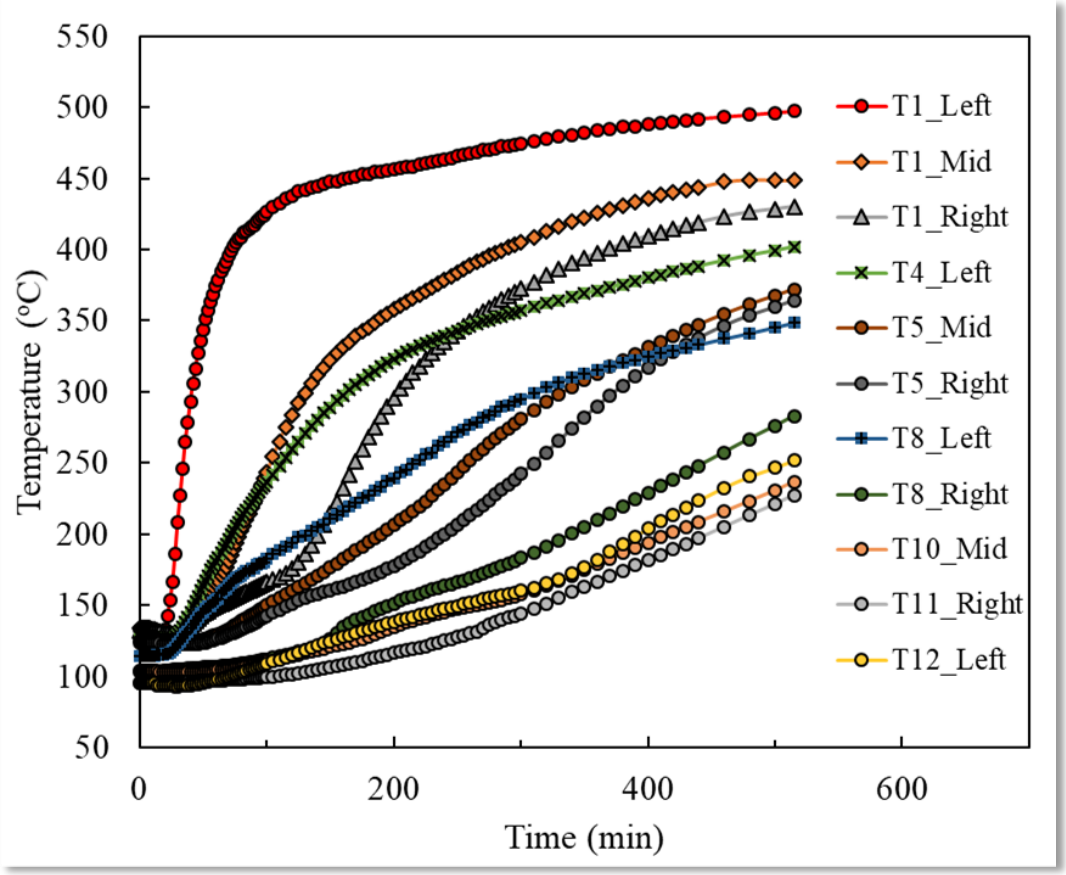

Source: UCLA, Wirz Research Group

Thermal Energy Storage

The sulfur and stainless tubes were major thermal storage components of the SulfurTES battery that predominantly store thermal energy via sensible heat storage mechanism. For thermal energy storage calculations, the average system temperature was calculated based on the tube temperatures, which was then used to compute the sensible energy storage with ambient temperature as a reference. In addition, the latent heat of liquification of sulfur was considered for the energy storage calculations. Figure 57 shows the plot of thermal energy stored during on-sun demonstration of the SulfurTES battery. The study observed that the SulfurTES battery stored greater than 30 kWh of thermal energy, thus meeting the Energy Commission's project goal.

Figure 56: Thermal Energy Stored in the SulfurTES Battery for Multiple Cycles

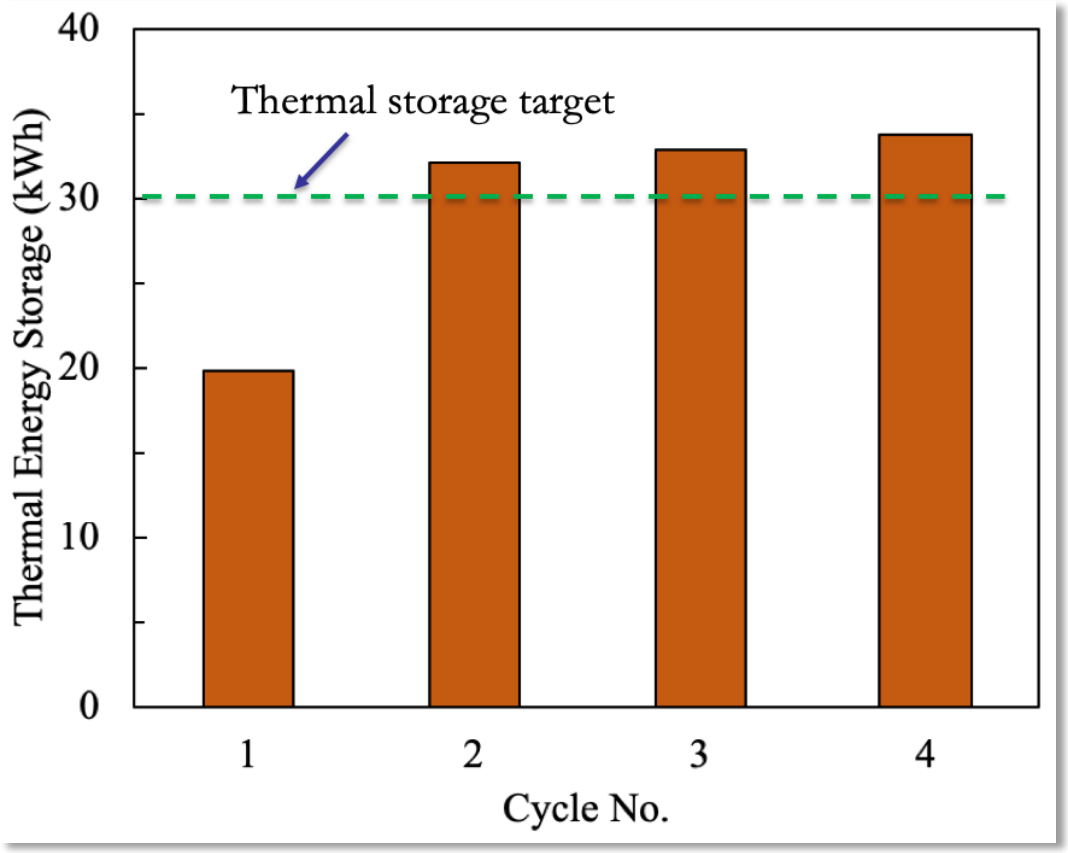

Source: UCLA, Wirz Research Group

Conclusion

The Energy Innovation Lab at UCLA, in collaboration with Thermal Storage Systems, has successfully demonstrated the pilot-scale SulfurTES battery integrated with the CSP-dish system to store greater than 30 kWh of thermal energy over multiple cycles. The key components of the system, including CSP system, solar receiver, heat transfer conduit, and the SulfurTES battery were designed and fabricated using industry standards, and provided safe and reliable performance during operation. The solar receiver integrated with the CSP-dish system effectively captured the concentrated solar energy to raise the heat transfer fluid temperature to greater than 400°C. The SulfurTES battery maintained significant thermal segregation along the heat transfer fluid path resulting in high exergetic and energetic efficiency during thermal cycling. This study provides a reliable framework for the development of a high-fidelity system cost model that will be used to design utility-scale SulfurTES systems.

CHAPTER 7:
System/Cost Analysis

Introduction

The objective of the system modeling was to develop an experimentally validated numerical model and to use it to investigate the performance and cost of industrial scaled SulfurTES systems. Energy conservation was applied to each component of the system including sulfur, tube, HTF, shell, and insulation, to form the numerical model as a set of coupled energy equations. Heat transfer coefficients are obtained from empirical correlations to avoid solving momentum equations and saving computational power and time. The model was validated by experimental results from lab-scale SulfurTES thermal battery and the on-site pilot demo, followed by a parametric study for a system with 1 megawatt-hour (MWh) storage capacity, where design and operating conditions are varied to observe their impact on system level performance. After gaining insight into dependency of system level performance on system geometry and operating conditions, a design strategy will be proposed with a detailed design procedure to help design a system that meets user-specified performance requirements. Finally, based on the system level performance, cost analysis will be conducted for differently designed systems with various storage capacities to demonstrate the low-cost characteristics of SulfurTES systems.

Model Development

System Description

A schematic of the system with its cross-sectional view is shown in Figure 58. Based on the concept of a shell-and-tube heat exchanger, the system in the thermal battery configuration has a bundle of sulfur-filled steel tubes that are enclosed by a circular shell with an HTF inlet/outlet placed on either end. The system geometry is specified by an inner shell diameter $D_{sh,i}$, a shell length L and a tube bundle arrangement. The tube bundle is supported by baffles separated by a baffle spacing, Bs, equals to $0.2D_{sh,i}$. Within the tube bundle, each tube has an outer and an inner diameter of d_o and d_i. The tube arrangement is in a 30° triangular layout, with a tube pitch ratio, Pr = $\frac{P_t}{d_o}$, and percent baffle cut, %Bc, determined based on TEMA standard [58] and recommendation from heat exchanger design handbook [59]. The entire outer surface of the system is covered by insulation.

Figure 57: Schematic of the SulfurTES

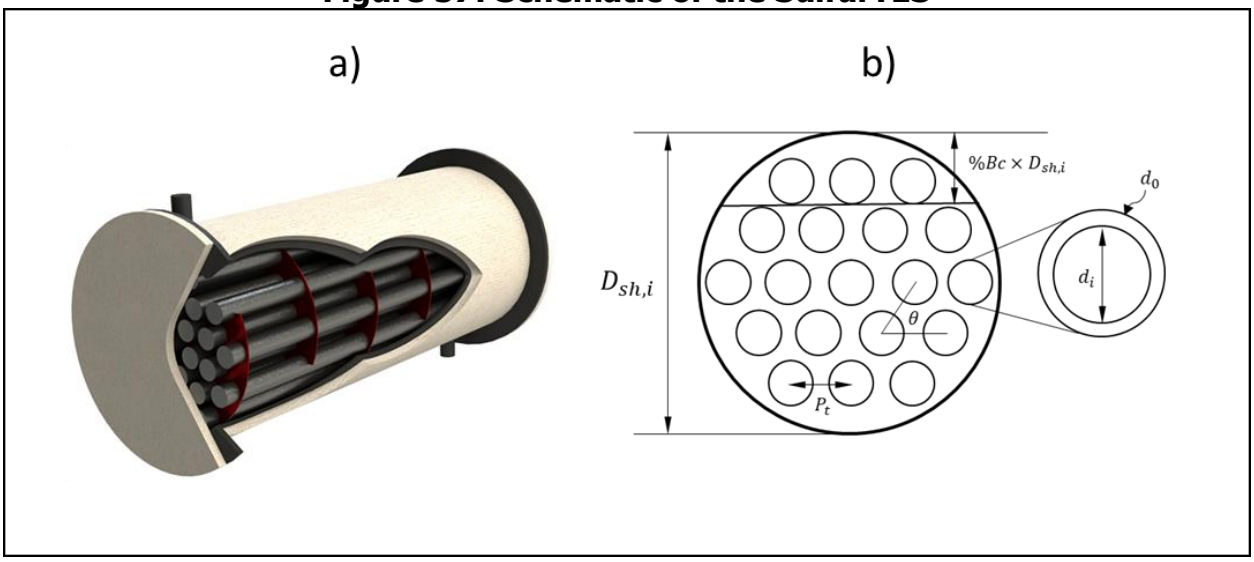

System schematic of (a) SulfurTES system, and (b) cross-sectional view of system.

Source: Heat Exchanger Design Handbook

During charging, hot HTF enters the system on one end, flowing axially along a tortuous path created by baffles, providing heat to the system and leaving the system on the other end. A schematic of flow path of charging is shown in Figure 58. During discharging, the flow path is reversed to have optimum rate of heat recovering. For the current study, the charge/discharge temperature T_C/T_D and HTF mass flow rate was set to be constant throughout thermal cycling.

Figure 58: Schematic of Heat Transfer Fluid Flow Path

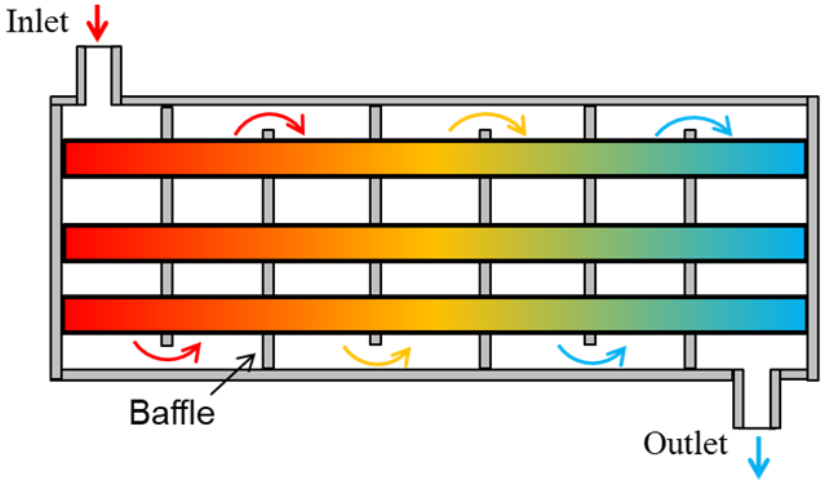

Source: UCLA, Wirz Research Group

Model Assumptions

In the current analysis, the HTF temperature was assumed to vary solely along the flow direction (axial direction). Temperatures of the shell and tube wall (SS316) are assumed to be radially invariant at any time instance while varying only in the axial direction. This assumption is valid due to its relatively low conductive resistance. Although temperature variation in sulfur is radially dependent due to natural convection, the ongoing analysis considers volume-

averaged sulfur temperature, and a volume-averaged sulfur heat transfer coefficient, h_s, is employed in Eq. (1). Due to the assumption of radial uniformity in HTF temperature, the vertically installed insulation will only have axial temperature gradient across its thickness. However, for horizontal insulation, both axial and radial temperature gradients coexist, due to axial temperature variation in HTF and large temperature differences between the system and ambient environment respectively.

Governing Equations

The performance of the system can be modeled based on energy transfer between each component, including sulfur, container tube, HTF, shell and insulation. Each component is discretized, and energy conservation is applied to each grid and solved to predict its transient temperature field during thermal cycling. Equations (1)-(6) denote to corresponding energy equations,

$$m_s C_{p,s}\left(\frac{\partial T_s}{\partial t}\right) = h_s A_s (T_s - T_t) + k_s A_s \frac{\partial T_s}{\partial z} \quad \text{— Sulfur} \tag{1}$$

$$m_t C_{p,f}\left(\frac{\partial T_t}{\partial t}\right) = h_f A_t \left(T_t - T_f\right) + h_s A_s (T_t - T_s) + k_t A_t \frac{\partial T_t}{\partial z} \quad \text{— Tube} \tag{2}$$

$$m_f C_{p,f}\left(\frac{\partial T_f}{\partial t} + v\frac{\partial T_f}{\partial z}\right) = h_f A_t \left(T_f - T_t\right) + h_f A_{sh}\left(T_f - T_{sh}\right) + k_f A_f \frac{\partial T_f}{\partial z} \quad \text{— HTF} \tag{3}$$

$$m_{sh} C_{p,t}\left(\frac{\partial T_{sh}}{\partial t}\right) = h_f A_{sh}\left(T_{sh} - T_f\right) + k_t A_{sh} \frac{\partial T_{sh}}{\partial z} \quad \text{— Shell} \tag{4}$$

$$m_{ins} C_{p,ins,V}\left(\frac{\partial T_{ins,V}}{\partial t}\right) = k_{ins} A_{ins,V} \frac{\partial T_{ins,V}}{\partial z} \quad \text{— Vertical insulation} \tag{5}$$

$$m_{ins} C_{p,ins,H}\left(\frac{\partial T_{ins,H}}{\partial t}\right) = k_{ins} A_{ins,H} \frac{\partial T_{ins,H}}{\partial r} \quad \text{— Horizontal insulation} \tag{6}$$

where *m,Cp,k,T* refer to mass, constant pressure specific heat, thermal conductivity and temperature of each component. *A* is the cross-sectional area of each component, normal to the axial direction of the system. Subscripts "*f,t,s,sh*" denote to HTF, tube, sulfur, and shell. Subscripts "*ins,V*" and "*ins,H*" refer to vertically and horizontally installed insulation respectively. The size and thickness of tube is chosen based on nominal pipe size (NPS) according to American Society of Mechanical Engineers (ASME) standard [63]. The above coupled governing equations are solved in a finite volume approach. The advection term of HTF in Eq. (3) is solved using a hybrid scheme, and the conductive term is via first order central differencing scheme, assuming a piece-wise linear profile. The first order fully implicit scheme is applied to the transient term so that a stability issue can be avoided.

Heat Transfer Coefficients

The interstitial heat transfer coefficients are obtained empirically to avoid the complexity of solving moment interaction between each component. Discussions on empirical correlations for HTF side and sulfur side heat transfer coefficients are presented in the following sections.

The design of the system is based on shell-and-tube heat exchanger, which allows the shell side heat transfer coefficient, h_f, to be obtained based on Bell-Delaware method [64]. For this study, the Bell-Delaware method is utilized because it considers the effect of numerous

geometric terms affecting fluid flow and heat transfer performance, which are accounted for via the coefficients, J and R_1, which are considered as 1.054 and 1.0, respectively. The corrected heat transfer coefficient is denoted as:

$$h_o = J\phi c_{p,f} j \frac{\dot{m}_f}{S_m} Pr_f^{-2/3} \tag{7}$$

where S_m is the crossflow area at the shell centerline and is represented by $S_m = b_s\left[\frac{(W-d_o)}{P_t/d_o}(P_t/d_o - 1)\right]$, b_s is the spacing between baffles, Pr_f is the Prandtl number for the shell-side fluid, ϕ is the wall viscosity compensation term ($\phi = \left(\frac{\mu(T=T_w)}{\mu(T=T_f)}\right)^{0.14}$), and j is the Colburn factor that are correlated by Taborek where coefficients are dependent on the tube layout, tube pitch ratio ($P_r = P_t/d_o$), and Reynolds number. These factors are given as $j = a_1\left(\frac{1.33}{P_r}\right)^a Re_D^{a_2}$ and $f = b_1\left(\frac{1.33}{P_r}\right)^b Re_D^{b_2}$ where the coefficients are tabulated based on empirical results from testing with shell and tube heat exchangers.

Different sulfur side heat transfer coefficients are adopted when sulfur is in a different physical state. The sulfur exists in a solid state at temperatures less than 115°C, and, thus, a conductive heat transfer coefficient h_{cond} (w/(m^2 K)) is used to characterize the conduction heat transfer within sulfur. Initially, a transient temperature distribution within sulfur was obtained by solving a 1D, transient energy conservation as shown in Eq. (8). Then conductive convection coefficient, h_{cond} and effective Nusselt number is computed as shown in Eqs. (9)–(10).

$$\frac{1}{r}\frac{\partial}{\partial r}\left(r\frac{\partial T(r,t)}{\partial r}\right) = \frac{1}{\alpha}\frac{\partial T(r,t)}{\partial t} \tag{8}$$

$$h_{cond}(t) = -k\frac{\left(\frac{\partial T(r,t)}{\partial r}\right)_{r=R}}{T_t - T_s(t)} \tag{9}$$

$$Nu(t) = \frac{h_{cond}(t)D_i}{k} \tag{10}$$

Where, T_s is the cross-sectional area-averaged sulfur temperature at each time instance, α is the thermal diffusivity of sulfur, and R is the inner radius of the tube. Tube temperature is required as boundary condition for solving Eq. (8). However, during thermal charging, the tube temperature is a dependent variable and is not readily known. Thus, to close the problem, a nondimensional sulfur temperature, T^* is defined to correlate instantaneous h_{cond}(t) with sulfur and tube temperature.

$$T^* = \frac{T_s - T_{s,i}}{T_t - T_{s,i}} \tag{11}$$

where $T_{s,i}$ is the initial sulfur temperature. In each time step, T^* can be calculated based on T_s and T_t from the previous time step, and the corresponding Nusselt number can be obtained based on the following correlation:

$$Nu = 3637.596T^{*6} - 12804.29T^{*5} + 18022.76T^{*4} - 12925.86T^{*3} + 4980.08T^{*2} - 992.17T^* + 90.54 \tag{12}$$

As sulfur temperature increases to beyond melting temperature, liquid sulfur appears, and natural convection inside sulfur gradually becomes the dominant heat transfer mode.

Nithyanandam et al., [46] studied sulfur heat transfer performance during thermal cycling in a low temperature range, between 50°C and 200°C, to characterize sulfur heat transfer with phase-change. A Nusselt number correlation as a function of solid-liquid Rayleigh number can be obtained as:

$$Nu = 2.230Ra_{s-l}^{0.1702} - 0.746 \text{ charge} \quad (13)$$

$$Nu = 9.711 \times 10^{-6}Ra_{s-l}^{1.018} + 6.955 \text{ discharge} \quad (14)$$

where solid-liquid Rayleigh number is defined as $\boldsymbol{Ra_{s-l} = \frac{\rho^2 C_p g\beta(T_s - T_t)[d_i(1-\sqrt{1-\gamma}]^3}{\mu k}}$, $\boldsymbol{d_i}$ is the inner diameter of the tube and $\boldsymbol{\gamma}$ is the liquid fraction that determines the characteristic length during phase-change process. The liquid fraction with corresponding $\boldsymbol{T_s}$ is also provided by Nithyanandam et al.,[46], shown in Figure 60, and their correlation can be obtained by curve fitting, shown as Eq. 15.

Figure 59: Sulfur Fraction and Liquid Fraction

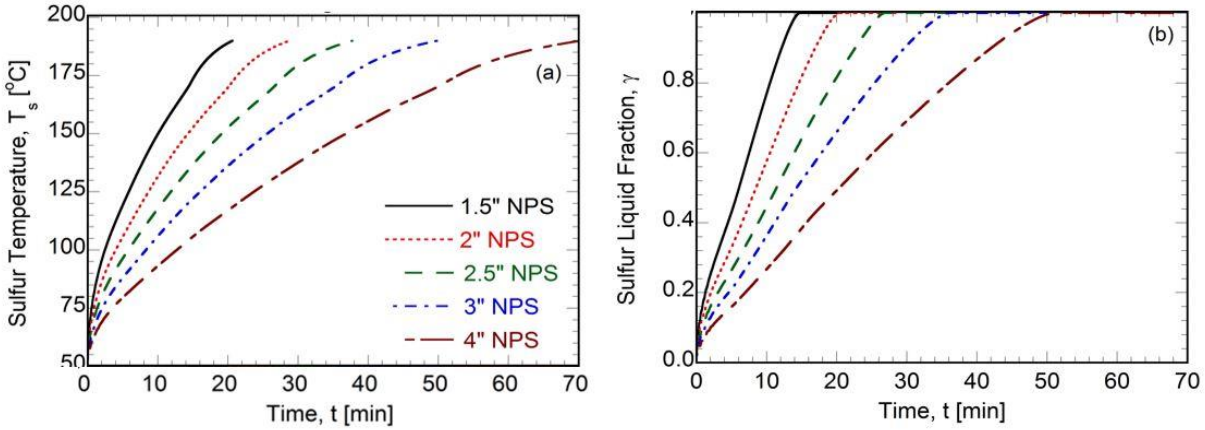

(a) Area averaged sulfur temperature with (b) Corresponding liquid fraction.

Source: UCLA, Wirz Research Group

$$\gamma = -1.44 \times 10^{-8}T_s^4 + 6.73 \times 10^{-6}T_s^3 - 1.12 \times 10^{-3}T_s^2 + 0.087T_s - 2.5 \quad (15)$$

When sulfur temperature is in high temperature range, from 200°C to 600°C, where sulfur is in pure liquid phase, natural convection dominates the energy transfer. Nithyanandam et al., [45,46] proposed Nusselt number correlations in this high temperature range to characterize heat transfer rate of sulfur expressed as:

$$Nu = 0.909Ra^{0.242} - 1.612 \text{ charge} \quad (16)$$

$$Nu = 0.545Ra^{0.238} - 0.79 \text{ discharge} \quad (17)$$

where $Ra = \frac{g\beta d_i^3(T_s - T_t)\rho^2 C_p}{\mu k}$.

The Nusselt number correlations developed by Nithyanandam et al., for 50—200°C and 200—600°C were integrated to obtain a single correlation to characterize the sulfur heat transfer over 50—600°C. The integrated correlations for sulfur charge/discharge are presented as:

$$Nu = 0.6228Ra^{0.2611} - 1.376 \text{ charge} \quad (18)$$

$$Nu = 0.4995Ra^{0.2409} + 0.4571 \text{ discharge} \quad (19)$$

Figure 61 shows the comparison of integrated Nusselt number correlations with independent Nusselt number correlations developed for low (50—200°C) and high temperatures (200—600°C). The integrated correlations are in agreement with the original correlations with average errors of 5.02 percent and 6.31 percent for low-temperature charge/discharge, while 0.58 percent and 1.42 percent for high-temperature charge/discharge, respectively.

Figure 60: Unified Comparisons of Integrated Number Correlations

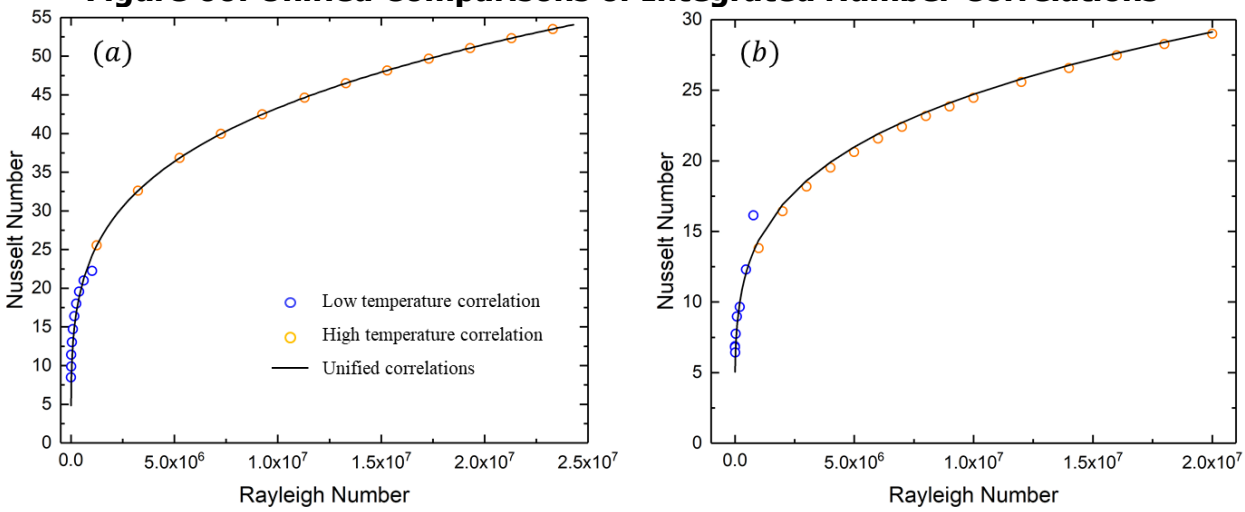

(a) charge, (b) discharge correlations compared to correlations from high and low temperature studies

Source: UCLA, Wirz Research Group

In the beginning of the phase-change process, conduction is still dominant, where liquid fraction and Ra_{SL} are close to zero, leading to an unrealistically small heat transfer coefficient. To avoid this, the conductive heat transfer coefficient will also be evaluated simultaneously and compared to the convective heat transfer coefficient. The larger one will be adopted, as it indicates the transition between conduction-dominant to convection-dominant.

Thermo-Physical Properties

Thermal physical properties (C_p, ρ, k) of HTF (air) are obtained from National Institute of Standards and Technology (NIST) Chemistry WebBook, Standard Reference Database [65], and those of sulfur are from Sulfur Data Book [66]. Temperature dependency of above two sets of material properties are obtained by curve fitting and shown in Table 6 and Table 7. Constant properties are used for steel tubes where $\rho_t = 8000\ kg/m^3$, $C_{p,t} = 550\ J/kg\ K$ and $k_t = 19\ W/mK$.

In the sulfur solid-liquid phase change, the melt front starts from the peripheral and concentrically propagates toward the center of the tube. Predicting volumetric-averaged sulfur temperature thus requires the incorporation of latent heat. The project team has formulated a correlation for effective specific heat capacity to account for the latent heat of sulfur via volumetric liquid fraction and is presented as:

$$C_{p,s,eff} = \frac{C_{p,s}(T_{pc,start} - T_D) + C_{p,s}(T_{pc,end} - T_{pc,start})Q^*(\gamma)}{(T_s - T_D)} \quad (20)$$

In Eq. (20), $T_{pc,start}$ and $T_{pc,end}$ refer to area averaged sulfur temperature when solid-liquid phase change starts and ends respectively. Q^* is a dimensionless energy content, defined as:

$$Q^*(\gamma) = \frac{m_s C_{p,s}(T_C - T_D) + \gamma m_s l}{m_s C_{p,s}(T_C - T_D)} \quad (21)$$

where l is the latent heat of solid-liquid phase change. The correlation between Q^* and γ can be obtained from Nithyanandam's study in low temperature range [0] as:

$$Q^* = -0.23\gamma^2 + 1.28\gamma + 0.11 \quad (22)$$

where $\boldsymbol{\gamma}$ changes from 0 to 1, and $\boldsymbol{Q^*}$ is observed to increase from 0 to around 1.3, shown in Figure 62.

.

Figure 61: Liquid Fraction and Corresponding Dimensionless Energy Content

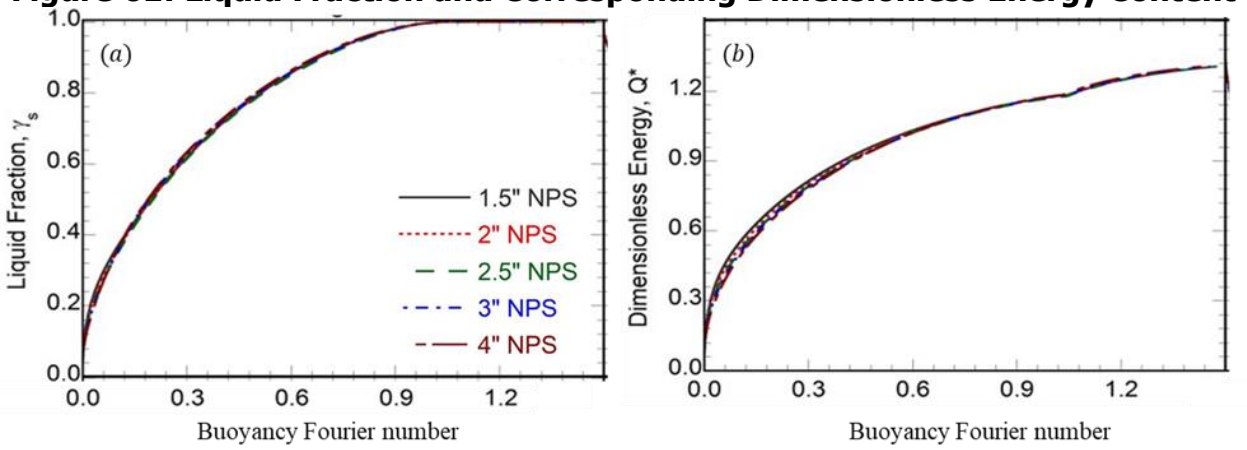

(a) liquid fraction and (b) corresponding dimensionless energy content [0]

Source: UCLA, Wirz Research Group

The model uses sulfur temperature from the previous time step to calculate liquid fraction according to Eq.15, and corresponding Q^* based on Eq.22. Subsequently, $C_{p,s,eff}$ can be acquired based on Eq. 20.

Table 6: Thermal Properties of Heat Transfer Fluid (Air)

Properties	Air (unit of T: ^oC)
Density, ρ $[kg/m^3]$	$(1.52E-12)T^4 - (7.35E-9)T^3 + (1.29E-5)T^2 - 9.91T + 3.243$
Specific heat , C_p $[J/kg\ K]$	$(1.12E-13)T^4 - (5.35E-10)T^3 + (8.27E-7)T^2 - (2.59E-4)T + 1.0321$
Viscosity, μ $[kg/m\ s]$	$(-3.97E-13)T^4 + (2.15E-9)T^3 - (4.70E-6)T^2 + (6.99E-3)T + 0.109$
Thermal conductivity, k $[W/m\ K]$	$(3.23E-13)T^4 + (1.96E-9)T^3 - (5.16E-6)T^2 + (1.03E-2)T + 0.064$

Source: UCLA, Wirz Research Group

Table 7: Thermal Properties of Sulfur

Properties	Sulfur (unit of T: ^oC)
Density, ρ $[kg/m^3]$	$(-4.55E-6)T^3+(3.94E-3)T^2-1.64T+1952.43$
Specific heat , C_p $[J/kg\ K]$	$0.556T+943$
Viscosity (T < 340 ^oC) , μ $[kg/m\ s]$	$(4.38E-8)T^3-(4.62E-5)T^2+0.015T-1.53$
Viscosity (T > 340 ^oC) , μ $[kg/m\ s]$	$EXP(-8.74+3914.07/(T+273.15))$
Thermal conductivity, k $[W/m\ K]$	$(2.15E-4)T+0.048$

Source: UCLA, Wirz Research Group

Model Validation

The model was validated using experimental results of lab demonstrations of the SulfurTES battery, described in Chapter 5. The numerical model was used to predict the temperature distribution within SulfurTES battery for the identical initial and boundary conditions as observed during the experimental analysis.

Figure 62: Locations of Tube Temperature Measurements Along the Axis

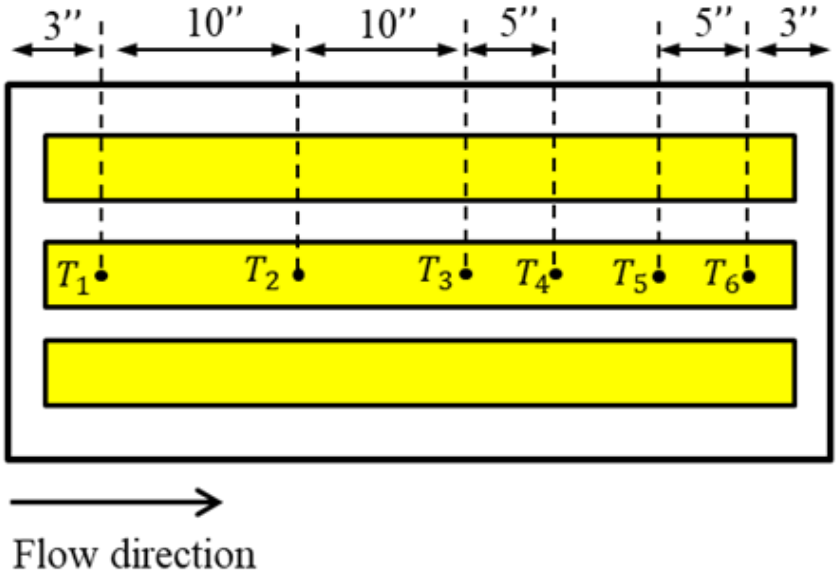

Source: UCLA, Wirz Research Group

Figure 63: Comparison Between Predicted and Measured Tube Temperature

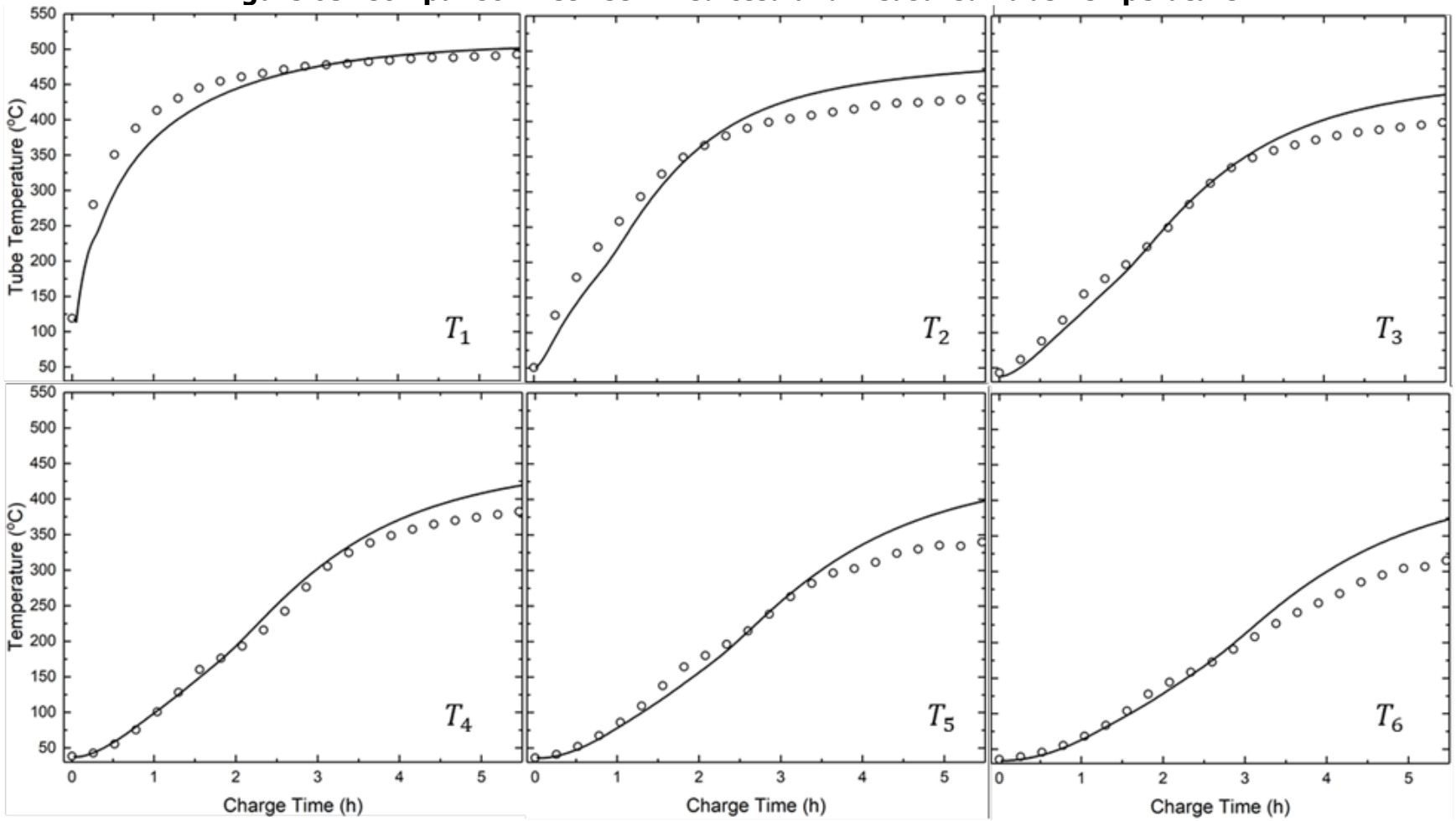

Source: UCLA, Wirz Research Group

Figure 64 shows the comparison of measured and predicted tube temperature at locations shown in Figure 62 during thermal charging. The relative error for T_1 to T_6 are 2.9 percent, 4.5 percent, 4.1 percent, 3.2 percent, 6.9 percent, and 8.7 percent, respectively. The predicted results compare well with experimental results in earlier stage of charging (before 3.5 hours), while the model overpredicts the tube temperatures later (greater than 3.5 hours) into the charging process. The overprediction of tube temperatures could be the result of the additional heat loss during experiments, due to imperfect installation of insulation panels. These imperfections provide pathways with higher effective conductivity for heat to escape to the ambient, and such practical imperfections could not be accurately incorporated in the numerical model. These effects become prominent at later stages during thermal charging due to higher system temperatures and accumulation of the total heat loss. Despite these practical limitations, ~5 percent average error shows that the model can well predict the temperature distribution within the SulfurTES battery and can be used for the parametric study of the SulfurTES systems.

Parametric Study of 1 MWh System

The design parameters of SulfurTES battery were selected based on TEMA standards [58] and recommendations from heat exchanger design handbook [64] to match with standardized design pattern. According to the heat exchanger design handbook, the shell inner diameter, $D_{sh,i}$, and the tube outer diameter, d_o, are two independent design variables that are often determined based on the user requirements. Thus, they were selected for the parametric study. The presentation of shell geometry was simplified using shell aspect ratio, AR, where $AR = L/D_{sh,i}$.

The performance of the SulfurTES battery was investigated for specific operating conditions of the charge/discharge temperature, T_C/ T_D, charge/discharge period and mass flow rate of HTF. The charge/discharge temperatures were selected as 600°C and 50°C, respectively, to investigate the SulfurTES performance for the temperatures relevant for low to high temperature applications. A six-hour charge period was selected for all test cases, to simulate the average time period available for the solar thermal charging. A time period of 12-hours was selected for discharging. Since the parametric study was conducted independent of any specific heat source and/or application, selection of an appropriate range of the HTF mass flow rate relevant for the one MWh SulfurTES system was necessary. Initially, we defined a reference mass flow rate as:

$$\dot{m}_{ref} = \frac{Q_{store}}{C_{p,f}(T_C - T_D)t} \quad (23)$$

Where Q_{store} is the storage capacity and t refers to the charge/discharge time. A nondimensional mass flow rate, $\dot{m}^*$ was defined to represent the actual mass flow rate, wherein, $\dot{m}^* = \frac{\dot{m}_{act}}{\dot{m}_{ref}}$. For this study, researchers selected $\dot{m}^*$ in the range of 0.5-1.5, which corresponds to the amount of energy supply from 0.5 to 1.5 times of the storage capacity.

Performance Characterization

The system level performance metrics consist of a set of performance parameters including storage capacity utilization, charge/discharge utilization, and round-trip efficiency.

Performance of systems within the design space were observed and analyzed with varying $\dot{m}^*$ (Figure 64).

Storage Capacity Utilization and Charge Utilization

Storage capacity utilization and charge utilization demonstrate charging performance of SulfurTES battery. The storage capacity utilization shows the percentage of storage capacity that has been used by the end of charging, expressed as:

$$U_{Capacity} = \frac{Actual\ energy\ stored\ in\ sulfur\ and\ tube}{Energy\ storage\ capacity} = \frac{m_s C_{p,s}(T_s - T_D) + m_t C_{p,t}(T_t - T_D)}{m_s C_{p,s}(T_C - T_D) + m_t C_{p,t}(T_C - T_D)} \quad (24)$$

Charge utilization is expressed as:

$$U_C = \frac{Net\ stored\ energy}{Energy\ supplied} = \frac{\int_0^{t_C} \dot{m}_f C_{p,f}(T_C - T_{out,c})dt - \int_0^{t_C} h_{loss} A_{surf}(T_{ins} - T_o)dt}{\int_0^{t_C} \dot{m}_f C_{p,f}(T_C - T_D)dt} \quad (25)$$

which is the ratio between net stored energy (energy absorbed minus heat loss) and energy provided by HTF.

Figure 64: Charge and Storage Utilization Performance

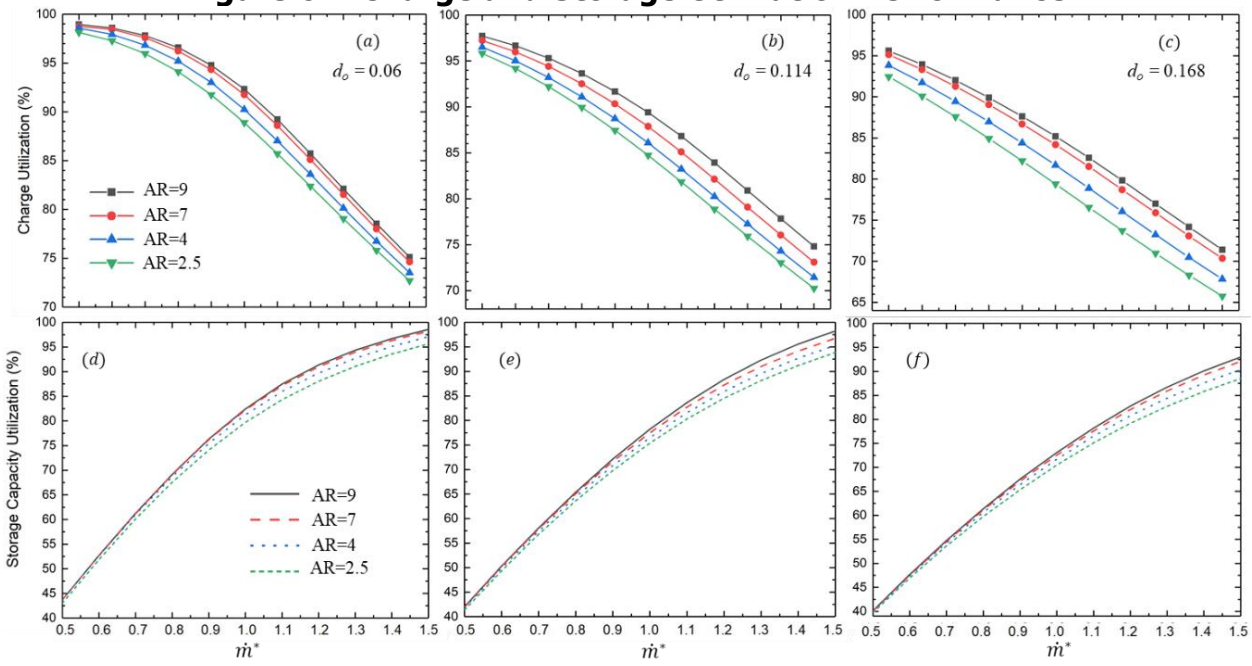

(a) D_o = 0.06 M, (b) D_o = 0.114 M, (c) D_o = 0.168 M and storage capacity utilization for (d) D_o = 0.06 M, (e) D_o = 0.114 M, (f) D_o = 0.168 with varying $\dot{m}^*$

Source: UCLA, Wirz Research Group

As shown in Figure 64, with increase in $\dot{m}^*$ from 0.5 to 1.5, the charge utilization decreases from near 100 percent to around 70 percent, while storage capacity utilization increases from about 40 percent and approaches 100 percent. System temperature and capacity utilization remain low while low flow rate is supplied. Because of the low system temperature, a relatively large temperature difference stays between HTF and the system, providing high potential for energy transfer, so that a higher charge utilization is achieved. The charge utilization keeps decreasing with increasing $\dot{m}^*$, because the system is approaching full charge (storage

capacity utilization approaches 100 percent), therefore additional energy supply is being wasted.

Geometric dependency is also observed from Figure 64 given that longer *AR* yields higher charge utilization and a slightly higher capacity utilization of around 5 percent. Because the system with longer *AR* has a smaller flow area and a higher flow velocity, the shell side heat transfer coefficient is higher, leading to better thermal performance. Tube size also affects the system level performance, where a larger tube size yields lower charge utilization. Larger tube size associates with a smaller number of tubes required, reducing the surface area for the heat transfer between HTF and sulfur.

In general, capacity utilization is positively related to mass flow rate, while the opposite is true for charge utilization. Shell geometry that produces superior shell side heat transfer performance is beneficial to thermal performance during charging.

Charge Exergetic Efficiency

The exergetic efficiency provides an assessment on how closely the system operates near ideal condition where all useful work can be acquired. The definition of charge exergetic efficiency is analogous to that of charge utilization, presenting the ratio of exergy stored, equivalent to exergy absorbed minus exergy destruction, and exergy provided, expressed as [73]:

$$\phi_c = \frac{Acutal\ exergy\ stored}{Exergy\ supplied} \frac{\int_0^{t_C} \dot{m}_f C_{p,f}\left((T_C - T_{out,c}) - T_o\, ln\left(\frac{T_C}{T_{out,c}}\right)\right)dt - \frac{\dot{m}_f W}{\eta} t_C}{\int_0^{t_C} \dot{m}_f C_{P,f}\left((T_C - T_o) - T_o ln\left(\frac{T_C}{T_o}\right)\right)dt} \quad (26)$$

The term $\frac{\dot{m}_f W}{\eta} t_C$ represents the amount of exergy destruction by pumping HTF through the system. Since air is a compressible ideal gas, the work required in moving air, *W*, can be treated as an isentropic process that depends on the system's pressure drop. Efficiency (η) is the product of compressor efficiency and energy conversion efficiency.

Figure 65: Charge Exergetic Efficiency

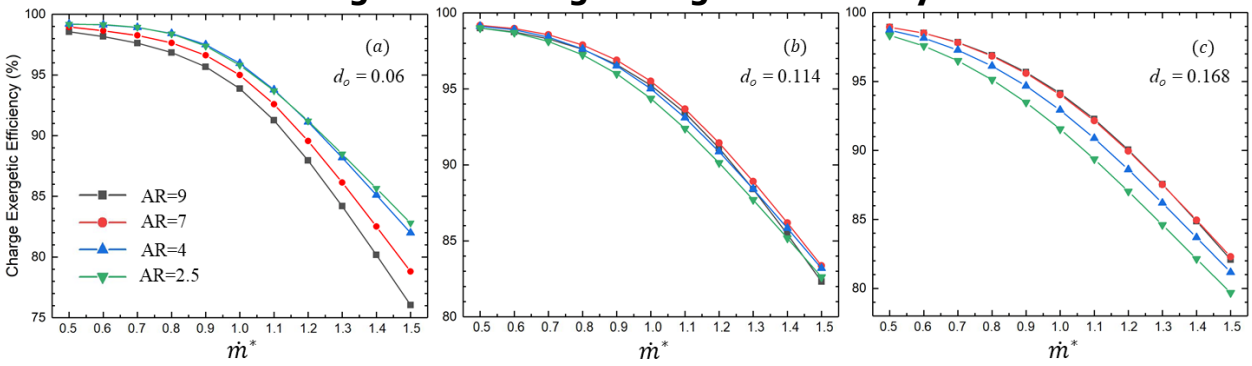

With varying $\dot{m}^*$ for (a) d_o = 0.06 m, (b) d_o = 0.114m, (c) d_o = 0.168 m.

Source: UCLA, Wirz Research Group

Figure 65 shows that the dependency of charge exergetic efficiency on mass flow rate is similar to that of charge utilization. The system's ability to efficiently absorb useful work decreases with an increase in the mass flow rate. However, its dependency on shell aspect ratio is different, due to exergy destruction by pump work. Although, a larger *AR* provides

better heat transfer performance that is beneficial to exergy absorption, it also requires higher pump work due to increased flow velocity and pressure drop. Therefore, with tube diameter decreasing and shell *AR* increasing, the amount of exergy destruction overcomes the benefit from better thermal performance, leading to an inverse relationship with charge exergetic efficiency. The effect of pump work diminishes when tube size increases. For instance, the charge exergetic efficiency of systems with d_o = 0.114 m and *AR* = 9 nearly merges with that of the system whose *AR* = 4, while the system with d_o = 0.168 m, *AR* = 9 provides similar results as that by *AR* = 7.

Discharge Utilization and Round-Trip Efficiency

The discharging performance is characterized by discharge utilization, which refers to the percentage of energy recovered from discharging by net stored energy from charging, expressed as:

$$U_D = \frac{Energy\ recovered}{Net\ stored\ energy} = \frac{\int_0^{t_D} \dot{m}_f C_{p,f}(T_{out,D} - T_D)dt}{\int_0^{t_C} \dot{m}_f C_{p,f}(T_C - T_{out,c})dt - \int_0^{t_C} h_{loss} A_{surf}(T_{ins} - T_o)dt} \quad (27)$$

The round-trip efficiency provides insight into the system's performance for the entire thermal cycle. It is defined as the ratio of energy recovered from discharging to energy supplied during charging. Mathematically, it is also the product of charge and discharge utilization with the following expression:

$$U_{roundtrip} = U_c \times U_D = \frac{Energy\ recovered}{Energy\ supplied} = \frac{\int_0^{t_D} \dot{m}_f C_{p,f}(T_{out,D} - T_D)dt}{\int_0^{t_C} \dot{m}_f C_{p,f}(T_C - T_D)dt} \quad (28)$$

Figure 66: Discharge Utilization and Round-trip Efficiency Rates

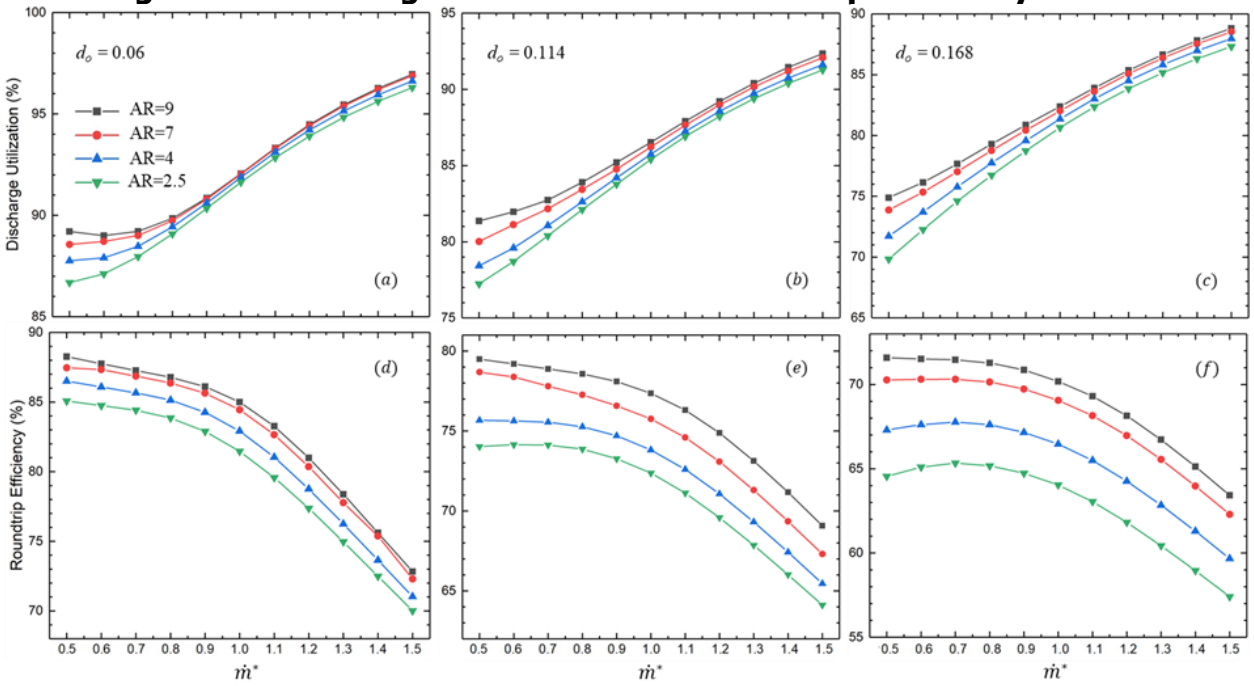

(a) d_o = 0.06 m, (b) d_o = 0.114 m, (c) d_o = 0.168 m and Round-trip Efficiency (d) d_o = 0.06 m, (e) d_o = 0.114 m, (f) d_o = 0.168 m with Varying $\dot{m}^*$

Source: UCLA, Wirz Research Group

Figure 66 presents discharge utilization and round-trip efficiency for all configurations with varying mass flow rates. Variation in discharge utilization with varying shell aspect ratio and tube diameter follows a similar trend as what has been observed for charge utilization. However, unlike charge utilization, discharge utilization is proportional to the increase in mass flow rate, because higher mass flow rate leads to a higher rate of energy recovery, extracting a larger amount of stored energy in the same time span. Round-trip efficiency stays relatively constant when $\dot{m}^*$ is less than 1, followed by a drop as $\dot{m}^*$ increasing beyond 1. Since the charge/discharge utilization is negatively/positively related to mass flow rate respectively, their combined effect yields a somewhat similar round-trip efficiency with $\dot{m}^*$ less than 1. As $\dot{m}^*$ increasing beyond 1, the system is highly charged ($U_{Capacity}$ > ~75%), therefore a prominent decrease in charge utilization dominates the change in round-trip efficiency, causing that steep drop.

Geometric dependency of round-trip efficiency shows a similar trend to that of charge/discharge utilization as expected, where larger *AR* and smaller tube size bring higher round-trip efficiency.

In summary, the increase in mass flow rate provides improving discharge utilization, but the performance of entire thermal cycle may be restricted by energy waste during charging that lowers the charge utilization and round-trip efficiency.

Discharge Exergetic Efficiency

The discharge exergetic efficiency is defined by the ratio of net available exergy in the system to the initial exergy stored in the system [73]. The net available exergy is the summation of recovered exergy and remaining exergy with exergy destruction excluded.

$$\phi_D = \frac{Exergy\ remaining + Exergy\ recovered - Exergt\ destruction}{Exergy\ stored}$$
$$= \frac{m_s C_{p,s}\left((T_s - T_D) - T_o ln\left(\frac{T_s}{T_D}\right)\right) + m_t C_{p,t}\left((T_t - T_D) - T_o ln\left(\frac{T_t}{T_D}\right)\right)}{m_s C_{p,s}\left((T_{i,s} - T_D) - T_o ln\left(\frac{T_{i,s}}{T_D}\right)\right) + m_t C_{p,t}\left((T_{i,t} - T_D) - T_o ln\left(\frac{T_{i,t}}{T_D}\right)\right)}$$
$$+ \frac{\int_0^{t_D} \dot{m}_f C_{p,f}\left((T_{out,D} - T_D) - T_o\, ln\left(\frac{T_{out,D}}{T_D}\right)\right) dt - \frac{\dot{m}_f W}{\eta} t_D}{m_s C_{P,s}\left((T_{i,s} - T_D) - T_o ln\left(\frac{T_{i,s}}{T_D}\right)\right) + m_t C_{P,t}\left((T_{i,t} - T_D) - T_o ln\left(\frac{T_{i,t}}{T_D}\right)\right)} \quad (29)$$

where $T_{i,s}$ and $T_{i,t}$ are initial sulfur and tube temperature at the beginning of discharging.

Figure 67 presents time dependent discharge exergetic efficiency for six system configurations, covering upper and lower limits of shell *AR* and all three tube sizes. As discharging proceeds, an increasing amount of exergy has been recovered from the system, while the amount of exergy remained in the system decreases. When the stored exergy is nearly drained, the further decrease in the remaining exergy and further increase in the exergy recovery approach cessation, leading to a plateau in the change of ϕ_D with time. For the system with small shell *AR* (*AR*=2.5), ϕ_D plateaus at values in a descending order with decreasing mass flow rate. For instance, the system with shell *AR*=2.5 and d_o = 0.06, ϕ_D decreases from nearly 100 percent and plateaus at around 60 percent for $\dot{m}^*$=1.5 and around 45 percent for $\dot{m}^*$=0.5.

Figure 67: Discharge Exergetic Efficiency for Different System Configurations

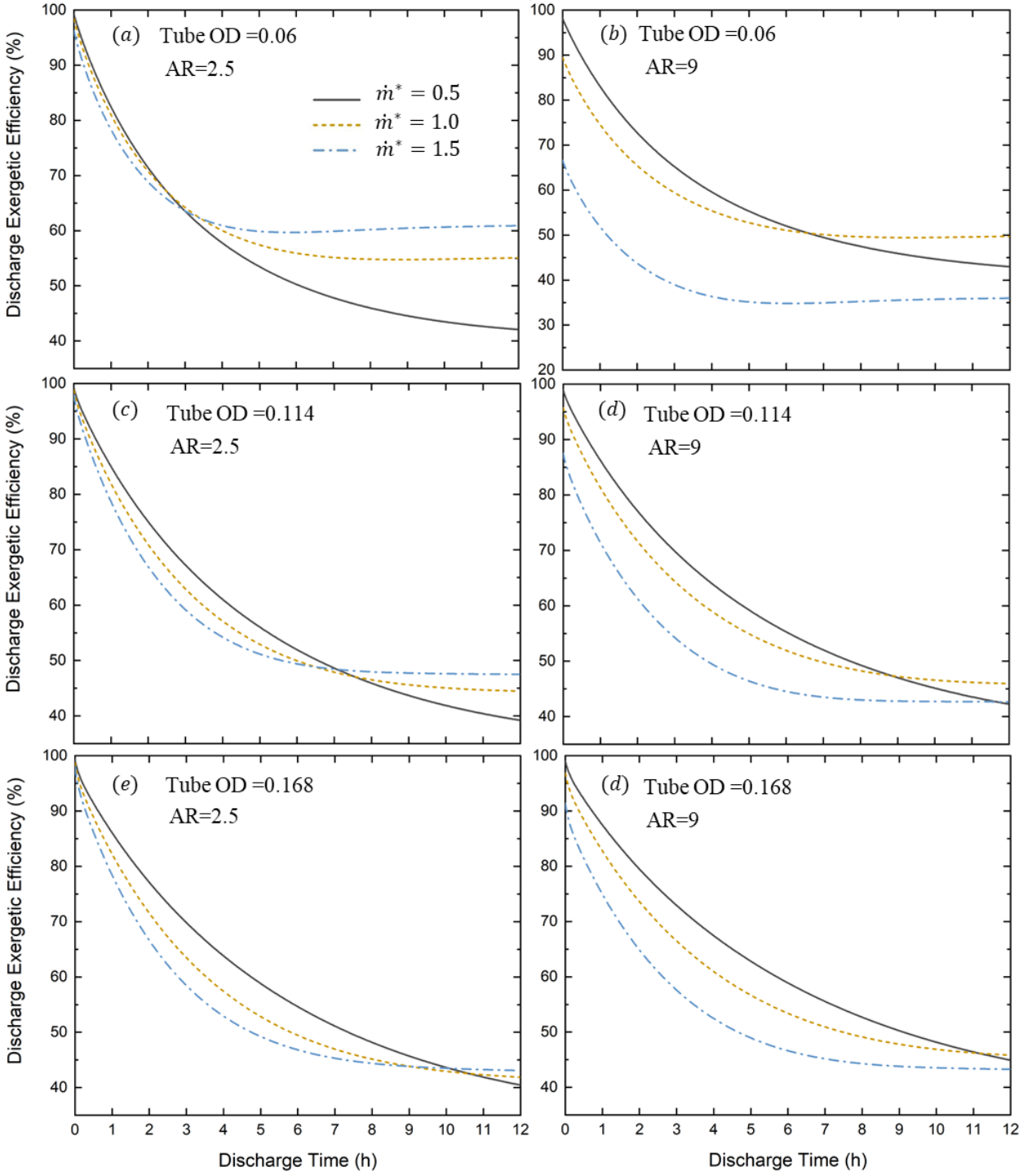

With (a) d_o = 0.06 M and AR = 2.5, (b) d_o = 0.06 M And AR = 9, (c) d_o = 0.114 M and AR = 2.5, (d) d_o = 0.114 M and AR = 9, (e) d_o = 0.168 M and AR = 2.5, (f) d_o = 0.168 M and AR = 9 with Varying Mass Flow Rate

Source: UCLA, Wirz Research Group

Discharging with higher mass flow rate provides high-temperature exhaust at a faster rate, yielding a larger amount of exergy recovery. For a long time into discharging, exergy remaining approaches zero, the amount of exergy recovery dominates the value of $\boldsymbol{\phi_D}$. Therefore, by providing a high amount of exergy recovery, discharging with high mass flow rate yields high $\boldsymbol{\phi_D}$. In contrast, the above described dependency of $\boldsymbol{\phi_D}$ on mass flow rate is

not entirely true for large shell *AR* (*AR=9,*) due to the prominent effect of exergy destruction by pump work. As discussed in the charging performance section, large shell *AR,* small tube size, and high mass flow rate lead to high pump work. Although high mass flow rate still provides high exergy recovery, exergy destruction is prominent to worsen the exergetic efficiency. As shown in Figure 67, for system with shell *AR*=9 and d_o = 0.06, with $\dot{m}^*$=1.5, ϕ_D starts from about only 70 percent, drops quickly to less than 40 percent in three hours and reaches the plateau, whereas for the same system with $\dot{m}^*$=0.5, ϕ_D drops from near 100 percent, and slowly approaches 40 percent in 12 hours.

In summary, discharging with high mass flow rate is generally beneficial to the discharge performance, but care should be taken in balancing the exergy recovery and exergy destruction, especially for a system with large shell *AR* and small tube size.

Design Guidance of Industrial Scale SulfurTES System

This section presents a suggested design tool for system design based on user-defined operating conditions and performance requirements. The design tool consists of two sections: a design space, and an iterative design procedure. The design space is bound by the upper and lower limits of $\dot{m}^*$ with corresponding shell *AR* to achieve required system performance. Based on the design space, an iterative design procedure will be followed, from which design parameters can be determined, meeting all performance requirements.

The system level performance is characterized by a set of performance parameters. A successfully designed system should satisfy requirements on each performance parameter. Table 8 shows a set of example requirements of performance parameters. It is a representative example, serving demonstrative purpose.

Table 8: Example Performance Requirements

$U_{Capacity}$	U_c	ϕ_C	$U_{roundtrip}$	ϕ_D
>= 75%	>= 85%	>= 85 %	>= 75%	>= 50% in 8 h

Design Space Determination

As seen from the previous section, except ϕ_D, the first four performance parameters change monotonically with changing mass flow rate, where $U_{capacity}$ increasing and U_C, ϕ_C and $U_{roundtrip}$ decreasing monotonically with increasing mass flow rate. Therefore, the requirement on $U_{capacity}$ yields a lower bound on mass flow rate, $\dot{m}^*_{min}$.

As shown in Source: UCLA, Wirz Research Group

, $\dot{m}^*_{min}$ should be around 0.85 for shell *AR* = 9,7 and 4 and 0.9 for shell *AR* = 2.5 to have $U_{capacity}$ being higher than 75 percent.

Figure 68: Storage Capacity Utilization for Systems with D_o = 0.06 Under Varying Mass Flow Rate

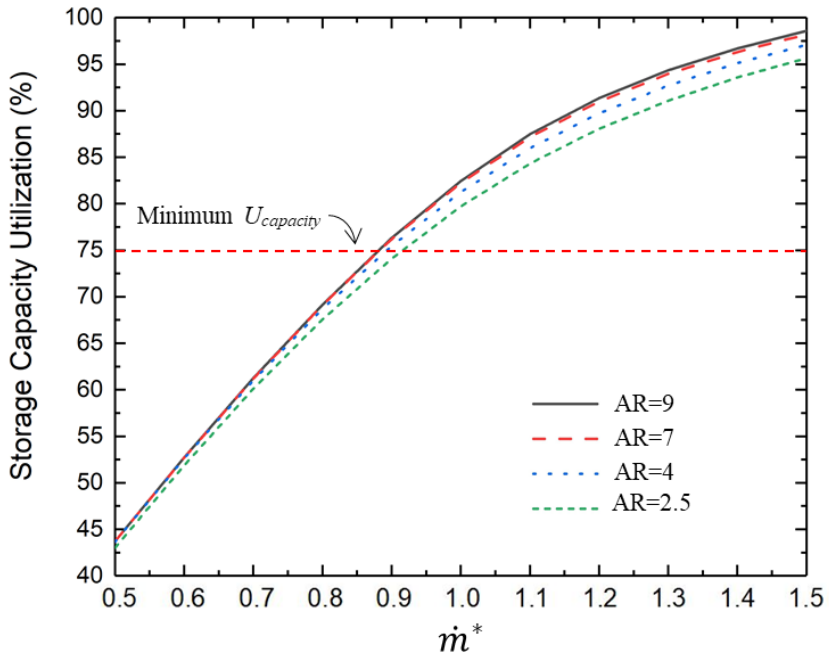

Source: UCLA, Wirz Research Group

The mass flow rate $\dot{m}^*_{max}$ is comparing requirements for U_C, ϕ_C and $U_{roundtrip}$. Figure 69 shows that, with increasing $\dot{m}^*$, U_C reaches its requirement of 85 percent while the other two performance parameters are still above required values. Therefore, based on the restriction on U_C, the upper bound, $\dot{m}^*_{max}$,is found to be 1.1, 1.15, 1.2, and 1.23 for shell *AR* = 2.5, 4, 7, and 9, respectively.

Figure 69: Charge Utilization, Charge Exergetic Efficiency and Round-Trip Efficiency Rates

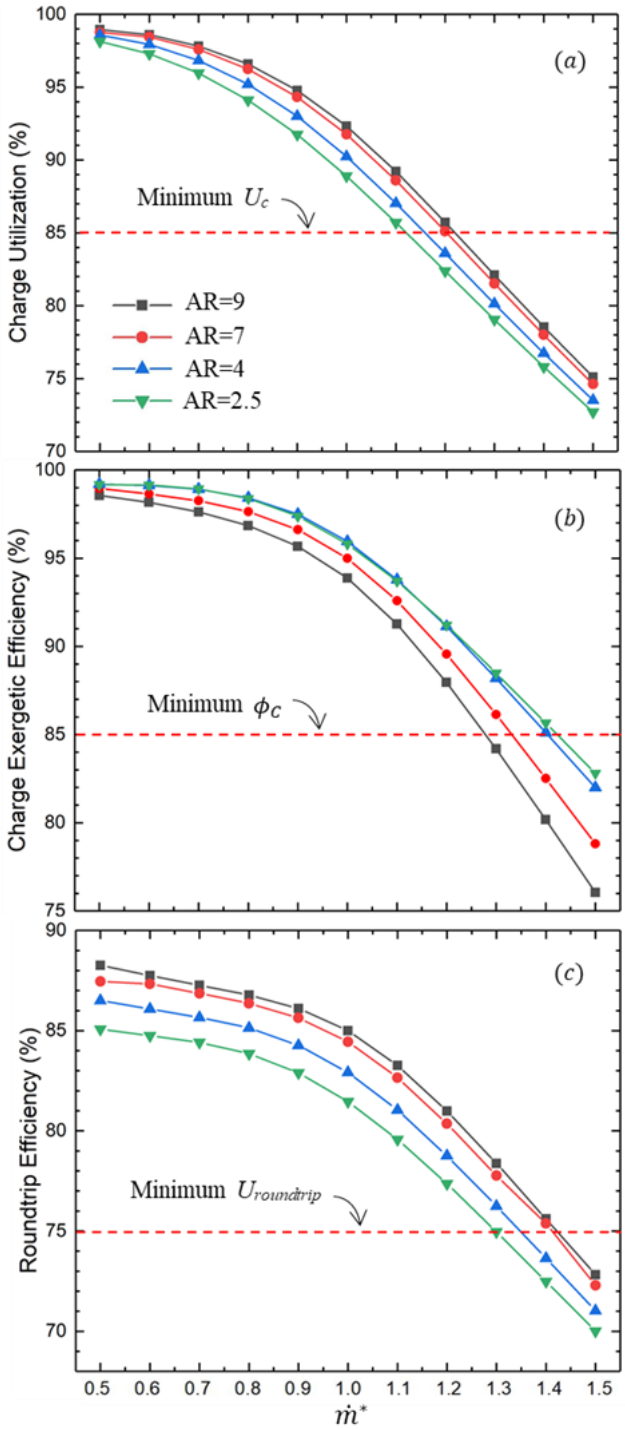

(a) Charge Utilization, (b) Charge Exergetic Efficiency, (c) Round-Trip Efficiency for Systems with D_o = 0.06 Under Varying Mass Flow Rate

Source: UCLA, Wirz Research Group

Figure 70 shows the discharge exergetic efficiency of systems with different shell *AR* at eight hours of discharging for a range of mass flow rates. As shown in Figure 70, ϕ_D does not vary monotonically with $\dot{m}^*$ when shell *AR* is large (*AR* =7,9) due to significant exergy destruction by pump work. Therefore, a range of $\dot{m}^*$ exists between $\dot{m}^*_{\phi_D,min}$ and $\dot{m}^*_{\phi_D,max}$, that satisfies

the requirement of ϕ_D. For systems with smaller shell *AR* (*AR* =2.5,4), $\dot{m}^*_{\phi_D,max}$ is not available in the current range of mass flow rate, therefore, only an $\dot{m}^*_{\phi_D,min}$ is needed to meet ϕ_D requirement.

Figure 70: Discharge Exergetic Efficiency of Systems

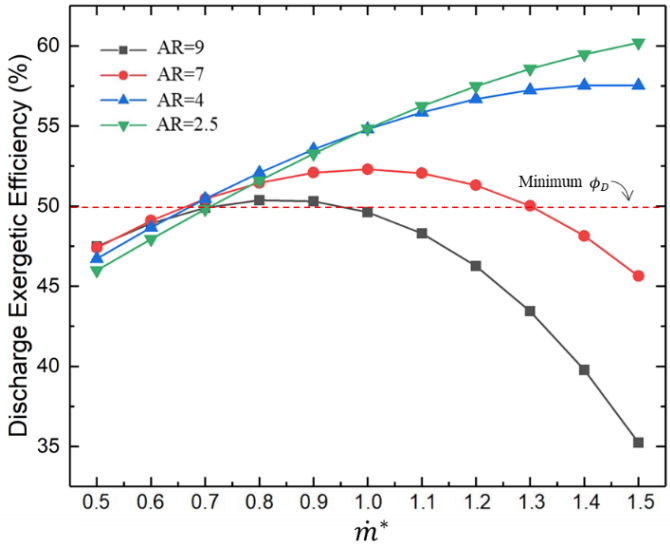

With D_o = 0.06 at 8 hours into discharging under varying mass flow rate.

Source: UCLA, Wirz Research Group

Observation on ϕ_D shows that $\dot{m}^*$ is between 0.7 and 0.9 for shell *AR* = 9, or between 0.7 and 1.3 for shell *AR* = 7. But for systems with shell *AR* = 2.5 and 4, having a $\dot{m}^*$ larger than 0.7 satisfies the above-mentioned requirement within the current range of mass flow rate.

By comparing $\dot{m}^*_{min}$ and $\dot{m}^*_{max}$, obtained based on requirements on the first four performance parameters, to $\dot{m}^*_{\phi_D,min}$ and $\dot{m}^*_{\phi_D,max}$, determined by requirement on ϕ_D, the range of $\dot{m}^*$ that satisfies all five parameters can be found. The smaller among $\dot{m}^*_{max}$ and $\dot{m}^*_{\phi_D,max}$, is set to be the upper limit on $\dot{m}^*$, and the larger one among $\dot{m}^*_{\phi_D,min}$ and $\dot{m}^*_{min}$ is chosen as the lower limit on $\dot{m}^*$.

Figure 71: Design Space Presentation

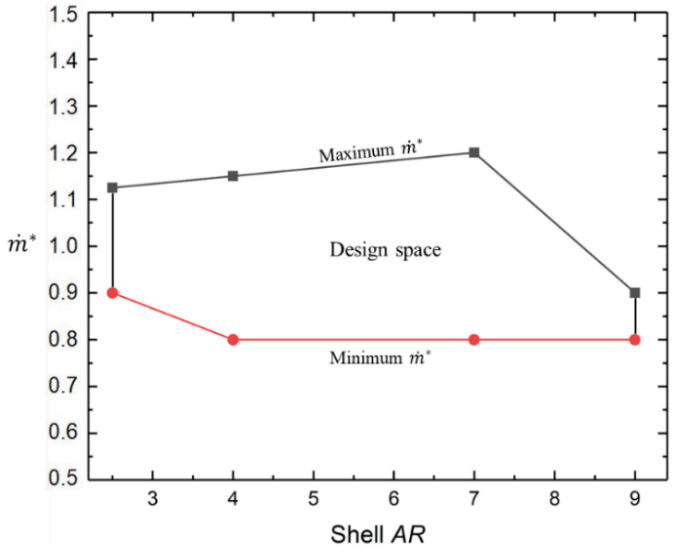

Source: UCLA, Wirz Research Group

Based on the described comparison, lower and upper bounds of $\dot{m}^*$ for each corresponding shell *AR* are determined and presented in Figure 71. The area between curves of upper and lower limit of $\dot{m}^*$ composes the design space that meets the specified performance requirements in Table 8. The study observed that with shell *AR* between 4 and 7, the design space is relatively wider where $\dot{m}^*$ can be between 0.8 and 1.2 to safely meet performance requirements. The design space narrows down with shell *AR* smaller than 4, due to a restriction on charge utilization, and with shell *AR* larger than 7, due to a restriction on exergetic efficiency. Therefore, the recommended range of shell *AR* is between 4 and 7 to accommodate a wide range of operating conditions.

System Design Procedure

The system design procedure takes input including actual mass flow rate, operating temperature range, desired tube size, and a design space obtained from the previous section to determine the storage capacity in the first iteration loop. Based on the determined storage capacity, the shell geometry is then provided following the second iteration loop, outputting shell inner diameter, corresponding baffle spacing, number of tubes and shell length. The flow chart in Figure 72 presents the above-described design procedure in detail.

Figure 72: System Design Procedure Flow Chart

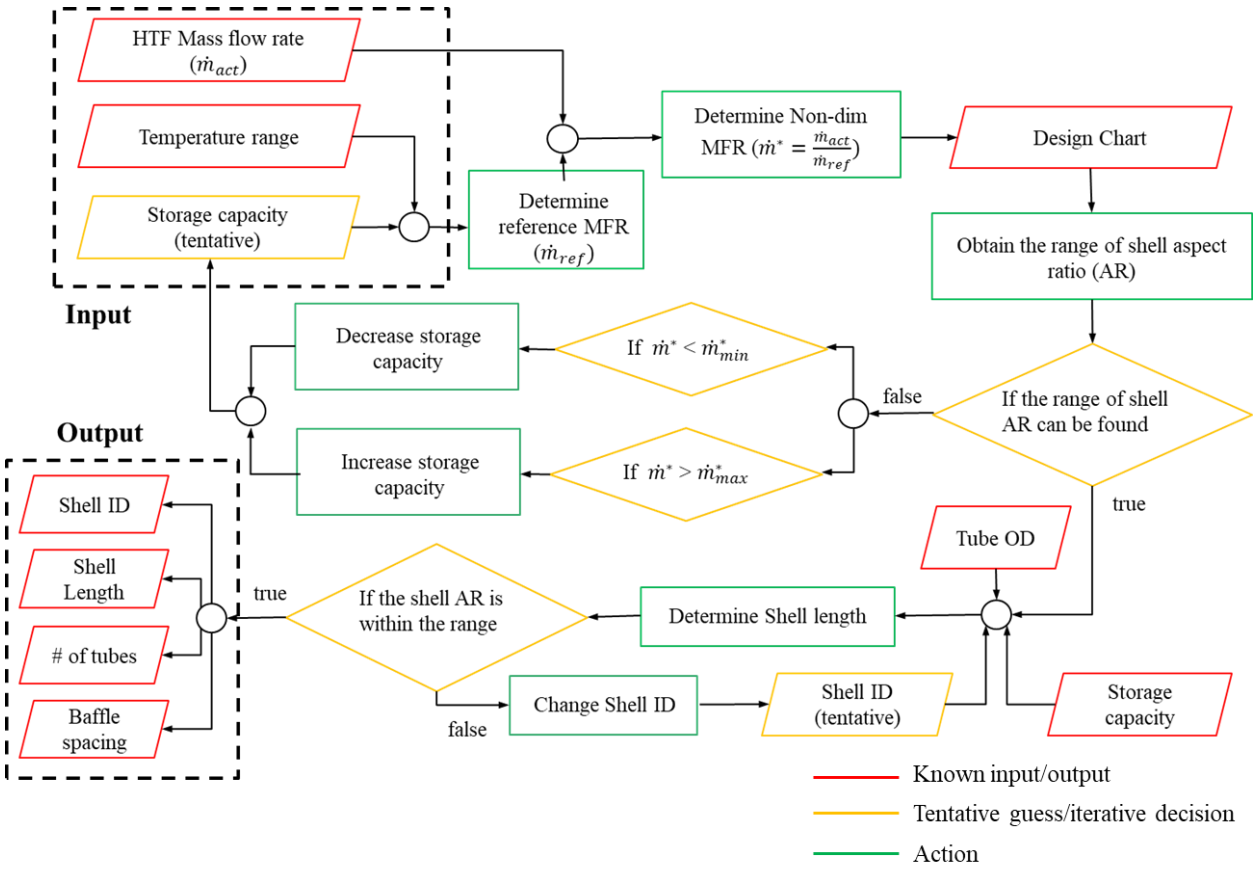

Source: UCLA, Wirz Research Group

Red colored input/output parameters denote those that are known from users or the decided outcome from the process, whereas yellow colored ones refer to tentative guesses, requiring iterations. Actions are green colored. Firstly, determine the storage capacity with an initial guess. Based on the tentative storage capacity, the nondimensional mass flow rate can be obtained. If the above obtained $\dot{m}^*$ falls within the design space, the range of shell *AR* can be determined. If not, increase the storage capacity if $\dot{m}^*$ is higher than the upper limit or vice versa. The iteration shall proceed until a reasonable storage capacity is determined to have $\dot{m}^*$ fallen within the design space that specifies the range of shell *AR*. The second iteration loop starts with a known range of shell *AR* to determine the complete shell geometry. For a fixed storage capacity and decided tube size, provide a guess of shell inner diameter, $D_{sh,i}$, and compute the shell length and corresponding shell *AR*. If the shell *AR* falls in between the *AR* range obtained from last step, the design process is concluded, outputting all necessary design parameters. If not, change the value of $D_{sh,i}$, and the second loop shall be iterated till the shell *AR* falls into the appropriate range.

System Cost Analysis

In this section, capital costs of single-tank (thermal battery configuration) and two-tank SulfurTES systems are estimated and compared with molten-salt TES systems. Based on the capital cost, levelized cost of energy (LCOE) is estimated using System Advisor Model (SAM) [71], assuming SulfurTES integration with CSP-trough plant and CSP-power tower.

Cost Comparison of SulfurTES with Molten-Salt TES system

The cost of SulfurTES is estimated based on operating conditions listed in Table 9.

Table 9: Operating Condition of CSP-Trough Plant and CSP-Power Tower

	T_C°C	T_D°C	T_{PC}°C	ϕ_C
Trough	500	200	450	0.395
Tower	650	200	500	0.41

Source: UCLA, Wirz Research Group

T_{PC} stands for the power block inlet temperature and ϕ_C is the corresponding cycle conversion efficiency [0]. The charging needs to occur at 650°C for a power tower so that sulfur stays below the operating temperature limit of SS316 tank, while 500°C for a trough plant is needed considering the practical upper temperature limit of parabolic trough collector. Cold sulfur is kept above 200°C to avoid freezing in two-tank configuration.

The cost estimation spans from commercial scale (around 10 MWh) to utility scale (around 2GWh) to provide a comprehensive cost map for SulfurTES in both single-tank and two-tank configurations. The cost map reveals unique cost advantage of each configuration in different scales of storage capacity.

The capital TES cost of single-tank SulfurTES is estimated as:

$$C_{sys} = \frac{m_t C_t + L_f C_f + m_s C_s + m_{sh} C_{sh} + Q_{TES} C_{found} + A_{ins} C_{ins}}{Q_{stored} \times U_d} \quad (28)$$

where L_f is the total length of tube fabrication required. It is assumed that the shell is made of cast iron, sitting on a foundation made by a pile of sand with a concrete reinforced ring wall and wrapped around by calcium silica insulation. Detailed component prices are listed in Table 10.

Table 10: Component Price of Single-Tank SulfurTES System

Material cost ($/kg)				Fabrication cost ($/ft) [70]	Insulation cost [72] ($/m$_2$)	Foundation cost [72] ($/kWh)
Sulfur	SS316 [67]	Cast iron [68]	AL2291 [69]			
0.04	4.34	1.39	2	1.99	235	1.1

Source: UCLA, Wirz Research Group

The tube is initially made by SS316 to withstand high temperature (greater than 600°C) and sulfur internal pressure associated with it. However, colder tube section exists near charge outlet. Cheaper and lighter materials, such as aluminum alloy 2291 (AL2291), can be used at cold section (up to 430°C) to reduce the SS316 usage that further reduces the system cost.

Single-tank SulfurTES systems have tubes with d_o = 0.168 m and a shell AR = 4. Performance of such systems integrated with CSP-trough plant and CSP-power tower are listed in Table 11.

Table 11: Single-Tank SulfurTES Performance

	U_C%	U_{ST}%	U_D%	Cold section
Trough	79	83	68	0.57
Tower	83	85	80	0.15

Source: UCLA, Wirz Research Group

where U_C, U_{ST}, U_D denote to charge, storage capacity and discharge utilization. Cold section stands for the portion of system that is below 430°C where aluminum tubes are used. Due to inherent inefficiency in both charging and discharging, the storage capacity of single-tank SulfurTES is overdesigned, and determined as $Q_{capacity} = \frac{Q_{12h}}{U_D \times U_{ST}}$ where Q_{12h} is the thermal energy required for a 12-hour power block operation.

The two-tank molten-sulfur TES is analogous to molten-salt TES system, with a hot tank and a cold tank. The capital cost of two-tank SulfurTES is estimated as:

$$C_{sys} = \frac{Q_{TES}(C_s + C_{found} + C_{pump} + C_{piping}) + m_{tank}C_{tank} + A_{ins}C_{ins}}{Q_{TES}} \quad (29)$$

where costs of tube and shell are replaced by costs of tank, pumping and piping.

Figure 73: Schematic of Two-Tank SulfurTES System

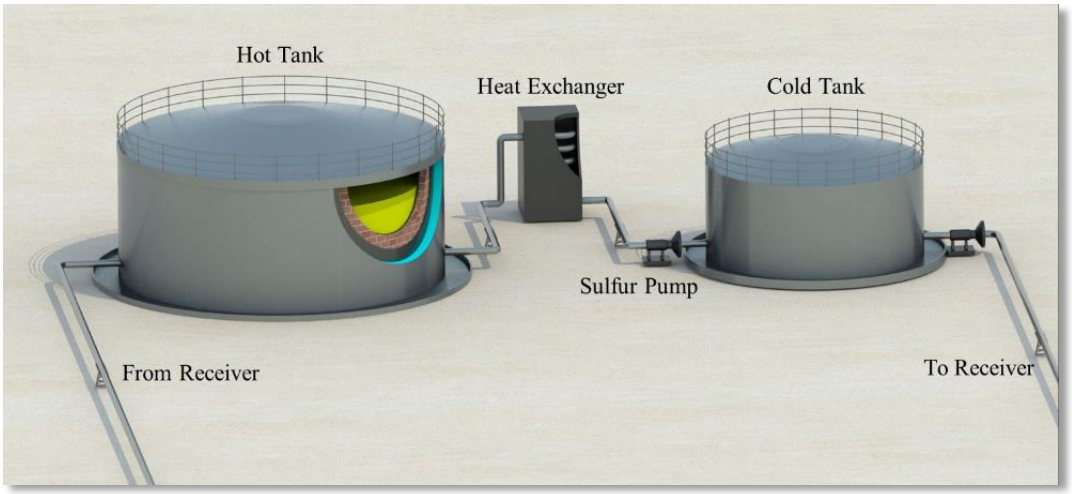

Source: UCLA, Wirz Research Group

The storage tank is made of SS316 with a thickness of 0.1—0.25 m and 0.03—0.1 m for hot and cold tanks respectively to withstand sulfur vapor and hydraulic pressure. Cost of piping, foundation, and insulation share the same value of molten-salt TES system. A more powerful pump is used, where the pumping cost is assumed to be twice as expensive to overcome high sulfur viscosity near 200°C. Prices for the components discussed are listed in Table 12.

Table 12: Component Price of Two-Tank SulfurTES and Molten-Salt TES System

	Sulfur cost ($/kWh)	Molten-salt Cost ($/kWh)	Tank material price ($/kg)	Foundation ($/kWh)	Sulfur pump cost ($/kWh)	Salt pump cost($/kWh)	Piping valve ($/kWh)	Insulation cost ($/m^2)
Trough	**1.09**	**10**	4.34	1.1	**0.94**	**0.47**	0.2	235.00
Tower	**0.73**							

Source: UCLA, Wirz Research Group

Comparison of capital TES cost between single-tank/two-tank SulfurTES and molten-salt TES is demonstrated in Figure 74.

Figure 74: TES Capital Cost Comparison Between SulfurTES and Molten-Salt TES

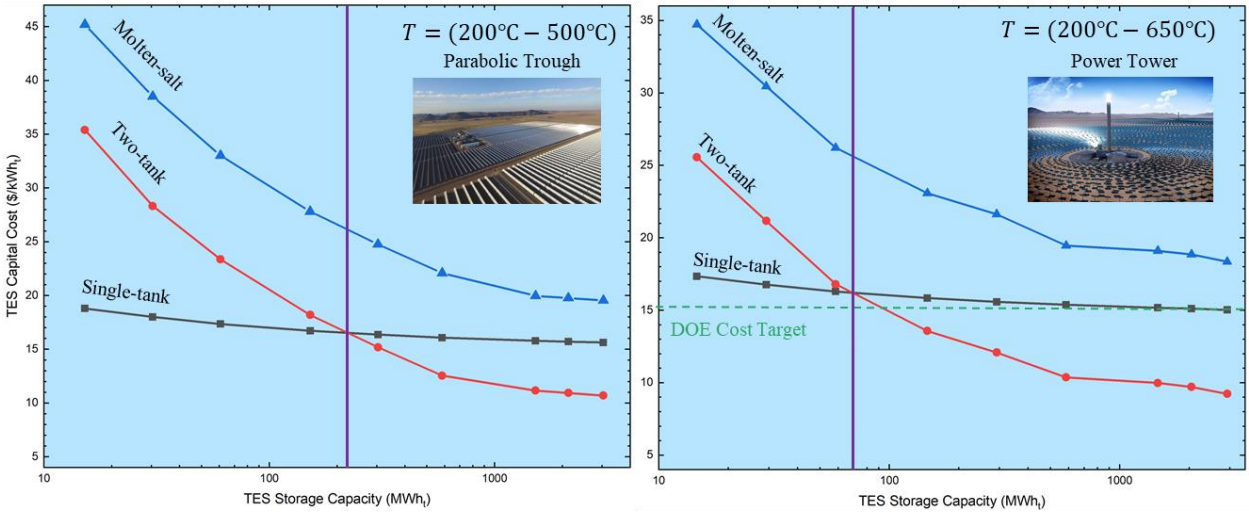

Integrating with (a) CSP-Trough Plant and (b) CSP-Power Tower.

Source: UCLA, Wirz Research Group

A considerable cost advantage of SulfurTES is seen from the comparison with molten-salt TES system, due to much lower cost of storage medium ($0.73-1.09/kWh as opposed to $10/kWh [0]). The capital cost of single-tank SulfurTES is the lowest in commercial scale, while the cost of two-tank SulfurTES decreases rapidly as storage capacity increases to utility scale, intersecting with that of single-tank SulfurTES at around 100 MWh capacity. The United States Department of Energy (USDOE) Sunshot TES cost target of $15/kWh is achieved by both single-tank and two-tank SulfurTES systems.

LCOE Comparison Between SulfurTES and Molten-Salt TES Systems

The LCOE of both SulfurTES and molten-salt TES systems is obtained using System Advisor Model (SAM) [71], integrating with CSP-trough plant and CSP-power tower plant. A solar multiple (SM) of 3.5 is used for both plants to accommodate a 12-hour TES system. The LCOE is calculated as:

$$\text{LCOE} = \frac{\text{sum of plant cost and TES cost over life time}}{\text{Total energy produced over lifetime}} \tag{30}$$

where the plant cost and total energy produced over a 30-year lifetime is obtained from SAM and the calculation of TES cost is shown in Chapter 4. The LCOE is presented with plant capacity ranging from 20 MWe to 1 GWe in Figure 74.

Figure 75: Levelized Cost of Energy of SulfurTES and Molten-Salt TES

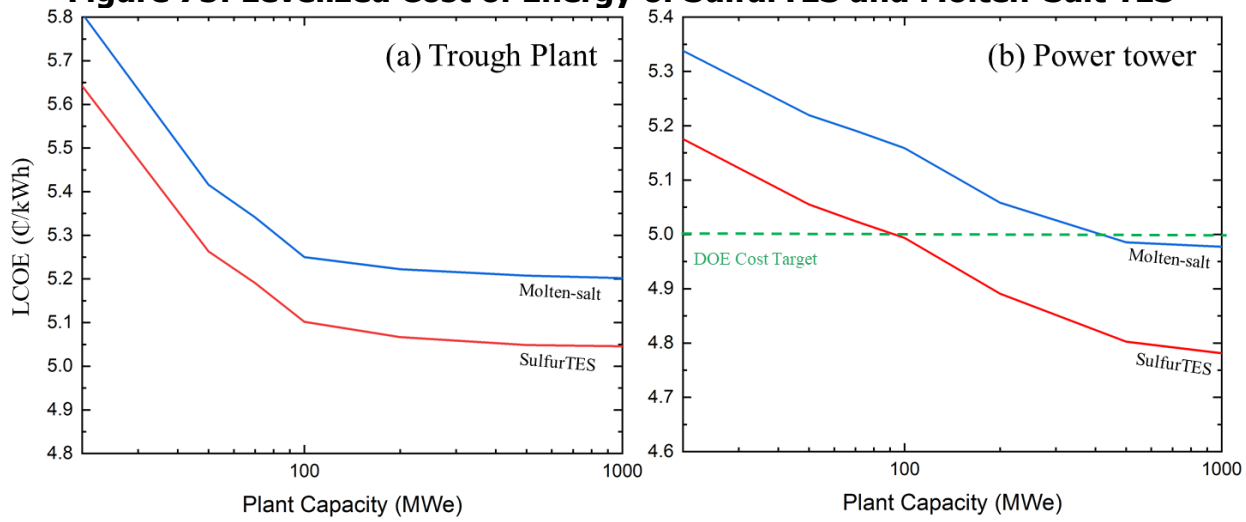

With (a) CSP- Trough Plant (b) CSP-Power Tower.

Source: UCLA, Wirz Research Group

Figure 75 demonstrates that replacing molten salt with molten sulfur reduces the LCOE by ~¢0.15/kWh and ¢0.2/kWh in a CSP-trough plant and a CSP-power tower respectively. The USDOE cost target for power tower of $0.05/kWh is achieved by SulfurTES system with plant capacity above 90 MWe. With a 30-year lifetime, the total amount of saving by SulfurTES system is around $275 million for a one GWe power plant, shown in Figure 76.

Figure 76: Total Amount of Saving With SulfurTES System

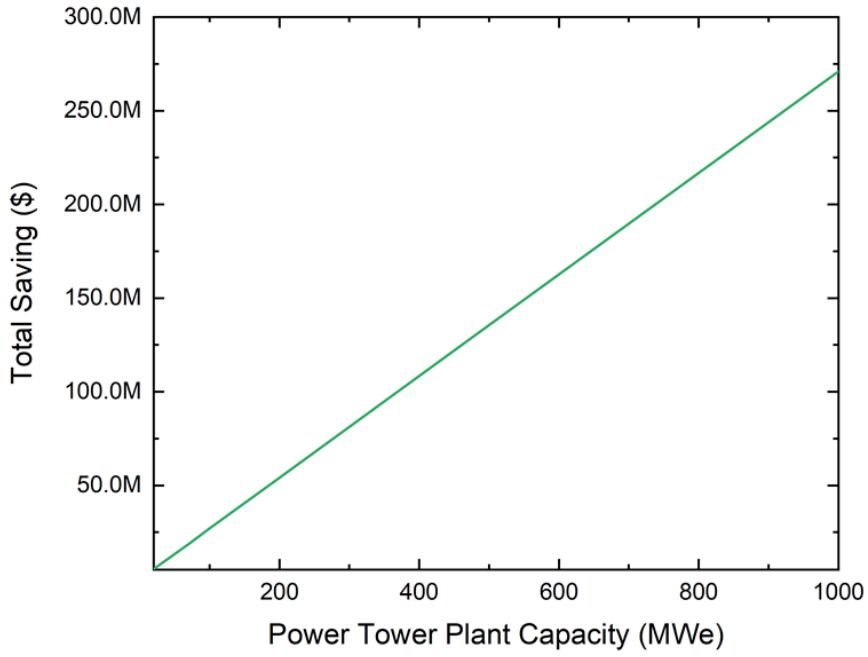

Source: UCLA, Wirz Research Group

In 2017, the annual electricity consumption in California was 206,328 GWh, which is around 32 percent of total energy consumption. [0]. Sustainable LA grand challenge requires 100 percent of electricity generation from renewable energy source by 2050[0]. If 25—50 percent of electricity generation was assumed to come from a CSP plant, a total of $5.6 billion to $11.3

billion annual savings will be seen in California, and an $84.6 billion to $169 billion total savings to the United States can be achieved with SulfurTES systems.

Conclusion

A transient two-dimensional system-cost model is developed to characterize the techno-economic performance of the SulfurTES system. This model is validated using the demonstration results of the laboratory-scale SulfurTES thermal battery, with around 5 percent error. This high-fidelity model is used to conduct a parametric study on key parameters, including tube size, shell aspect ratio, and mass flow rate of HTF. By characterizing the system level performance with charge/discharge utilization, charge/discharge exergetic efficiency, round-trip efficiency and storage capacity utilization, the following conclusion can be made:

1. Increase in mass flow rate is beneficial to capacity utilization where increased amount of energy is supplied to have the storage capacity fully utilized.
2. Increase in mass flow rate lowers the potential of energy transfer that leads to monotonically decreasing charge utilization and charge exergetic efficiency.
3. Increased mass flow rate yields higher rate of energy recovery during discharging, leading to an increase in discharge utilization.
4. The combined effect of charge and discharge utilization leads to a small variation in round-trip efficiency with $\dot{m}^* < \sim 1$. Further increase in mass flow rate yields lower charge utilization that in turn lowers the round-trip efficiency.
5. High mass flow rate is in favor of discharge exergetic efficiency as large amount of exergy can be recovered.
6. Large shell *AR* and small tube size are beneficial to HTF heat transfer performance that leads to improved system level performance. However, care should be taken with large mass flow rate as exergy destruction can be substantial, lowering the exergetic efficiency.

Following the parametric study, a system design tool is provided with a method in finding the design space based on user specified performance requirements, and an iterative design procedure that determines storage capacity and shell geometry. It is suggested that the shell *AR* should be between 4 and 7 to have relatively wider range of selection in operating mass flow rate.

The capital cost estimation demonstrates SulfurTES's significant cost advantage over molten-salt TES systems, achieving USDOE Sunshot cost target of $15/kWh. It also confirms that the single-tank SulfurTES is more economically favorable in commercial scale (less than around 100 MWh), while two-tank SulfurTES has prominently lower costs in utility scale (larger than around 100 MWh). Comparing the LCOE of SulfurTES with that of molten-salt TES systems in a 30-year lifetime, is around $0.15/kWh and $0.2/kWh reduction are seen with CSP-trough plant and CSP-power tower, respectively. The reduction in LCOE leads to around a $275 million saving with 1 GWe plant capacity and can bring $5.6 billion to $11.3 billion savings to California and $84.6 billion to $169 billion total savings to the United States in the near future.

CHAPTER 8:
Benefits to Ratepayers

The project is an enabling technology that increases the reliability and dispatchability of CSP plants by providing power generation ability at non-solar hours. Also, the project reduces the cost of TES and consequently LCOE. The project eliminates molten salt which is an expensive thermal storage fluid due to its use as a fertilizer commodity. The project reduces the cost of TES to $15/kWh leading to a decrease in the share of TES in LCOE from $0.32/kWh to $0.12/kWh. This change in LCOE is estimated to provide $1.6 billion to $3.3 billion in savings for California, depending on the grid penetration of CSP technology.

Figure 77: Grid-Scale Energy Storage Market Growth

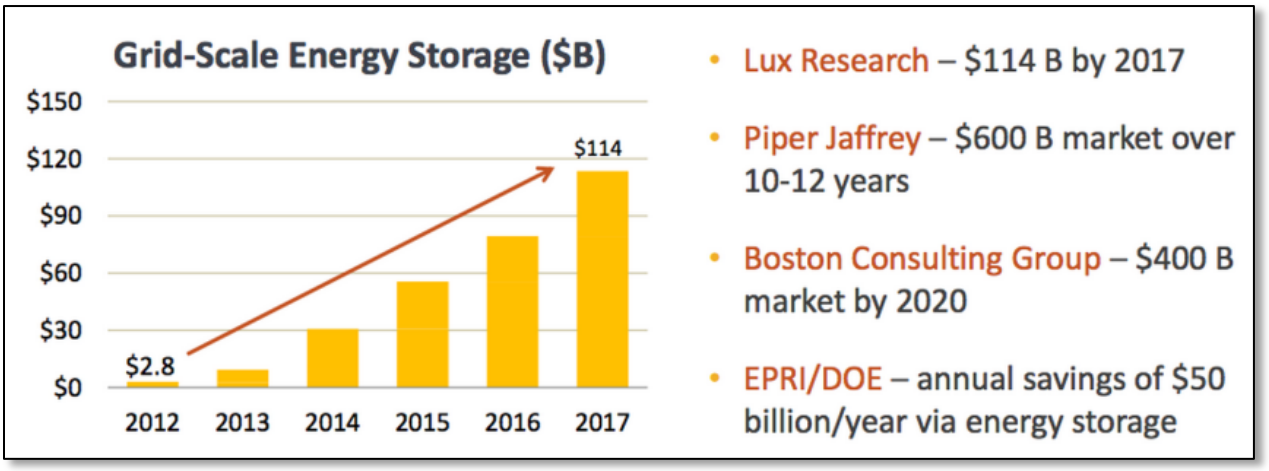

Source: EPRI/USDOE

The project stores excess harvested solar energy during off-peak hours and provides the energy required for power generation during peak demand or non-solar hours (discharge in 12 to 16 hours). The state of California's GHG emission associated with electricity generation in the year of 2017 was 776 ton/MWe of CO2, 0.023 ton/MWe of SO2, and 1.2 ton/MWe of NOx [0]. The study's calculations show that 344 GWh of thermal energy storage systems lead to significant reduction of annual emission of GHG: 22 million tons of CO2, 661 tons of SO2, and 34-thousand tons of NOx. Also, by shifting the workload of the power plant from day to night, the temperature of the heat sink of the power generation cycle reduces and provides California with 2.95 Ton/MW of water saving.

The total global utility-scale electricity storage market is valued at nearly $4 billion in 2010 and is expected to reach $18.5 billion by 2015. [60] The size of the market estimate varies significantly depending on the research organization being cited, however all estimates cite tremendous growth as grids adopt renewable energy. The graph below summarizes the available data on market growth. [61]

In California alone, the 2020 energy storage mandate may require investments of as much as $3 billion on power-storage systems in California to facilitate wider use of renewable energy. For the CSP thermal energy storage market, the 2013 global total addressable market (TAM)

can be estimated at $2.6 billion and the U.S. TAM is estimated at $1.6 billion (Figure 78). The majority of the U.S. market is located in the Southwestern U.S., including California. For the CSP industry, the market is expected to grow at a compounded annual growth rate of 44.9 percent. [62]

A growing problem faces the California electrical grid. More and more of the state's electricity is being generated by renewable sources such as wind and solar, yet by their nature these power sources are (1) unable to match power production to use, and (2) highly variable and/or intermittent in their production, when compared to traditional electricity sources. Taken together, these issues are a serious impediment to the proliferation of renewable energy in California. This proposed project addresses these problems by providing the California electricity grid with cost-effective energy storage. When combined with CSP, the technology allows for dispatchable power generation that will complement other nondispatchable renewable energy sources and allow California to build the next generation renewable energy grid.

Figure 78: Grid-Scale Energy Storage Market Growth

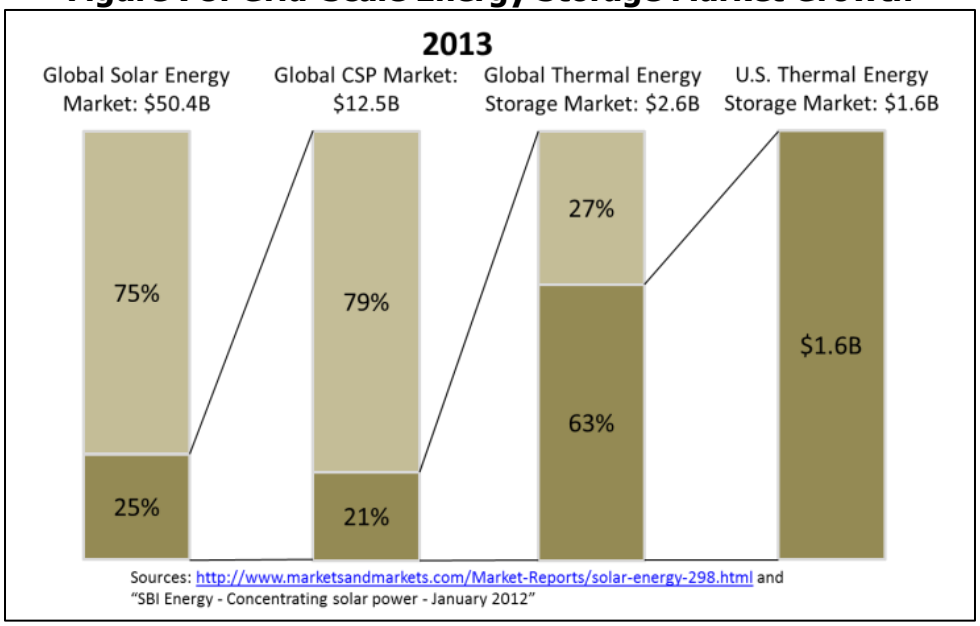

Source: SBI Energy

A 10-year net present value (NPV) model for the benefits realized by California due to the proposed technology is performed. Assuming technology deployment beginning in 2017, this model estimates the 10-year NPV of benefits to be between $6.88 billion and $13.77 billion. The project is a cost-saving technology as it allows for the replacement of any future molten-salt storage technology installations with a more cost-effective alternative. Therefore, the material costs of sulfur-based TES are already accounted for in the benefit calculations stated above. Taking this into consideration, the only costs for the cost-to-benefit analysis will be the cost of bringing the technology to market. This cost can be estimated at $11.6 million. According to USDOE's SunShot goals, the cost of thermal energy storage should be reduced to less than $15/kWh to enable reduction of LCOE to $0.05/kWh by 2030. The unconstrained solution for TES proposes an optimized storage fluid promising storage cost well below SunShot goal.

The project has gained significant tech-to-market experience during its ARPA-E supported effort on a similar technology, SuperTES, which led the team to pivot toward SulfurTES as an optimized and unconstrained solution. This tech-to-market experience included the formation of a business team led by a UCLA Anderson MBA student, primary market research, industry partnerships, business plan and pitch deck development, and participation in business plan competitions that resulted in two third-place awards. The project team has leveraged the experience and knowledge gained from the SuperTES project to create a cleantech startup, Element 16 Technologies, Inc., that will serve as the commercialization vehicle for the SulfurTES project. Element 16 has received multiple grants from CEC for commercial development of the SulfurTES technology and pursue near-term beachhead market opportunities. By having a dedicated commercialization team for the project that brings together the best of academia, industry, and business, this project is in a position to successfully bring its technology to the market well in advance of the 2030 goal.

LIST OF ACRONYMS

Term/Acronym	Definition
°C	Degrees Celsius
°F	Degrees Fahrenheit
µm	micrometer
ASME	American Society of Mechanical Engineers
CHP	Combined Heat and Power
CI	Charge Inlet
CO	Charge Outlet
CO2	Carbon dioxide
CSP	Concentrated Solar Power
DAQ	Data Acquisition System
DCI	Discharge Inlet
DCO	Discharge Outlet
EDS	Energy dispersive X-ray spectrometer
GHG	Greenhouse gases
HTF	Heat Transfer Fluid
kg	kilograms
Kj/kg	Kilojoules per kilogram
kWh	Kilowatt-hour
LCOE	Levelized Cost Of Electricity
LF	Loading fractions
MoS_2	Molybdenum disulfide
MWh	Megawatt-hour
NIST	National Institute of Standards and Technology
NOx	Nitrogen oxides
NPV	Net present value
PCM	Phase Change Material
psig	Pounds per square inch, gauge
PV	Photovoltaics
SCFM	Standard Cubic Feet per Minute
SEM	Scanning electron microscope
SFD	Sulfur Filling Device
SO^2	Sulfur dioxide

Term/Acronym	Definition
SulfurTES	Sulfur Thermal Energy Storage
TAM	Total addressable market
TEMA	Tubular Exchanger Manufacturers' Association
TES	Thermal Energy Storage
ton/MW_e	tons per megawatt-hour electric
TSS	Thermal Storage Systems (CSP company)
UCLA	University of California, Los Angeles
UDF	User-defined function.
USDOE	United States Department of Energy
V	Volt
W	Watt

REFERENCES

1. Wells, P., Nithyanandam, K. and Wirz, R. Cost Optimal Strategies of High Temperature Thermal Energy Storage Systems in Combined Heat and Power Applications. ASME 2016 10th International Conference on Energy Sustainability collocated with the ASME 2016 Power Conference and the ASME 2016 14th International Conference on Fuel Cell Science, Engineering and Technology, 2016; 1: V001T03A006-V001T03A006.

2. Haeseldonckx, D., Peeters, L., Helsen, L., D'haeseleer, W. The impact of thermal storage on the operational behaviour of residential CHP facilities and the overall CO2 emissions, Renewable and Sustainable Energy Reviews, 2007; 11: 1227-1243.

3. Stekli, J., Irwin, L. and Pitchumani, R. Technical challenges and opportunities for concentrating solar power with thermal energy storage. Journal of Thermal Science and Engineering Applications, 2013; 5: 021011.

4. Xu, B., Li, P. and Chan, C. Application of phase change materials for thermal energy storage in concentrated solar thermal power plants: a review to recent developments. Applied Energy, 2015; 160: 286-307.

5. Singh, D., Kim, T., Zhao, W., Yu, W. and France, D.M. Development of graphite foam infiltrated with MgCl 2 for a latent heat based thermal energy storage (LHTES) system. Renewable Energy, 2016; 94: 660-667.

6. Kim, T., France, D.M., Yu, W., Zhao, W. and Singh, D. Heat transfer analysis of a latent heat thermal energy storage system using graphite foam for concentrated solar power. Solar Energy, 2014; 103: 438-447.

7. Allen, M.J., Bergman, T.L., Faghri, A. and Sharifi, N. Robust heat transfer enhancement during melting and solidification of a phase change material using a combined heat pipe-metal foam or foil configuration. Journal of Heat Transfer, 2015; 137: 102301.

8. Nithyanandam, K. and Pitchumani, R. Computational studies on metal foam and heat pipe enhanced latent thermal energy storage. Journal of Heat Transfer, 2014; 136: 051503.

9. Alam, T., Dhau, J., Goswami, Y., Stefanakos, E. Macroencapsulation and characterization of phase change materials for latent heat thermal energy storage systems. Applied Energy, 2015; 154: 92-101.

10. Pardo, P., Deydier, A., Anxionnaz-Minvielle, Z., Rouge, S., Cabassud, M., Cognet, P. A review on high temperature thermochemical heat energy storage. Renewable and Sustainable Energy Reviews, 2014; 32: 591-610.

11. Prieto, C., Cooper, P., Inés Fernández, A., Cabeza, L., F. Review of technology: Thermochemical energy storage for concentrated solar power plants. Renewable and Sustainable Energy Reviews, 2016; 60: 909-929.

12. Ulf, H., Bruce K., Henry P. Two-tank molten salt storage for parabolic trough solar power plants. Energy, 2004; 29: 883-893.

13. Kearney, D., Herrmann U., and Nava, P., et al. Assessment of a Molten Salt Heat Transfer Fluid in a Parabolic Trough Solar Field. ASME. J. Sol. Energy Eng., 2003; 125: 170-176.

14. Evaluation of Annual Performance of 2-Tank and Thermocline Thermal Storage Systems for Trough Plants. ASME. J. Sol. Energy Eng., 2011; 133: 031023-031023-5.

15. Gil, A., Martorell, I., Potau, X., Cabeza, L. State of the art on high temperature thermal energy storage for power generation. Part 2- Case studies. Renewable and Sustainable Energy Reviews, 2010; 14: 56-72.

16. I., Arias, S., Ramirez, D. Gemasolar, the first tower thermosolar commercial plant with molten salt storage. 2012.

17. E., Bradshaw, R., W., Dawson, D., B., Rosa, W., D., Gilbert, R., Goods, S., H., Hale, M., J., Jacobs, P., Jones, S., A., Kolb, G., J., Prairie, M., R., Reilly, H., E., Showalter, S., K., Vant-Hull, L., L. Final test and evaluation of results from solar two project. Sandia National Laboratories, 20002; SAND2002-0120.

18. I., Hearps, P., J., Wright, M., N. Molten salt power towers: Newly commercial concentrating solar storage. Proceedings of IEEE,2012; 100: 504-515.

19. Medrano, M., Gil, A., Martorell, I., Potau, X., Cabeza, L., F. State of the art on high-temperature thermal energy storage for power generation. Part 2- case studies. Renewable and sustainable energy reviews, 2010; 14: 56-72.

20. Mehos, M., Turchi, C., Jorgenson, J., Denholm, P., Ho, C. and Armijo, K. On the Path to SunShot: Advancing Concentrating Solar Power Technology, Performance, and Dispatchability (No. NREL/TP-5500-65688; SAND2016-2237 R). NREL (National Renewable Energy Laboratory (NREL), Golden, CO (United States)), 2016.

21. Wirz, R., E., Stopin, A.,P.,P., Louis, A.,T., Lavine, A.,G., Kavehpour, H.,P., Lakeh, R.,B., Furst, B.,I., Bran, G. and Garcia-Garibay, M.,A., The Regents Of The University Of California. High-density, high-temperature thermal energy storage and retrieval, 2014; U.S. Patent Application 14/475,479.

22. Clark, P.D. and N.I. Dowling, Capture of solar energy using elemental sulfur. Journal of Sulfur Chemistry, 2004. 25(1): p. 7-11.

23. Brown, A. and J. Battles, The corrosion of metals and alloys by sodium polysulfide melts at 350/sup 0/C. 1986, Argonne National Lab., IL (USA).

24. Brown, A.P., The corrosion behavior of molybdenum and Hastelloy B in sulfur and sodium polysulfides at 623 K. Journal of The Electrochemical Society, 1987. 134(8): p. 1921-1925.

25. Journal of The Electrochemical Society, 1987. 134(10): p. 2506-2507.

26. Wefers, and L. D. Hart, Editor. 1990, The American Ceramic Society, Westerville, Ohio: Ohio.

27. and W. Giggenbach, Hydrogen sulphide ionization and sulphur hydrolysis in high temperature solution. Geochimica et Cosmochimica Acta, 1971. 35(3): p. 247-260.

28. Corrosion in the petrochemical industry. 1994: ASM international.

29. Influence of sulphur on high temperature degradation of steel structures in the refinery industry. Advances in Materials Science, 2006. 6(1): p. 16-25.

30. Mahoud, S., LOCALIZED CORROSION OF CORROSION RESISTANT ALLOYS IN SULFUR-CHLORIDE-CONTAINING ENVIRONMENTS. S. E. Mahoud, H. E. Chaung and C. W. Peterson. CORROSION 90/70, NACE, Houston, TX. Per Copy$ 4, 1990.

31. Maldonado, S. and P. Boden. The Mechanism of Corrosion of Mild Steel by Elemental Sulphur/Water Suspensions. in Metallic Corrosion. 8th International Congress on Metallic Corrosion. 1981.

32. Schmitt, G., Effect of elemental sulfur on corrosion in sour gas systems. Corrosion, 1991. 47(4): p. 285-308.

33. Smith, L. and B.D. Craig, Practical Corrosion Control Measures for Elemental Sulfur Containing Environments. CORROSION 2005, 2005.

34. Stott, F., F. Chong, and C. Stirling. The Influence of Reactive Elements on Sulphidation Resistance at High Temperatures. in Materials Science Forum. 1991. Trans Tech Publ.

35. Sudworth, J. and A. Tiley, Sodium Sulphur Battery. 1985: Springer.

36. Zagal, S.M. and P. Boden, HYDROLYSIS OF ELEMENTAL SULPHUR IN WATER AND ITS EFFECT ON THE CORROSION OF MILD STEEL. S. B. Maldonado Zagal and P. J. Boden, Br. Corros. J., 17, 1982(3).

37. S Jr, G.C., Sulfur mining with steam. 1971, Google Patents.

38. Butterworth, C. and J. Schwab, Sulfur Mining as a Processing Industry. Industrial & Engineering Chemistry, 1938. 30(7): p. 746-752.

39. Oana, S. and Y. Mizutani. Sulphur isotopic fractionation between hydrogen sulphide and sulphuric acid formed by the 4S+ 4H20= 3H2S+ H2SO4 reaction. in Symp. Geochem. Soc. Japan, Nagoya. 1966.

40. Mrowec, S., The problem of sulfur in high-temperature corrosion. Oxidation of Metals, 1995. 44(1-2): p. 177-209.

41. West J.R., "Thermodynamic Properties of Sulfur," Industrial and Engineering Chemistry, vol. 42, No. 4, pp. 713-718, 1950.

42. Rau, H., Kutty T.,R.,N., and Carvalho J,. High temperature saturated vapour pressure of sulphur and estimation of its critical quantities. J. of Chem. Thermodynamics, 1973; 5: 291-302.

43. Meyer B. "Elemental sulfur," Chemical reviews, vol. 76, no. 2, pp. 367-388, 1976.

44. Tuller, W., Freeport Sulphur Company. The sulphur data book. McGraw-Hill book company, Inc., 1954.

45. Nithyanandam, K., Barde, A., Baghaei, L.,R., Wirz, R. Charge and discharge behavior of elemental sulfur in isochoric high temperature thermal energy storage systems. Applied Energy, 2018.

46. Nithyanandam, K., Barde, A., Wirz R E. Heat transfer behavior of elemental sulfur for low temperature thermal energy storage applications. IJHMT, 2018; 127: 936-948.

47. Bacon, R.F. and Fanelli, R., 1943. The Viscosity of Sulfur. *Journal of the American Chemical Society*, *65*(4), pp.639-648

48. Fanelli, R., 1946. Modifying the viscosity of sulfur. *Industrial & Engineering Chemistry*, *38*(1), pp.39-43.

49. Rubero, P.A., 1964. Effect of Hydrogen Sulfide on the Viscosity of Sulfur. *Journal of Chemical & Engineering Data*, *9*(4), pp.481-484.

50. Timrot, D.L., Serednitskaya, M.A., Medveditskov, A.N. and Traktueva, S.A., 1981. Thermophysical properties of a sulfur-iodine binary system as a promising heat transfer medium for heat pipes. *Journal of Heat Recovery Systems*, *1*(4), pp.309-314.

51. El-Sharkawy, A.A. and Dessouky, M.T., 1983. Measurement of thermal conductivity, heat capacity, and thermal diffusivity of sulfur and selenium in the liquid state. *International journal of thermophysics*, *4*(2), pp.115-125.

52. Voller, V.R., Cross, M. and Markatos, N.C., 1987. An enthalpy method for convection/diffusion phase change. *International journal for numerical methods in engineering*, *24*(1), pp.271-284.

53. Nithyanandam, K., Barde, A., Tse, L., Lakeh, R.B. and Wirz, R., 2016, June. Heat Transfer Behavior of Sulfur for Thermal Storage Applications. In *ASME 2016 10th International Conference on Energy Sustainability collocated with the ASME 2016 Power Conference and the ASME 2016 14th International Conference on Fuel Cell Science, Engineering and Technology* (pp. V001T05A008-V001T05A008). American Society of Mechanical Engineers.

54. Saric, W.S., 1994. Görtler vortices. Annual Review of Fluid Mechanics, 26(1), pp.379-409.

55. Nithyanandam, K., Stekli, and Pitchumani, R., 2017. High-temperature latent heat storage for concentrating solar thermal technologies. In: Blanco, M. and Santigosa, L.R. eds.

Advances in Concentrating Solar Thermal Research and Technology. Woodhead Publishing, pp. 213-246.

56. Wirz R.E., Barde, A., Nithyanandam, K., "Thermal Energy Storage System", International Patent Application No. PCT/US2017/019947

57. Lakeh, R.B., Lavine, A.S., Kavehpour, H.P. and Wirz, R.E., 2015. Study of turbulent natural convection in vertical storage tubes for supercritical thermal energy storage. *Numerical Heat Transfer, Part A: Applications*, *67*(2), pp.119-139.

58. Standards of Tubular Exchanger Manufacturers Association, 9th edition http://www.tema.org/

59. Я. Петков, "HEAT EXCHANGER DESIGN HANDBOOK – Heat exchanger theory – Ernst U. Schlunder.

60. BCC Research Report EGY056B, Jan 2011, "Utility-scale Electricity Storage Technologies: Global Markets"

61. http://cleantechnica.com/2013/06/01/top-50-solar-energy-stories-of-the-year-part-one-1-10/

62. http://www.marketsandmarkets.com/Market-Reports/solar-energy-298.html

63. "ASME/ANSI B36.10/19." The American Society of Mechanical Engineers, Welded and Seamless Wrought Steel Pipe, 2015.

64. J. Taborek, Shell-and-tube heat exchangers, Heat Exchanger Design Handbook, vol. 3. New York, NY: Hemisphere Publishing Corporation, 1988.

65. "NIST Chemistry WebBook, Standard Reference Database Number 69." [Online]. Available: https://webbook.nist.gov/chemistry/.

66. W. N. Tuller, "The sulphur data book.," Sulphur Data Book, 1954.

67. PENN STAINLESS, "Budget quote," 10-Apr-2017.

68. U.S. Bureau of Labor Statistics, "Producer Price Index by Commodity for Metals and Metal Products: Cast Iron Scrap," *FRED, Federal Reserve Bank of St. Louis*, 01-Dec-1986.

69. "Aluminum Prices and Aluminum Price Charts," *InvestmentMine*, 2018

70. "DFMA Product Costing and Simplification." [Online]. Available: https://www.dfma.com/

71. "System Advisor Model (SAM)", National Renewable Energy Laboratory. Available: https://sam.nrel.gov/

72. Glatzmaier, G. Developing a cost model and methodology to estimate capital costs for thermal energy storage. No. NREL/TP-5500-53066. National Renewable Energy Lab.(NREL), Golden, CO (United States), 2011.

73. M. A. Rosen, "Appropriate Thermodynamic Performance Measures for Closed Systems for Thermal Energy Storage," J. Sol. Energy Eng., vol. 114, no. 2, pp. 100–105, May 1992.

74. Gilman, Paul, et al. Solar advisor model user guide for version 2.0. No. NREL/TP-670-43704. National Renewable Energy Lab.(NREL), Golden, CO (United States), 2008.

75. Schuknecht, Nathan, Jennifer McDaniel, and Harrison Filas. "Achievement of the $100/m2 parabolic trough." AIP Conference Proceedings. Vol. 2033. No. 1. AIP Publishing, 2018.

76. Mehos, Mark, et al. On the Path to SunShot-Advancing Concentrating Solar Power Technology, Performance, and Dispatchability. No. NREL/TP-5500-65688 SAND-2016-2237 R. EERE Publication and Product Library, 2016.

77. "Electric Generation Capacity & Energy", California Energy Commission. Available: https://www.energy.ca.gov/almanac/electricity_data/electric_generation_capacity.html

78. "Sustainability | Grand Challenges", University of California, Los Angeles. Available: https://grandchallenges.ucla.edu/sustainable-la/

79. "Detailed State Data", U.S. Energy Information Administration. Available: https://www.eia.gov/electricity/data/state/

80. Turchi, Craig S., Judith Vidal, and Matthew Bauer. "Molten salt power towers operating at 600–650° C: Salt selection and cost benefits." *Solar Energy* 164 (2018): 38-46.

APPENDIX A:
Analytical Solution for Solid-State Conduction in Steel Tube

For the solid-state conduction due to an axial temperature gradient, the temperature field is a function of time and axial location. The energy equation is represented as:

$$\frac{\partial T}{\partial t} = \alpha \frac{\partial^2 T}{\partial x^2} \tag{1A}$$

Initial condition:

$$T(t = 0) = -400x + 625 \tag{2A}$$

Boundary conditions:

$$T(x = 0) = 625 \tag{3A}$$

$$\frac{\partial T}{\partial t}(x = L) = 0 \tag{4A}$$

The analytical solution for the conduction heat transfer is:

$$T = \sum_{n=0}^{\infty} C_n \sin(\lambda_n x) e^{-\alpha \lambda_n^2 t} \tag{5A}$$

wherein,

$$C_n = 800 \left[\frac{sin(\lambda_n L) - \lambda_n L cos(\lambda_n L)}{\lambda_n^2}\right] \tag{6A}$$